

ABSTRACT

Title of Document:

Experimental and numerical characterization of
turbulent slot film cooling.

Carlos A. Cruz, PhD, 2008

Directed By:

Associate Professor André W. Marshall, and
Associate Professor Arnaud Trouv ,
Department of Fire Protection Engineering,
adjuncts to Aerospace Engineering Department.

This study presents an experimental and numerical characterization of the turbulent mixing in two-dimensional slot film cooling flows. Three different flows are considered by varying the coolant to mainstream velocity ratio (VR): a wall jet case ($VR \approx 2.0$), a boundary layer case ($VR \approx 1.0$) and a wall-wake case ($VR \approx 0.5$). For each flow, detailed measurements of the film cooling effectiveness, the heat flux, and the heat transfer coefficient are obtained for adiabatic and backside cooled wall conditions. Additionally, detailed flow velocity and temperature are measured under hot conditions using Particle Image Velocimetry (PIV) and a micro-thermocouple probe, respectively. These comprehensive measurements provide a unique data set for characterizing the momentum and thermal mixing of the turbulent flows, and for validating turbulence models in Reynolds averaged Navier-Stokes (RANS) simulations and large-eddy simulations (LES).

The three flow families display different performances. The mixing of the film is strongly influenced by the mean shear between the coolant and the hot mainstream, thus explaining that the boundary layer case provides the best effectiveness. Initially governed by the film kinematics at the injection point, the convective heat transfer is influence by the mainstream when the film mixes. Additionally, measurements indicate that semi-empirical correlations largely overpredict the mixing of the film. The results obtained with the Spalart-Allmaras RANS model compare favorably with the measurements, thereby proving that this model is a viable alternative to using correlations for the film cooling effectiveness. A Large-Eddy Simulation (LES) with the dynamic models is performed for the wall jet case under adiabatic wall conditions with inflow conditions prescribed from precursor simulations. The LES results show good agreement with measured adiabatic wall temperatures and provide unique insight into the turbulent transport mechanism and interaction between the near wall and outer shear regions responsible for the mixing of the film.

EXPERIMENTAL AND NUMERICAL CHARACTERIZATION OF TURBULENT
SLOT FILM COOLING.

By

Carlos A. Cruz

Dissertation submitted to the Faculty of the Graduate School of the
University of Maryland, College Park, in partial fulfillment
of the requirements for the degree of

PhD
2008

Advisory Committee:

Associate Professor André W. Marshall, Chair
Professor Ugo Piomelli, Dean's Representative
Associate Professor Arnaud Trouvé
Associate Professor Christopher Cadou
Associate Professor Kenneth Yu

© Copyright by
Carlos A. Cruz
2008

Acknowledgements

I would like to thank the Space Vehicle Technology Institute (SVTI) at the University of Maryland for providing the funding for this study as part of the NASA Constellation University Institute Program (CUIP). My gratitude also goes to my advisor Dr. Marshall, whose knowledge, motivation, support and patience greatly contributed to the success of this study. I also thank my co-advisor Dr. Arnaud Trouv  for his guidance and rigorous methodology in the validation and interpretation of the numerical simulation results. I would like to extend my gratitude to the other member of the film cooling research group: Dr. Christopher Cadou, Kiran Dellimore, and Fernando Raffan. I also express my gratitude to Dr. Ugo Piomelli for sharing his expertise of large-eddy simulations and guiding me through this project. This project would not have been possible without the help and support of several of my fellow graduate students. I would like to personally thank Luis Bravo for his contributions to the code implementations, and my colleague and friend Fernando Raffan for his contributions, his valuable expertise in Particle Image Velocimetry, and his support.

I also would like to express my gratitude to the other members of my advisory committee, Dr. Kenneth Yu and Dr. Christopher Cadou. Their advice and guidance during my PhD have greatly improved my knowledge and skills.

Finally I would like to thank my family for supporting me from far away, and my girlfriend Judith Reyes-Hernandez for her continuous support, patience and love.

Table of Contents

Acknowledgements	ii
Table of Contents	iii
List of Tables.....	vi
List of Figures	vii
Nomenclature	x
Chapter 1: Introduction.....	1
1.1 Motivation: Critical Aspects of Film Cooling	1
1.2 Position of Problem	3
1.3 Literature Review	4
1.3.1 From Early Experiments to Engineering Correlations	5
1.3.2 Numerical Simulations	12
1.3.3 Summary of Previous Work	16
1.4 Objectives.....	17
1.5 Main Achievements.....	18
Chapter 2: Experimental and Numerical Methodology	20
2.1 Experimental Measurements and Analysis	21
2.1.1 Description of the Hot Wind Tunnel Facility	21
2.1.2 Measurement Techniques (PIV, μ TC, IR thermography)	26
2.1.3 Test Matrix	41
2.1.4 Typical Experimental Uncertainties.....	42
2.2 Navier-Stokes Solver.....	45
2.2.1 Fundamental Framework: RANS and LES	45
2.2.2 Governing Equations.....	46
2.2.3 Sub-Grid Scale and RANS Closure Terms.....	48
2.2.4 Discretization and Numerical Methods	53
2.2.5 Grid Requirements for Wall Resolved LES	55
2.2.6 Inflow conditions.....	57
2.3 Validation of the Solver	59
2.3.1 Fully Developed Turbulent Channel Flow Background.....	59
2.3.2 Computation Details and Post-Processing.....	61
2.3.3 Validation Results	62
2.3.4 Summary of the validation test.....	66
Chapter 3: Film Cooling Flow Analysis	67
3.1 Introduction.....	67
3.1.1 Overview of the Physics	67
3.1.2 Experimental Conditions	70
3.2 Comparison of Cases.....	71

3.2.1 Pure Mixing, the Film Cooling Effectiveness	71
3.2.2 Effect of Backside Cooling.....	75
3.3 Thermal and Momentum Mixing	81
3.3.1 Temperature mixing and scaling	81
3.3.2 Characteristics of the momentum mixing.....	87
3.4 Summary of Experimental Results.....	95
Chapter 4: Evaluation the Spalart-Allmaras RANS Model.....	97
4.1 Computational Details.....	97
4.1.1 Computational domain and boundary conditions	97
4.1.2 Methodology for the inflow conditions	100
4.1.3 Grid details	100
4.2 Quantitative Validation for the Wall Jet Case	101
4.2.1 Wall temperatures	101
4.2.2 Heat transfer prediction	103
4.2.3 Assessment of the flow predictions	105
4.2.4 Skin friction coefficient	108
4.2.5 Summary of the validation	109
4.3 Wall-Wake and Boundary Layer Cases	109
4.3.1 Film cooling effectiveness.....	109
4.3.2 Wall heat flux and shear stress.....	111
4.4 Summary: Performance of the Spalart-Allmaras Model.....	114
Chapter 5: Large-Eddy Simulation of Wall Jet Film Cooling	116
5.1 LES Computational Details	116
5.1.1 Computational domain and boundary conditions	117
5.1.2 LES inflow from precursor simulations.....	118
5.1.3 Grid details	120
5.1.4 Post-processing and statistics	121
5.2 Large-Eddy Simulation Results.....	121
5.2.1 Film cooling effectiveness and mixing.....	121
5.2.2 Mean flow statistics	124
5.2.3 Higher order statistics	127
5.3 Summary of the Main LES Results	132
Chapter 6: Conclusions.....	134
Appendix A. Experimental and Numerical Details	138
A1. Micro-Thermocouple Signal Compensation.....	138
A2. Experimental Uncertainty Analysis.....	140
A3. The Spalart-Allmaras RANS Model	146
Appendix B. Inflow Conditions for RANS and LES.....	148
B1. Mean Inlet Profiles	148
B2. Inlet Profiles of Temperature and Velocity RMS.....	149
B3. Inlet Profiles of Modified Eddy-Viscosity	151
Bibliography	152

List of Tables

Table 1. Response time of TiO ₂ tracing particles.....	29
Table 2. Particle image for particle diameters of 0.3 and 1.0 μm	32
Table 3. Experimental operating conditions.....	42
Table 4. Uncertainty on measured and derived quantities	44
Table 5. Computational grid and Reynolds numbers	61
Table 6. Experimental operating conditions.....	71
Table 7. Location of maximum velocity	126
Table 8. Variables for the profiles of mean inflow velocity and temperature	149

List of Figures

Figure 1. Slot film cooling configuration	3
Figure 2. Hot wind tunnel facility layout	22
Figure 3. Test section description	24
Figure 4. Schematic of the fluidized bed solid particle seeder.	30
Figure 5. Wall temperature and heat flux measurements	37
Figure 6. Micro-thermocouple probe assembly	38
Figure 7. Discretization on a staggered grid with wall ghost cells	54
Figure 8. Computational domain for the fully developed turbulent channel flow simulation.	59
Figure 9. Mean profiles.....	63
Figure 10. Mean profiles in wall units.....	64
Figure 11. Temperature statistics in wall units	65
Figure 12. Schematic of the film cooling flow physics.....	68
Figure 13. Experimental inlet conditions for the adiabatic cases	72
Figure 14. Adiabatic wall temperature distribution	74
Figure 15. Wall surface temperatures normalized by $(T-T_c)/(T_\infty-T_c)$	76
Figure 16. Measured heat fluxes at the film cooled wall.....	78
Figure 17. Convective heat transport	80
Figure 18. Comparison of dimensionless temperature profiles	82
Figure 19. Dimensionless temperature profile with Wieghardt similarity scaling	84
Figure 20. Wieghardt thermal thickness along the wall, adiabatic cases.	85
Figure 21. Profiles of flow temperature RMS.....	87
Figure 22. Experimental streamwise velocity profiles normalized by the freestream velocity	88
Figure 23. Streamwise velocity RMS normalized by the mainstream velocity	90
Figure 24. Wall-jet schematic with notations and similarity variables and function	91
Figure 25. Effects of wall-jet spreading	92
Figure 26. Friction coefficient for the wall-jet case VR2.0.....	95
Figure 27. Computational domain for the RANS simulations 98	
Figure 28. Schematic of the thermal boundary conditions for the backside cooled wall.	99
Figure 29. First grid point away from the wall in wall units.....	101
Figure 30. Comparison between predictions of wall temperatures.....	103
Figure 31. Heat transfer results for VR2.0NA	105

Figure 32. Velocity and temperature profiles for VR2.0AD.....	107
Figure 33. Skin friction coefficient for the wall jet case VR2.0	108
Figure 34. Adiabatic film cooling effectiveness	110
Figure 35. Heat transfer for VR0.5 and VR1.0	112
Figure 36. Downwash effect for the wall-wake case	112
Figure 37. Skin friction coefficient for all the cases.....	113
Figure 38. Computational domain for the large-eddy simulation	117
Figure 39. Film cooling effectiveness, LES, RANS and measurements	122
Figure 40. Instantaneous contour of streamwise velocity (a), and temperature (b).....	123
Figure 41. Mean profiles streamwise velocity (a) and temperature (b) compared to the present measurements	125
Figure 42. Profiles of mean velocity in wall units	126
Figure 43. Skin friction coefficient	127
Figure 44. Grid resolved normal Reynolds stresses	128
Figure 45. Resolved Reynolds shear stress in wall units.....	130
Figure 46. Temperature RMS normalized by the local temperature difference ($T_{\infty}-T_{aw}$)	131
Figure 47. Turbulent streamwise (a) and wall-normal (b) heat fluxes	132
Figure 48. Measurement of inlet temperature and velocity RMS profiles	150
Figure 49. Inlet profiles of modified eddy viscosity for RANS simulations	151

Nomenclature

Roman

C_p, C_{pb}	specific heat at constant pressure for air and thermocouple bead
C_{ev}	coefficient in eddy-viscosity subgrid-scale model
C_q	coefficient in eddy-diffusivity subgrid-scale model
d_{im}	particle image diameter in the Particle Image Velocimetry (PIV)
d_p	seeding particle diameter
$f^\#$	aperture f number of the PIV camera
$F_{w0}, F_{w,win}$	radiation view factor between wall and the casing, wall and window
h	convective heat transfer coefficient
k	turbulent kinetic energy
k_w, k_f	thermal conductivity of the wall, and fluid
L, L_0	reference length scale and Kolmogorov length scale
M_0	PIV imaging magnification ratio
m	blowing ratio $m = r_c U_c / r_\infty U_\infty$
Nu, Nu_x	mean and local Nusselt number
p	pressure
Pr	Prandtl number
Pr_t	turbulent Prandtl number
q	heat flux
q_i	subgrid-scale heat flux

q_b , q_c , q_r	conduction, convection and radiation heat flux at the wall
Re	Reynolds number
Re_s	slot Reynolds number, $Re_s = sU_c/\eta$
s	slot height
S_{ij}	strain rate tensor
St	Stanton number or Stokes number in PIV analysis (Chapter 2)
t	time or slot louver thickness
t_w	wall thickness
T	temperature
T_c , T_∞	mean coolant and mainstream temperatures
u , v , w	streamwise, wall-normal and spanwise velocity components
u_i	tensor notation of velocity: $u_1 = u$, $u_2 = v$, and $u_3 = w$
U_c , U_∞	coolant bulk velocity and mainstream velocity
x , y , z	Cartesian coordinates: streamwise, wall-normal and spanwise directions
x_i	tensor notation of the coordinate system

Greek

α	thermal diffusivity
α_t	eddy-diffusivity also referred to as turbulent diffusivity
δ	boundary layer thickness or half channel height
δ_{ij}	Kronecker delta
δ_t	thermal boundary layer thickness
δ_{z0}	laser light sheet thickness for PIV
D	LES filter width

e	turbulent kinetic energy dissipation rate
h	flow effectiveness, $h = (T_\infty - T)/(T_\infty - T_c)$
h_{aw}	adiabatic film cooling effectiveness, $h_{aw} = (T_\infty - T_{aw})/(T_\infty - T_c)$
k	von Kàrmàn constant
l	laser wavelength
m	dynamic viscosity
n	kinematic viscosity
η_t	eddy-viscosity, also referred to as turbulent viscosity
q	dimensionless temperature
Q	transformed dimensionless temperature
r	density
s	Stefan-Boltzmann constant
t	time scale
t_p, t_f	particle response time and flow time scale
t_k, t_0	Kolmogorov and integral time scale
t_{ij}	subgrid-scale shear stress tensor
τ_w	wall shear stress

Superscripts and subscripts

0	variable evaluated at the casing
∞	variable evaluated at the hot mainstream
aw	variable evaluated at the adiabatic wall
b	variable evaluated at the thermocouple bead

<i>c</i>	variable evaluated at the slot coolant
<i>p</i>	variable evaluated at the seeding particle (TiO_2)
<i>rms</i>	root mean square of a variable
<i>sgs</i>	subgrid-scale variable
<i>w</i>	variable evaluated at the wall
<i>wb</i>	variable evaluated at the backside wall

Conventions

\cdot^+	variable in wall units
$\hat{\cdot}$	test filter
$\bar{\cdot}$	grid filtered variable (LES) or Reynolds averaged variable (RANS)
$\langle \cdot \rangle$	time and ensemble average

Chapter 1: Introduction

The extreme pressure and temperature conditions of modern rocket and gas turbine engines are responsible for the extreme thermal loads experienced by several critical engine components. Among these critical components one can mention the combustor liner and the turbine blades of gas turbine engines, as well as the thrust chamber assembly and the nozzle in rocket engines. In past decades, the constant increase in efficiency and power was a direct consequence of higher operating pressure and temperature in the combustion chamber. However this trend is limited by the ability of critical structural elements to withstand these conditions.

1.1 Motivation: Critical Aspects of Film Cooling

A variety of techniques have been developed to protect critical components from the hot flowpath inside an engine. In gas turbine engines, the combustor liner is convectively cooled with bleed air from the compressor. Small orifices and slots are machined in the combustor liner in order to allow cool air to penetrate inside the combustor by forming a protective film that convectively cools the hot surface. This widely used technique, known as film cooling, remains the major thermal protection mechanism used in gas turbine engines for the combustor as well as the turbine blades [1]. Rocket engines thermal protection techniques can be categorized into three families: ablation, radiation, and convection cooling [2]. In ablation cooled applications, a small amount of material is continuously eroded thus creating a layer in the process that protects the hot surface. This technique is mostly used in solid propellant rockets and

thermal protection systems for reentry vehicles. Radiation cooling makes use of the sometimes large heat fluxes associated with the thermal radiation of a hot surface in a cooler surrounding. While this method may require large exchange surfaces, it takes full advantage of the low temperature of outer space. Critical components of larger rockets are protected by convection cooling, which includes regenerative, backside and film cooling techniques.

Along with regenerative cooling and backside cooling, film cooling is the major technique used to protect large rockets, such as the J-2X engine that will be used to launch the Crew Exploration Vehicle (CEV). Although film cooling is a successfully used technique, the fundamental phenomena governing the mixing of the film are not well understood. Consequently there is a need for detailed measurements to further enhance the current understanding of the turbulent near-wall transport physics and the mixing of the film. Furthermore, since the aerospace community is relying more heavily on Computational Fluid Dynamic (CFD) tools to support Research and Development (R & D), there is a growing need for accurate high-fidelity models as those used for Large-Eddy Simulations (LES). Indeed, wall resolved LES of high-speed wall bounded flows lead to high computational costs due to high Reynolds numbers and large separation of scales of motion. The computational cost associated with such detailed simulations can be prohibitive for component level R & D applications. From this perspective, comprehensive wall models derived from a deep understanding of the physics are critical for future R & D initiatives.

1.2 Position of Problem

Slot film cooling represents both a practical and canonical flow configuration for film cooling applications, as pictured in Figure 1. Such a configuration is present in the primary zone of a gas turbine combustor, in a rocket thrust chamber and nozzle extension. Because of its simple geometry, this flow constitutes a canonical configuration suitable for experimental, analytical, and numerical evaluation of the transport physics governing film-cooling performance. In contrast, discrete hole cooling has recently received significant attention in the literature, but variations in the hole geometry or hole arrangement make it difficult to evaluate general characteristics of turbulent mixing for propulsion applications.

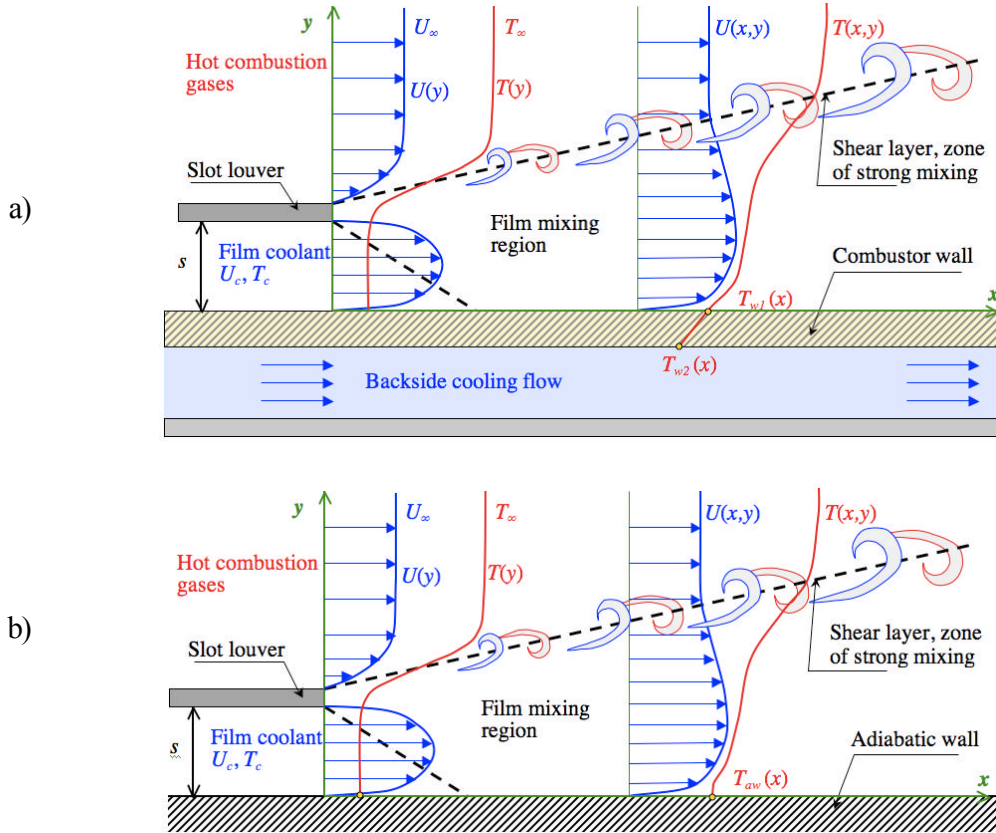


Figure 1. Slot film cooling configuration: a) with backside cooling; b) adiabatic wall

In most engineering applications, film cooling is used with backside cooling (Figure 1-a) to enhance the thermal protection of the wall. For liquid propellant rockets the cryogenic fuel is heated in the backside cooling process. This pre-heated fuel can be injected directly in the combustion chamber (gas generator cycle), used to drive the turbines of the turbo-pumps (expander cycle) or injected in the pre-combustor (staged-combustion cycle) as in the Space Shuttle Main Engine (SSME) [2]. The adiabatic wall configuration presented in Figure 1-b represents a canonic configuration often used to evaluate the mixing of the film and the associated film cooling effectiveness. The adiabatic wall temperature, as we will see, is an important concept because it represents the reference temperature used to calculate the convective heat flux at a film-cooled wall.

Despite the fact that the 2D slot configuration provides a statistically two-dimensional flow, three-dimensional turbulent structures develop in the flow and produce strong mixing. Of particular interest is the interaction between the coolant and hot gas streams in the shear layer, as illustrated in Figure 1. The temperature of the film near the injection point is virtually unaffected by the hot gases. However, further downstream the flow is characterized by a region of intense mixing. The mainstream mixes with the coolant flow, thereby increasing the temperature of the flow near the wall and reducing the protective effects of film cooling.

1.3 Literature Review

In this section, we present previous work relative to slot film cooling from an experimental, analytical and numerical point of view. An overview of the main achievements brings to perspective the main advances in the understanding of this problem and the challenges that remain to be addressed.

1.3.1 From early experiments to engineering correlations

We begin with an historical overview, and then present the derivation of film cooling effectiveness, which leads to the description of the governing physics of the flow. Finally the physical grounds for the use of engineering correlations for film cooling flows is presented, and their limitations mentioned.

Historical perspective

The physics of film cooling have been studied with great interest during early developments of gas turbine engines. Experimental and analytical investigations lead to the derivation of semi-empirical correlations that attempt predicting the effects of film injection on heat transfer to hot surfaces. Surprisingly, one of the most prominent studies in this area dealt with the problem of deicing of wings. In 1946, Wieghardt [3] investigated the injection of warm air through a two-dimensional slot as a de-icing device by looking at the entrainment of the film by the mainstream as a function of the injection angle for different blowing ratios. He also proposed a similarity expression for the dimensionless gas phase temperature profiles (based on the local adiabatic wall temperature) as a function of the local thermal boundary layer thickness. Later, measurements and analysis by Hartnett et al. [4] extended Wieghardt's work and provided an expression for film cooling effectiveness consistent with an expression previously derived by Tribus and Klein [5]. Following these early developments Stollery and El-Ehwany [6] derived a simple correlation for slot film cooling effectiveness based on an enthalpy balance. The issue of the scatter on film cooling effectiveness experimental data [4] was also addressed. Although there exist small slot geometrical differences, they point to the fact that slot Reynolds numbers were not considered in the

comparison. This oversight resulted in inappropriate comparison of data having different turbulent inlet conditions. This remark points out the need for well-characterized inlet conditions with mean profiles and turbulence statistics to identify effects of turbulence intensity in film cooling effectiveness decay. However, these measurements were difficult to perform and most studies relied on the slot Reynolds number to characterize the turbulence. But since the adiabatic film cooling effectiveness is a measure of the mixing of the film, Marek and Tacina [7] suggested that the correlation should depend on streamwise turbulence of the mainstream through a mixing coefficient C_m . Based on their measurements they concluded that this coefficient could not remain constant along the wall because it would lead to a $\pm 30\%$ deviation between their correlation and experimental data.

Later Simon [8] considered the wall normal turbulence intensities of the freestream and the slot exit flow. Through a clever wall jet analysis with separate treatment of the jet zone and the mixing zone, Simon was able to develop a 1D-mixing model for the film-cooling flow. This model predicts the film cooling effectiveness within $\pm 4\%$ of the Marek and Tacina experimental data from which it was developed. Simon also describes an iterative computational method to determine a local mixing parameter equivalent to Marek and Tacina mixing coefficient C_m .

However most correlations commonly used rely on the slot Reynolds number as the sole turbulence parameter, and were developed based on the fully developed turbulent boundary layer asymptotic solution and the constant gas properties assumption because of small temperature gradients in the far field. Therefore these correlations could not be applied in the near injection region where large gradients exist, and the turbulent

boundary layer is not fully developed. In an attempt to describe the film cooling effectiveness in the near slot region, Ballal and Lefebvre [9] used previous analysis and direct measurements of the skin friction coefficient near the slot ([10],[6]) to derive an expression for the film cooling effectiveness in this region of interest. After empirical correction for the Reynolds number exponent and the constants their correlation showed good agreement with experimental data ($\pm 5\%$). For high blowing ratios, they also derived an expression for the effectiveness based on wall jet theory. Several authors have proposed other simple correlations for the effectiveness. In 1971 Goldstein [11] provided a comprehensive review of those scaling laws.

Derivation of film cooling effectiveness correlations

Film cooling effectiveness correlations can be derived from an enthalpy balance. At any given downstream position x , the excess energy introduced by the film must be equal to the energy introduced at the exit of the slot [4],

$$\int_0^d \rho U W C_p (T - T_\infty) dy = \rho_c U_c s W C_p (T_c - T_\infty) \quad (1)$$

In this equation, d is the boundary layer thickness at x , s is the slot height and W is the slot width. T , ρ and U are the temperature, density and velocity, respectively, of the flow at the exit of the slot with subscript c and of the freestream with the subscript ∞ . The specific heat at constant pressure C_p is assumed constant. The integral on the left hand side can be rearranged by introducing the difference between adiabatic wall temperature and freestream temperature, $(T_{aw} - T_\infty)$, and the freestream density and velocity, to yield:

$$\int_0^d \rho U W C_p (T - T_\infty) dy = \rho_\infty U_\infty W C_p (T_{aw} - T_\infty) \int_0^d \frac{\rho U}{\rho_\infty U_\infty} \frac{T - T_\infty}{T_{aw} - T_\infty} dy \quad (2)$$

Making use the 1/7th power law approximation for a turbulent boundary layer the mass flux ratio can be expressed as [4],

$$(rU)/(r_\infty U_\infty) = (y/d)^{1/7} \quad (3)$$

Then assuming x is far enough downstream of the slot exit for the temperature profile to be fully developed, the similarity expression of Wieghardt [3] is used to express

$$\frac{T - T_\infty}{T_{aw} - T_\infty} = \exp\left(-c\left(\frac{y}{d}\right)^{13/6}\right) \quad (4)$$

The exponential term in Eq. (4) contains a constant c (determined experimentally) and can be expanded in Taylor series before inserting into Eq. (2). The result of the integral is a constant times the boundary layer thickness d . Then assuming that $d \propto x \text{Re}_x^{-1/5}$ the left hand side of Eq. (1) becomes

$$\int_0^d r U W C_p (T - T_\infty) dy = r_\infty U_\infty W C_p (T_{aw} - T_\infty) c' \frac{x}{\text{Re}_x^{1/5}} \quad (5)$$

Then, regrouping, simplifying and rearranging Eq. (1) the following relation is obtained [4]:

$$\frac{T_{aw} - T_\infty}{T_c - T_\infty} = c_2 \left(\frac{r_c U_c}{r_\infty U_\infty} \right) \frac{s}{x} \text{Re}_x^{1/5} \quad (6)$$

The term on the left hand side is the adiabatic film cooling effectiveness, noted \hbar ,

$$\hbar = \frac{T_{aw} - T_\infty}{T_c - T_\infty} \quad (7)$$

The effectiveness takes values between one, near slot exit, and zero far downstream when the protective effect of the film has vanished. The effectiveness thus represents the

mixing of the film or the dimensionless temperature of the gas near the wall in the adiabatic wall case. Based on this simple analysis, this important parameter depends on: the local downstream position, the local Reynolds number, the slot height, and the blowing ratio m defined by

$$m = \frac{r_c U_c}{r_\infty U_\infty} \quad (8)$$

Traditionally, the slot Reynolds number Re_s is often preferred over the local Reynolds number because it represents a global inlet parameter. It is based on the slot height and slot exit velocity and fluid properties

$$Re_s = \frac{r_c U_c s}{m_c} \quad (9)$$

With some algebraic manipulations the local Reynolds number is related to the slot Reynolds number, the blowing ratio, slot height, and viscosity ratio

$$Re_x = Re_s \left(\frac{m_c}{m_\infty} \right) \left(\frac{x}{ms} \right) \quad (10)$$

Finally substituting this relation into Eq. (6) yields the classical expression for the film cooling effectiveness based on a turbulent boundary layer analysis [4]

$$\eta = \frac{T_{aw} - T_\infty}{T_c - T_\infty} = c_2 \left(\frac{x}{ms} \right)^{4/5} Re_s^{1/5} \left(\frac{m_c}{m_\infty} \right)^{1/5} \quad (11)$$

This expression demonstrates the dependency of the film cooling effectiveness on downstream position and inlet operating conditions. The constant can be determined analytically, but is most often determined using experimental data [1]. This expression was derived based on the assumption of fully developed turbulent boundary layer which

is only valid far downstream of the slot exit. Ballal and Lefebvre proposed a similar expression based on measurements of the skin friction that is valid near the slot exit for blowing ratios less than 1.3 [9]

$$h = 0.6 \left(\frac{x}{ms} \right)^{0.3} \left(Re_s \frac{m \cdot m_c}{m_\infty} \right)^{0.15} \quad (12)$$

For blowing ratios greater than 1.3, a piecewise expression based on turbulent wall jet theory has been developed [9]

$$h = \begin{cases} 1 & x/(ms) < 8 \\ (0.6 + 0.05 x/(ms))^{-1} & 8 \leq x/(ms) \leq 11 \\ 0.7 \left(\frac{x}{ms} \right)^{-0.3} \left(Re_s \frac{m_c}{m_\infty} \right)^{0.15} m^{-0.5} & x/(ms) > 11. \end{cases} \quad (13)$$

However close attention to this expression reveals discontinuity depending on values of Re_s , μ_c/μ_∞ and m at the junction point $x/(ms)$ equal to 11. Consequently the Simon jet model is preferred for wall jet configurations.

Film cooling heat transfer using engineering correlations

Engineering calculations of convective heat flux usually rely on Newton's law of cooling, $q''_w = h_x (T_{ref} - T_w)$, with reference temperature taken as the bulk temperature for channel or pipe flows, or freestream temperature for external boundary layers. However for film cooling flows the choice of the reference temperature is not obvious because of the mixing of two streams with different temperatures. Goldstein demonstrated that the adiabatic wall temperature, T_{aw} , is the reference temperature that leads to zero convective heat flux in the case of a perfectly insulated wall [11]. Even though it represents an ideal condition, the adiabatic wall temperature has a double importance for film cooling flows:

it describes the mixing of the film when non-dimensionalized (i.e. film cooling effectiveness) and it is the reference temperature for Newton's law of cooling. Consequently, for film cooling applications the convective heat flux is conventionally written as

$$q''_{conv} = h_x(T_{aw} - T_w) \quad (14)$$

In this expression h_x is the local convective heat transfer coefficient and T_w is the temperature of the non-adiabatic film cooled wall. The two unknowns of this engineering problem are h_x and T_{aw} . Knowing the inlet conditions, the adiabatic wall temperature can be determined with a correlation for the film cooling effectiveness, as described above. The convective heat transfer coefficient can be calculated using the appropriate Nusselt number correlation depending on the blowing ratio [1]

$$Nu_x = \frac{h_x x}{k_c} = \begin{cases} 0.069 (\text{Re}_s x/s)^{0.7} & 0.5 \leq m \leq 1.3 \\ 0.10 \text{Re}_s^{0.8} (x/s)^{0.44} & m > 1.3 \end{cases} \quad (15)$$

where k_c is the thermal conductivity of the cooling film. Having determined the convective heat transfer coefficient and the film effectiveness, the convective heat transfer at a film cooled wall can then be easily estimated by

$$q''_{conv} = h_x(T_\infty - \hbar(T_\infty - T_c) - T_w) \quad (16)$$

It is worth noting that the success of this approach is limited by the accuracy of the correlations for h_x and \hbar and the validity of the assumptions they are based on. If a semi-empirical mixing model (for \hbar) is chosen it may not be able to account for the effects of turbulence intensity and large disturbances into the prediction of effectiveness. A possible alternative is to use the iterative method of the Simon's mixing model [8] to

calculate the film cooling effectiveness. In addition to inflow mean quantities (T_∞ , T_c , U_∞ and U_c) this method also requires as input the wall normal turbulence intensities at the exit of the slot and in the freestream. This model has been validated for blowing ratios between 0.5 and 1.9 and showed good agreement with experimental data. It has only been validated up to a distance of 34-slot height downstream of the injection [8]. However it has been shown to perform relatively well further downstream [12].

1.3.2 Numerical Simulations

With increasing computational power, computational fluid dynamics (CFD) models are gaining widespread use. For the past two or three decades, despite their well-documented weaknesses Reynolds Averaged Navier-Stokes (RANS) models have been very popular within the engineering community. Recently, large-eddy simulation (LES) has been applied to flows of engineering interest. This transition towards LES models is clearly evidenced in their availability in commercial CFD packages (e.g. Fluent, StarCD). However to the author's knowledge there is no large-eddy simulation study of slot film cooling with scalar transport available in the open literature. In this section most relevant numerical works to the problem are reviewed.

RANS studies

In the RANS fundamental framework all turbulent scales of motion are modeled. A large variety of closure models exist, one-equation, two-equation and algebraic stress models. Calibration of the model constants can be a crucial and difficult task for the performance of most advanced RANS closure models. Wilcox [13] examined the performance of most commonly used RANS models over several test flows for which reliable experimental data exist. Test flows include free-shear flows (mixing layer, far

wake, plane and radial jet), boundary layer flows, and separated flows (backward facing step). By this thorough examination Wilcox concluded that the standard k - e model performs poorly for all the flows except the mixing layer and plane jet. By contrast the k - w model predicts satisfactorily all the flows considered. Wilcox also showed that the single equation Spalart-Allmaras model also shows good agreement with all the test flows, except for the plane jet case [13]. Despite its simplicity, the Spalart-Allmaras performs well in its standard form, whereas two-equation models are sometimes adapted or modified to certain flow configurations such as the wall-jet [14].

In a film cooling numerical simulation study, Zhou, Salcudean and Gartshore [15] modeled turbulence using a k - e model with a near-wall low-Reynolds-number k model and also a k - e model with a wall function. For blowing ratio less than 0.4, their simulation results were in good agreement with the experimental data for velocity profiles and cooling effectiveness. Jansson, Davidson and Olsson [16] modeled film cooling through a slot by an algebraic stress model and a standard k - e model. The numerical results showed good agreement with experiments for velocity profiles but, surprisingly, the comparison for gas temperature profiles showed significant differences, especially near the wall. The authors pointed to measurement issues and problems with the way diffusive terms were modeled in the transport equation for temperature to explain these differences. Jia et al. [17] performed simulation of a slot film-cooling flow with injection angles ranging from 16 to 90°, using k - w and k - e RANS models. The comparison of the simulation results with Laser Doppler Velocimetry (LDV) measurements showed good agreement, but the temperature profiles tended not to agree as well, especially in the near-wall and shear regions. Wall temperatures of film cooling

effectiveness were not compared to experimental data, although this exercise would have proved useful in validating the simulation results.

LES based studies

In the past decade LES has gained interest in the engineering community, even though wall resolution remains a challenge for complex geometries and high Reynolds number flows. To reduce the computational cost of LES of wall-bounded flows, Spalart et al. [18] suggested a hybrid approach making use of RANS near the wall and LES further away. This hybrid technique is commonly referred to as Detached-Eddy Simulation (DES). Most LES or DES studies of film cooling focus primarily on discrete holes, with a few exceptions directly relevant to the present problem.

Recently, Roy, Kapadia and Heidmann [19] implemented the DES approach to solve film-cooling flow on a flat plate with coolant injection through a single inclined cylindrical hole. Their results demonstrate a strong anisotropic mixing behavior, which is not captured by RANS alone. However the numerical results are limited due to the symmetric boundary condition imposed on the domain. This computational issue was later resolved in a subsequent technical note [20]. Analysis of the results confirms the anisotropic mixing behavior. When compared to experimental data, the centerline cooling effectiveness tends to be over-predicted but the spanwise averaged is slightly under-predicted. Muldoon and Acharyan [21] performed a Direct Numerical Simulation (DNS) of a similar flow configuration with a single hole inclined at 35 deg., at a Reynolds number of 3068 (based on the hole diameter). Based on the DNS results they computed all the terms in $k-e$ transport equations and compared their values those of the modeled $k-e$ terms. The Boussinesq gradient approximation, as used in standard $k-e$, was

shown to be a reasonable model but the eddy viscosity contained large errors. A new damping function for the eddy-viscosity was proposed.

Martini et al [22] performed simulation of slot film cooling at the trailing edge of a turbine blade, using steady RANS k - w and DES. For all the blowing ratios considered, the predicted film cooling effectiveness using DES is in good agreement with experimental data, whereas k - w largely over-predicts the effectiveness. Non-adiabatic cases were also considered. In this case the convective heat flux is prescribed at the wall boundary condition. Martini et al. [22] only report the convective heat transfer coefficient. For this quantity both k - w and DES models give good results. However the authors forgot to consider that this is merely a coincidence in the k - w case. Considering that $h = q_{conv}/(T_{aw} - T_w)$, that the heat flux is prescribed, and that the adiabatic wall temperature is under-predicted, it follows that the good agreement resulted from an under-prediction in the wall temperature. Although this configuration resembles that of the present study, it differs because of a slightly inclined slot and a large louver lip thickness, generating much larger shear.

A wall resolved LES of an isothermal plane turbulent wall jet at a Reynolds number of 9600 was performed by Dejoan and Leschziner [23]. Even though the wall jet is in a stagnant environment, and thus the flow configuration differs from the present study, this detailed work presents an examination of the inner and outer scaling. In the self-similar region, the flow scales in wall units (friction velocity) in the inner region whereas it scales with the maximum velocity in the outer region. More importantly a thorough analysis of the turbulent energy and stresses budgets shed light into the turbulent transport responsible for the interaction between both regions. Shear-stress

budget indicates that the negative production is balanced in the near-wall region by the velocity-pressure and turbulent diffusion terms, the later playing an important role in identifying the interaction region. In the outer region, the positive production is balanced almost exclusively by the velocity-pressure term. Furthermore, the ratio of turbulent kinetic energy production to dissipation shows significant differences with turbulent channel flow at a similar Re_t , the main difference being the lack of equilibrium for the wall jet flow due to the contribution of the turbulent diffusion from the outer layer towards the wall. Consequently, for the wall jet, the region where the log law holds is very limited.

A direct numerical simulation of plane turbulent wall jet with scalar mixing was performed by Ahlman et al. [24] for a slot Reynolds number equal to 2000 and Mach number equal to 0.5. The flow configuration resembles that of a wall jet in a stagnant environment since the velocity ratio, U_c/U_∞ , was equal to 10 for this simulation. The passive scalar was introduced in the slot flow to study the mixing characteristics. The authors found the scalar mixing to behave like the streamwise velocity mixing. In addition, the scalar turbulent fluxes are shown to be of comparable magnitude in the streamwise and wall-normal directions [24].

1.3.3 Summary of previous work

Previous experimental studies have placed significant emphasis on the wall temperature (i.e. effectiveness). However as recent numerical studies pointed out, it appears that near wall temperature profiles and the corresponding wall heat flux are difficult to predict accurately [16], [22]. High quality flow and wall temperature measurements under realistic flow conditions (blowing ratio, temperature ratio, slot

Reynolds number, turbulence intensity) are needed to help develop and validate emerging near-wall mixing and heat transfer models for film cooling applications.

In addition, there is some discrepancy in the performance of different RANS models. Spalart-Allmaras may be a viable candidate for the present flow. LES and DES appear to be promising tools to investigate the physics of the flow. Although wall resolved LES has been used for a similar flow it has not yet been applied to slot film cooling with scalar transport.

1.4 Objectives

The primary objective of the present study is to characterize the mixing and near-wall transport of the turbulent slot film-cooling problem. Because of the lack of detailed experimental data for this configuration in the literature, the first objective is to obtain a detailed and comprehensive database of slot film cooling experimental data over a large parameter space under realistic conditions. Consequently we consider three flow configurations with different coolant to mainstream velocity ratios characteristic of a wall-jet, a wall-wake and a boundary layer. In addition to the adiabatic wall configuration, a non-adiabatic wall thermal boundary condition is added to study heat transfer in slot film-cooling configurations. The intended database ought to include not only measurements of wall quantities but also flow quantities such as velocity and temperature, and well-characterized inflow conditions. From this comprehensive experimental database, mixing phenomena and near-wall transport can be analyzed to characterize this flow.

The numerical simulations aim first at investigating the performance of the RANS Spalart-Allmaras model in order to reconcile and classify the disagreements observed in

the literature. This study also seeks to analyze the performance of LES for this flow configuration by comparing to RANS results and experimental data. From wall resolved and validated LES data, key turbulent mixing information can be analyzed to further improve our understanding of this flow. Because these turbulent quantities are nearly impossible to obtain experimentally, they provide valuable information in the effort to characterize near-wall mixing and heat transfer behavior in slot film cooling flow.

1.5 Main Achievements

Several significant achievements were accomplished in the course of this research both experimentally and numerically. First of all, a unique hot wind tunnel facility was designed and built to study film cooling mixing and heat transfer. Minimally intrusive and non-intrusive diagnostics were applied to characterize near-wall mixing behavior. A special micro-thermocouple probe was built. With its fast response time and spectral digital compensation of its thermal inertia high frequency temperature fluctuations are recovered thus providing a unique opportunity to characterize the thermal mixing associated with this flow. For LDV and PIV measurements, two solid particle seeders using the fluidized bed principle were designed and built to deliver steady and uniform TiO₂ seeding to the coolant and the hot streams. With the help of Fernando Raffan, the test facility was upgraded with backside cooling to study cases with wall heat flux. Heat flux level through the wall can be adjusted by regulating the backside coolant flow temperature. In this configuration the wall backside temperature is nearly uniform, thus representing a simple boundary condition for numerical simulations. Wall heat flux and temperature were successfully measured in this configuration and near-wall velocity measurements were achieved using PIV and a special wall treatment.

The numerical solver used in this study derives from an existing LES solver developed by Anthony Keating ([25], [26]). The solver was modified to include the energy transport equation and the necessary boundary and initial conditions. The dynamic eddy-diffusivity sub-grid scale model was implemented for LES and the Spalart-Allmaras model for RANS. New modifications to the code were validated against DNS and experimental data. Therefore the solver was used with confidence to tackle the difficult problem of slot film cooling which had never been published before.

Chapter 2: Experimental and Numerical Methodology

The purpose of this chapter is to describe the methodology used in this study. Because previous experimental studies have been mostly concerned with studying the effects of isolated global parameters (i.e. turbulence intensity, geometry, Reynolds number) on the film mixing, this study focuses more on the fundamental mechanisms that cause the mixing of the film. As a result detailed turbulent characteristics of the flow need to be measured and correlated to the film mixing dynamics. Such an endeavor requires comprehensive detailed measurements of the flow at the inlet and in the mixing region (i.e. temperature and velocity) and the temperature and heat flux (when applicable) at the wall. Details about the experimental facility, diagnostics, and post-processing techniques are provided in section 2.1.

Since large-eddy simulations of a two-dimensional slot film cooling with scalar mixing have never been published, it appears critical to further understand the physics governing the film mixing from a numerical point of view. Consequently, performing wall resolved large-eddy simulations of experiments provides a unique perspective on the problem. Furthermore, the performance of the RANS Spalart-Allmaras model will be evaluated in this work. Details about the solver, the numerical methods and turbulence models are presented in §2.2.

Finally in the last sub-section, the LES and RANS models are validated against experimental and DNS data of a fully developed channel flow with heat transfer.

2.1 Experimental Measurements and Analysis

A hot wind tunnel facility was specially designed and constructed for the study of near-wall mixing and heat transfer under conditions relevant to gas turbine engines and rocket thrust chambers. In this section we will first proceed with a description of the hot wind tunnel facility and its specific components. Then the diagnostics will be presented along with the data post-processing techniques that were used to obtain the experimental results. A brief section on measurement uncertainties will close the description of the experimental measurements.

2.1.1 Description of the hot wind tunnel facility

As portrayed in Figure 2, the hot wind tunnel facility is an open circuit system that includes a centrifugal fan, an inline methane burner, a 90-degree elbow with turning vanes, a settling chamber with flow control devices, and a two-dimensional convergent section with a contraction ratio of 6:1. In the test section, a high capacity compressor delivers compressed air that is injected through a louvered slot to create a tangential film. Downstream of the test section an optimized two-dimensional diffuser reduces pressure losses. A duct connects the exit of the diffuser to a large hood equipped with a blower. As result of the wind tunnel arrangement the pressure in the test section is less than the atmospheric pressure. The hot wind tunnel provides a realistic experimental configuration to investigate heat transfer in rocket thrust chambers and gas turbine engines. The wind tunnel produces operating conditions relevant to real engine conditions with velocity ratios U_c/U_∞ ranging from low values of 0.5 (relevant to rocket engines) to high values up to 3 (relevant to gas turbine engines), and maximum absolute temperature ratios T_∞/T_c up to 2. Blowing ratios, m , ranging from 0.75 (relevant to rocket

engines) up to 5 (relevant to gas turbine engines) can be achieved under thermally aggressive conditions. It should be noted that the peak temperatures in the laboratory configuration are limited when compared with actual engines, particularly rockets (175 K min, and 3500 K max). Also the experimental slot injection Reynolds numbers Re_s , are significantly smaller than those found in propulsion applications; however, they are still in the turbulent regime, ranging from 2000 to 6000.

This facility uses a centrifugal fan equipped with a backward curved airfoil impeller and powered by a direct drive 3-phase 1.5 HP electric motor. A frequency controller allows selecting the speed of the fan, and consequently controls the velocity of the mainflow in the wind tunnel. When laser diagnostics are in use, solid particles of titanium dioxide (TiO_2) are injected in the flow by means of counter flow jets to enhance mixing. Downstream of the fan, an inline methane burner is mounted inside the flame tube. The pilot flame of the burner is remotely ignited with a 6000 Volt spark plug. The

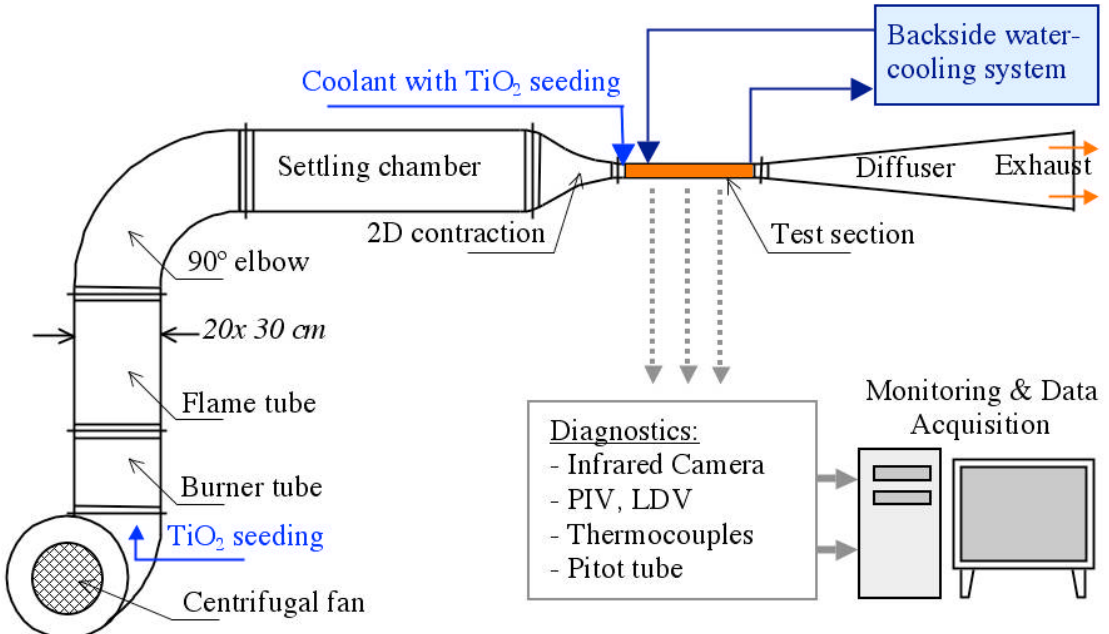


Figure 2. Hot wind tunnel facility layout

methane flow rate is measured with a rotameter and controlled during the experiments to ensure steady operating conditions. A significant part of the flow bypasses the burner to provide dilution of the flame before entering the 90-degree elbow. The elbow is equipped with turning vanes to reduce pressures losses in the wind tunnel.

The main purpose of the settling chamber is to provide a well characterized homogeneous flow upstream of the contraction section. Given the cross section of the wind tunnel, 20 x 30 cm, and the operating conditions, the settling chamber was designed to be 100 cm long. Several flow-controlling devices are present in the settling chamber. First a 10-cm long obstruction made of randomly packed ceramic saddles is mounted at the inlet of the settling chamber. While posing little resistance to the flow this obstruction serves as a buffer that thermally mixes and homogenizes the flow containing large temperature fluctuations induced by the burner and the dilution process. Downstream of the ceramic bed a welded stainless-steel honeycomb breaks the large eddies and reduces the components of the velocity in the wall-normal and spanwise direction. The characteristic cell diameter and length, respectively 3.17 mm and 15.87 mm, were specified based on recommendations by Mehta and Bradshaw [27]. A fine mesh stainless steel screen is placed at the exit of the settling chamber and 50 cm downstream of the honeycomb to further homogenize the velocity and reduce the boundary layer thickness. The screen is made of 0.165 mm diameter stainless steel wires with 900 meshes per square inch, resulting in an open area of 64.8%. The two-dimensional convergent section with a contraction ratio of 6:1 is made of stainless steel and mounted downstream of the settling chamber. Because thermal losses through the walls and thermal boundary layer growth are not desired in this controlled heat transfer

experiment, both the settling chamber and the convergent section are thermally insulated with one-inch thick Kaowool® boards.

Test section

The test section is a stainless steel flanged channel 200 by 50 mm in cross-section and 500 mm in length, directly connected to the convergent exit section. The test section is equipped with several optical access windows and ports as illustrated in Figure 3. The louvered slot is mounted to the test plate allowing for an easy modification of the slot's geometrical characteristics. In the present work, the slot height, s , is set to 4.0 mm and the louver is 0.76 mm thick and 50 mm long. The film flow is injected through discrete holes 3.17 mm in diameter separated by 6.35 mm. The resulting small jets impinge on

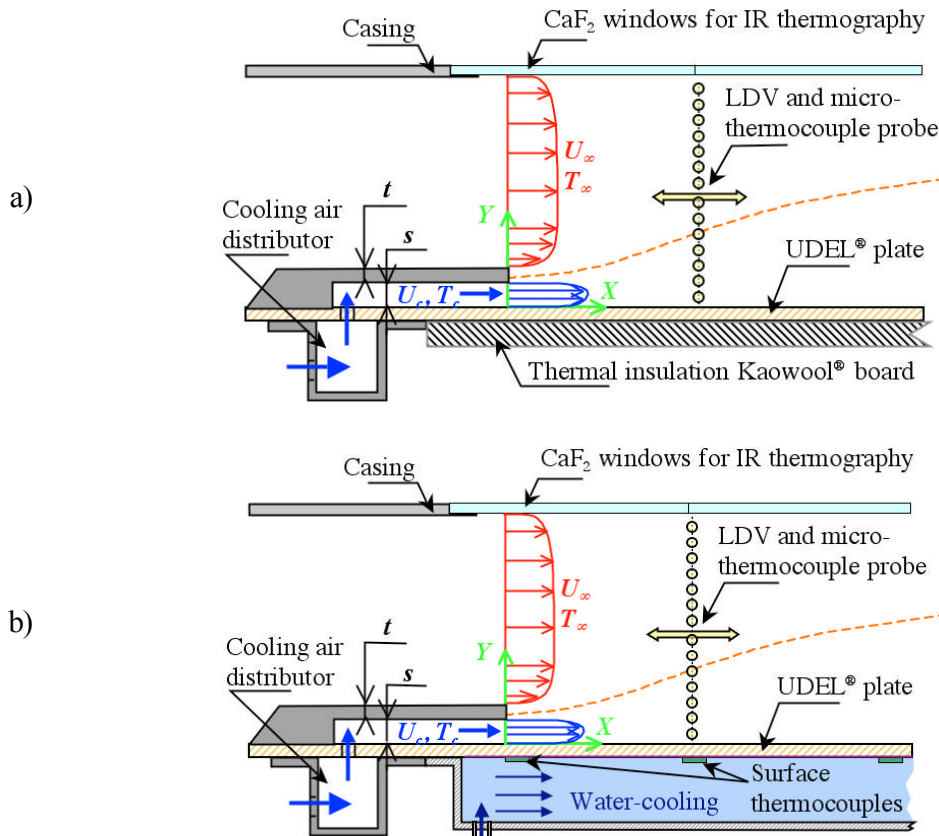


Figure 3. Test section description, a) Adiabatic wall experiment configuration, and b) Non-adiabatic wall experiment for heat transfer measurements.

the louver to create a film at the exit of the slot. The test plate (200 by 500 mm and 6.35 mm thick) is made of UDEL®, a high temperature polycarbonate with a low thermal conductivity of $0.24 \text{ W}\cdot\text{m}^{-1}\cdot\text{K}^{-1}$. This low conductivity material provides a large temperature gradient across the test plate for accurate measurement of the heat flux through the plate in the non-adiabatic experiments. In adiabatic experiments, this material provided the first layer of thermal insulation to prevent heat losses from the wall.

For adiabatic wall experiments the back surface of the test plate is insulated with a 1-inch-thick Kaowool® board, as illustrated in Figure 3a. This insulation material has a low thermal conductivity of $0.06 \text{ W}\cdot\text{m}^{-1}\cdot\text{K}^{-1}$ providing an efficient insulation. The measured adiabatic wall temperature yields the film cooling adiabatic effectiveness, an important parameter describing the mixedness of the film cooling flow with the hot mainstream.

In the heat transfer experiments, the thermal insulation is removed and replaced by a stainless steel cooling channel, as shown in Figure 3b. Cooled-water ($9\text{-}10^\circ\text{C}$) flows inside this channel, thus removing heat from the backside of the wall by forced convection. A pump drives water from a tank to the test section and back to the tank. Because of the choice of this closed loop system, the tank is equipped with a heat exchanger that keeps the water temperature constant during the entire experiment. Given the high thermal capacity of water and the high flow rates considered (10-20 gpm) the backside temperature of the wall was nearly uniform along the streamwise and spanwise directions. This simple thermal boundary condition provides ideal conditions for direct comparison with numerical simulations. For additional details the reader is referred to Cruz and Marshall [12].

2.1.2 Measurement techniques

The hot wind tunnel is equipped with several instruments to provide a comprehensive and detailed characterization of the slot film-cooling problem. The inlet temperature and velocity are carefully measured. Detailed flow temperature and velocity measurements provide valuable information about the film mixing mechanisms. Wall surface temperature and heat flux (when applicable) are also measured, thus providing a characterization of the thermal boundary conditions of the problem.

Inlet characterization

The velocity and temperature of the hot mainstream inlet flow is measured with a specially designed small pitot tube equipped with a micro-thermocouple attached parallel to the total pressure tube. The total and static pressure tubes are made of small stainless steel tubes 1/16" in outer diameter. The type K thermocouple probe is made of bare wires with 50 μ m diameter that are threaded through a two-holed ceramic tube. This probe assembly is attached to the casing and can be traversed in the wall-normal direction to acquire inlet profiles and perform uniformity checks at the operating conditions. The pressure is measured with a pressure transducer that outputs a current proportional to the pressure, while the thermocouple probe outputs a voltage. The corresponding analog signals are digitized using a Labview DAQ data acquisition board with a sampling rate of 1 kHz. A Labview program was specially developed to calibrate and process the information yielding the velocity and temperature of the hot mainstream.

The temperature of the flow exiting the slot is measured with a micro-thermocouple placed inside the slot with a sufficient offset from the main (x, y) measurement plane pictured in Figure 3. The bulk velocity at the exit of the slot is

calculated by using mass conservation between the rotameter and slot exit sections. The bulk velocity is an important parameter for this channel flow configuration. Most importantly, the bulk velocity is also the reference velocity to use when calculating the blowing ratio and slot Reynolds number [1].

Inlet velocity profiles are also measured using Particle Image Velocimetry (PIV), which are in good agreement with the pitot measurements. Because of the higher spatial resolution and lower measurement uncertainty of the PIV, these inflow measurements are taken as the reference velocity profiles in this study.

Flow velocity measurement

The flow velocity is measured using a minimally intrusive laser based technique, Particle Image Velocimetry (PIV). This technique was first described by Adrian [28] and Pickering and Halliwell [29]. In these two papers the principle of particle image velocimetry is introduced, which contrasts with laser speckle velocimetry. PIV utilizes small particles that follow precisely the flow structures and scatter light from a laser light sheet. The laser emits light for short time durations or pulses. This strobining effect allows visualizing the ‘frozen seeded flow’ by means of an optical system and a photographic camera, which today is replaced by a digital CCD camera. This strobining effect results in several images of the flow being frozen in time where the light scattered by the particles is clearly visible. The PIV principle makes use of two successive frames separated by a time interval, dt , small enough to guarantee optimum displacement of particles between two frames. Applying the PIV technique to the present study posed several challenges, such as correctly seeding the coolant and hot streams, imaging the particles, and reducing laser scatter at the wall to obtain near wall measurements given the small dimensions of

the experimental setup.

a) Seeding the flow

The particles introduced in the flow serve as tracer particles for the imaging system. The particle concentration must be small enough (typically $10^9\text{-}10^{12}$ particles/m³) so as not to alter the physical properties of the studied fluid. For best results, the particles should be uniformly distributed in the flow, although this criterion is not as critical as for laser Doppler Velocimetry [30]. Since PIV actually measures the velocity of the tracing particles in the flow it is critical to ensure that they follow faithfully the important structures of the flow. This usually means that the particles injected in the flow must be small. However the particles must have good light scattering properties to be tracked by the imaging system. Because of these two opposing criteria for the size of the particles, an optimum particle size must be found. At first order approximation and with the small Reynolds number assumption, the difference between a particle velocity, \vec{V}_p , and the surrounding fluid velocity, \vec{U} , can be written as [37]

$$\vec{V}_p - \vec{U} = \frac{2}{9} \frac{r_p^2(r_p - r)}{\mu} \frac{d\vec{V}_p}{dt} \quad (17)$$

where r_p and r_p are the radius and density of the particle, and r and μ are density and viscosity of the fluid. From this expression we observe that the velocity difference is small when the term $r_p^2(r_p - r)/\mu$ is small. For hot gas flows (i.e. present study), solid particles are usually used because liquid droplets tend to evaporate. As a result, in this application the density of the gas is negligible compared to that of the particle (by three orders of magnitude). We then define the particle response time, t_p , to a stepwise change in the flow velocity

$$t_p = \frac{2}{9} \frac{r_p^2 r_p}{m}. \quad (18)$$

For a given turbulent flow time scale, the particle follows the flow faithfully within 2% error when the Stokes number (ratio of the particle time scale to the flow time scale) is smaller than 0.2 [31]. The characteristic time scales in a turbulent flow are bounded by the Kolmogorov and integral time scale ([32],[33]). Invoking the energy cascade, and the equilibrium between turbulent kinetic energy production at the integral scales and dissipation at the Kolmogorov scales, one can establish the following scaling law for the Kolmogorov time scale, t_K

$$t_K \propto t_0 \text{Re}_0^{-\frac{1}{2}} = t_0 (U_0 L_0 / n)^{-\frac{1}{2}} \quad (19)$$

Where t_0 is the integral time scale (i.e L_0/U_0), and Re_0 is the Reynolds number at the large scales. This simple relation provides an estimation of the time scales in the flow, as reported in Table 1 for a flow with 15% RMS of a mean velocity of 22 m/s. In addition, the resulting Stokes number range for titanium-dioxide (TiO_2) particles of mean diameter ranging from 0.3 to 1.0 μm is also presented. For a particle 0.3 μm in diameter this

Table 1. Response time of TiO_2 tracing particle in a turbulent flow characteristic of current experimental conditions ($\text{Re}_0 = 5345$, $U_0 = 3.3$ m/s, $L_0 = 4$ mm)

Particle mean diameter d_p , μm	Particle response time t_p , s	Flow time scales t_f , s	Stokes number $St = t_p / t_f$
0.3	$1.12 \cdot 10^{-6}$	Kolmogorov $42 \cdot 10^{-6}$	0.027
		<i>Limit 2% error</i> $5.8 \cdot 10^{-6}$	0.2
		Integral $1.21 \cdot 10^{-3}$	0.001
1.0	$12.5 \cdot 10^{-6}$	Kolmogorov $42 \cdot 10^{-6}$	0.305
		<i>Limit 2% error</i> $64.1 \cdot 10^{-6}$	0.2
		Integral $1.21 \cdot 10^{-3}$	0.011

analysis shows that the Stokes number is less than 0.027. Thus, the particle follows all the flow structures. A larger particle 1 μm in diameter is almost able to follow faithfully all the scales of motion down to 2/3 of the Kolmogorov scales. This scaling analysis provides confidence that the selected particles of TiO_2 with mean diameter in the range 0.3–1.0 μm faithfully follow most of the important turbulent structures present in the flow. Although the particles follow almost all the scales of motion, the PIV is not able to spatially resolve the Kolmogorov scales because the integration region (control volume) ideally contains several particles.

The TiO_2 solid particles are injected in the film-cooling flow and the hot mainstream using two similar seeders. These fluidized bed solid particles seeders were made to match the seeding requirements by utilizing compressed air forced through a porous plate, as pictured in Figure 4. The large pressure drop across this plate creates high-speed micro-jets that entrain solid particles. When the inlet pressure and flow rate are correctly set the powder bed is fluidized and homogeneous [34]. The seeding density can be controlled by modifying the pressure and flow rate through the seeder. Additionally, the position of the exit tube in the seeder can be lowered or raised to increase or decrease, respectively, the seeding density.

b) Particle illumination and imaging

This study makes use of a commercial PIV system purchased from LaVision Inc

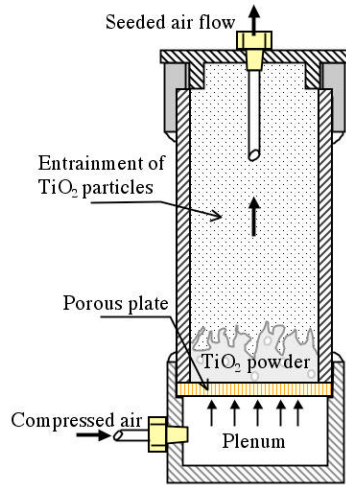


Figure 4. Schematic of the fluidized bed solid particle seeder.

[35]. The system includes a Solo PIV laser from New Wave Research, with a dual Nd:YAG laser-head. It incorporates a beam combining system and frequency doubler providing high output energy of green visible light (up to 100 mJ per pulse at 532 nm wavelength). Focusing and sheet forming optics are attached to the exit of the laser to produce a bright illumination plane of the seeded flow. The pulse timing and laser power can be directly controlled from the PIV computer in the Davis Software.

Each laser pulse needs to be very short to prevent the imaging system from seeing streaks of particles instead of instant snapshots of the frozen flow. Because this laser system has a pulse duration between 5 and 15 ns virtually any flow speed can be frozen. This is particularly true in the current work with speeds on the order of 30 m/s and low magnification factor in the imaging system.

The minimum time interval between frames, dt , is not limited by the laser pulse duration but by the CCD sensor in the digital camera. In double frame capture mode required for PIV), the first frame needs to output to the camera RAM before the second frame is acquired by the CCD sensor. The camera used in the present work, Camera Imager Pro X, is a 14-bit CCD camera with 4 Mega pixels spatial resolution. In double exposure mode it has an interframe time of 100 ns that is small enough for velocity measurements in high-speed flows. The optical system configuration was setup so as to allow the particle image to be larger than one pixel, thus avoiding peak locking. Peak locking occurs when a particle image smaller than one pixel is displaced by a small distance during the interframe time but remains in the same pixel. The PIV algorithm cannot capture this displacement and returns a zero velocity, thereby influencing the quality of the flow statistics. Furthermore, particle images smaller than one pixel are not

desired because sub-pixel interpolation for the displacement is not possible, thus limiting the dynamic range of the PIV measurement. To ensure a proper optical configuration for PIV one has to adjust the field of view and the aperture $f^\#$ of the camera lens. The particle image diameter, d_{im} , can be calculated using the relation [37]

$$d_{im} = \left((2.44(1 + M_0)f^\#)l)^2 + M_0^2 d_p^2 \right)^{1/2} \quad (20)$$

where M_0 is the magnification factor (image size divided by the object size), l is frequency of the laser light (i.e. 532 nm), and d_p is the particle physical diameter. The first term in the square root is the diffraction-limited spot and the second term is the geometric size in the image plane. In the present study the field of view is 50 by 50 mm and the CCD sensor is a square of side 15.155 mm. Consequently the magnification factor is less than unity and equal to 0.3031. Given an $f^\#$ of 8, the particle image diameter is reported in Table 2 for particle sizes of 0.3 and 1.0 μm . The particle image diameter is also expressed in pixels, given the pixel size is 7.40 μm for the CCD chip. This estimation demonstrates that the particle image is larger than one pixel independently of the size of the particle, which reveals that the diffraction limited spot dominates the geometric image of the particle. More importantly, d_{im} is very close to 2 pixels, which represents the optimum size to reduce RMS displacement errors [36].

The present analysis is only valid if the illuminated particles are in focus. This means that the laser sheet thickness must be smaller than the camera depth of field (or

Table 2. Particle image for particle diameters of 0.3 and 1.0 μm , $f^\# = 8$

Particle diameter, d_p (μm)	0.30	1.00
Particle image diameter, d_{im} (μm)	13.53	13.54
Particle image diameter, d_{im} (pixel)	1.83	1.83

depth of view). Illumination planes with a thickness, dz_0 , of 1 mm were easily achieved. The camera depth of view is calculated based on optical considerations using [37]

$$dz_0 = 4(1 + M_0^{-1})^2 f^{\#2} l . \quad (21)$$

With the magnification factor, aperture number and laser frequency retained above, the depth of view is equal to 2.52 mm, which is greater than the laser sheet thickness. Consequently this validates the imaging settings used in the present study, and the particle size choice. However, there are other challenges one needs to be aware of when using PIV for a wall-bounded flow.

c) Challenges associated with the PIV technique

There exist several technical challenges associated with obtaining a high quality image pair of the seeded flow and thus guaranteeing a good measurement using the PIV technique. Such challenges are: identifying the focal plane, determining the seeding concentration and interframe time, and reducing the noise at the wall. First, one needs to ensure that the camera is correctly focused in the plane of illumination. This can be verified empirically by inspecting the images of particles or more deterministically by identifying the focal plane that produces the maximum image contrast defined by the standard deviation of the image grey value divided by the mean image grey value.

In addition, the seeding concentration and interframe time need to be adjusted using an iterative procedure described by Westerweel [36]. One starts with low seeding concentration and a small interframe time so that successive frames are almost identical. The seeding concentration is slowly increased while monitoring the signal to noise ratio of the cross-correlation function, until this ratio is above 3 in the measurement domain. Once the optimum seeding concentration is found, the interframe time can be increased to

obtain the maximum dynamic measurement range. Proceeding by increments, dt is increased while monitoring the results of the cross-correlation. The maximum resulting particle displacement in the flow should be between 5 and 10 pixels. This criterion is recommended for our system, and sets the upper bound of the dynamic range. The lower bound is function of the post-processing technique and the quality of the image pair. According to the specifications of Davis software, sub-pixel resolution (0.01 pixel) is achieved.

For wall-bounded flows, high laser power often creates difficulties due to light scattering at the wall, which creates a halo that illuminates particles out of the measurement plane near the wall. If this wall illumination effect exceeds the depth of view of the camera some particles are seen out of focus. Consequently the processing algorithm encounters difficulties in obtaining a correlation in this critical near-wall region. Correctly adjusting the aperture of the camera reduces this wall effect but also resets the imaging settings. In the present study a different approach to reduce the wall scatter was preferred. This technique consists in applying a coat of clear paint with rhodamine 6-G on the wall surface and by using a 532 nm bandpass filter in front of the camera optics. The dye of the paint layer absorbs the incident 532-nm light and re-emits in the range 555-585 nm with a peak at 566 nm. Consequently laser scatter effects at the wall are strongly attenuated for a camera equipped with the 532nm bandpass filter. This wall treatment technique has been applied with success in the present study to enhance near wall resolution.

d) Obtaining the vector field

In this section, we present briefly the main steps leading to the final velocity field

results, which were performed using LaVision Flow Master software [35]. Before conducting the hot flow experiments, a calibration plate is inserted in the test section to calibrate the distances in the imaging system. Then the experiment is started, keeping the illumination and imaging systems settings constant. To obtain reasonable statistics 1000 pair of images are recorded at each of the four streamwise stations.

The raw images are first pre-processed, then the vectors are computed, and finally the results are post-processed. In the pre-processing step, a sliding background is applied in order to remove the contribution of particles stuck in the window. The vectors are then computed using a multi-pass cross-correlation algorithm. The interrogation region is first 32 by 32 pixels then it is reduced to 8 by 8 pixels in the last pass. A 50% overlap of the interrogation regions is applied as suggested by the manufacturer. The post-process includes a procedure to remove and replace spurious vectors using the median filter technique developed by Nogueira et al. [38]. Statistics are then computed on the 1000 samples to obtain mean and RMS of the streamwise and wall normal velocity components.

Wall temperature and heat transfer

The temperature of the backside of the test wall was measured using four type K surface-mounted thermocouples. Due to the high mass flow of water-cooling on the backside, this wall surface has a nearly uniform temperature. The temperature is interpolated using these four data points.

The temperature of the surface of the wall facing the film flow was measured by infrared (IR) thermography. This non-intrusive measurement technique makes use of an IR thermal sensor in the FLIR ThermaCam SC 3000. This sensor receives thermal

radiation from the measurement surface with optimum IR range in the 8-9 μm wavelength spectrum. Consequently the casing of the test section was equipped with an optical access made of calcium-fluoride (CaF_2), which has good transmission in the IR range up to a 10- μm wavelength. Several optical parameters influence the temperature measurement using this technique. They are the emissivity of the wall, the temperature and emissivity of the CaF_2 window, and the optical and thermal properties of the atmosphere. These parameters change with the operating temperature for a given experiment. Consequently, the IR measurements were first calibrated at the operating conditions using a micro-thermocouple probe inserted at the wall.

Given the measurement of the temperature difference across the test wall and knowing the thermal properties of the UDEL material, one can easily determine the conduction heat flux across the wall, as illustrated in Figure 5. Using a sign convention with positive heat flux being oriented from the film flow towards the wall, the conductive heat flux across the wall, q_k , is obtained by

$$q_k = \frac{k_w}{t_w} (T_w - T_{wb}), \quad (22)$$

where the wall thermal conductivity $k_w = 0.25 \text{ Wm}^{-1}\text{K}^{-1}$ and the wall thickness $t_w = 6.35 \text{ mm}$. The wall temperatures on the film side and on the backside are T_w and T_{wb} respectively, as represented in Figure 5. In this equation, it was assumed that the heat conduction within the wall is one-dimensional with a preferred direction in the wall normal direction. This assumption is valid because of the large gradients across the wall and the relative thinness of the wall.

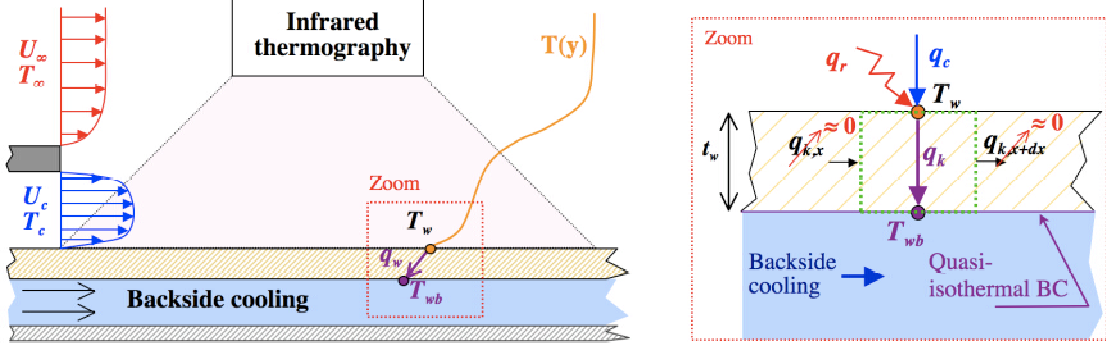


Figure 5. Wall temperature and heat flux measurements

The convective heat flux at the wall per unit area, q_c , is then estimated by writing a heat balance at the surface of the wall between convection, radiation from the casing and conduction across the solid. Using the same sign convention described above,

$$q_c = q_k - q_r \quad (23)$$

where q_r , the net radiation heat flux per unit area. At each wall temperature measurement point, the net radiation flux per unit area on the wall from the casing is calculated using the direct radiation approach and neglecting multi-reflections [39]

$$q_r = e_0 e_w F_{w0} \sigma (T_0^4 - T_w^4) \quad (24)$$

where T_w and T_0 are the temperatures of the wall element and the casing, e_w and e_0 are the emissivity of the wall and the casing, σ is the Stefan-Boltzmann constant, and F_{w0} is the view factor from the wall to the casing. This later parameter was calculated by using view factor algebra and removing the view factor from the wall to the window, $F_{w,win}$, because the window is transparent to infrared radiation. Consequently F_{w0} is obtained by:

$$F_{w0} = 1 - F_{w,win} \quad (25)$$

where $F_{w,win}$ is calculated based on the analytical form proposed by Siegel and Howell [40]. In the calculation of the radiation heat flux, the emissivity of the casing made of polished stainless steel is equal to 0.20 and that of the test plate made of UDEL is equal to 0.91.

The radiation effects may seem small compared to the conduction heat flux but near the slot exit the wall is much cooler than the casing. This results in thermal radiation loads that cannot be neglected compared to the small heat conduction across the wall in this region. Further downstream, as the wall temperature increases, the radiative heat flux becomes smaller compared to the conductive heat flux.

Flow temperature

The flow temperature is measured with a micro-thermocouple inserted in the flow through small portholes in the casing of the test section that are located at the edge of the IR transparent window. The probe itself, as illustrated in Figure 6, is made of a 13 μm -wire-diameter type K thermocouple threaded through a double holed ceramic insulator. The properties of this electrical insulation guarantees operation up to elevated temperatures. The ceramic assembly is then inserted in a stainless steel tube and bonded

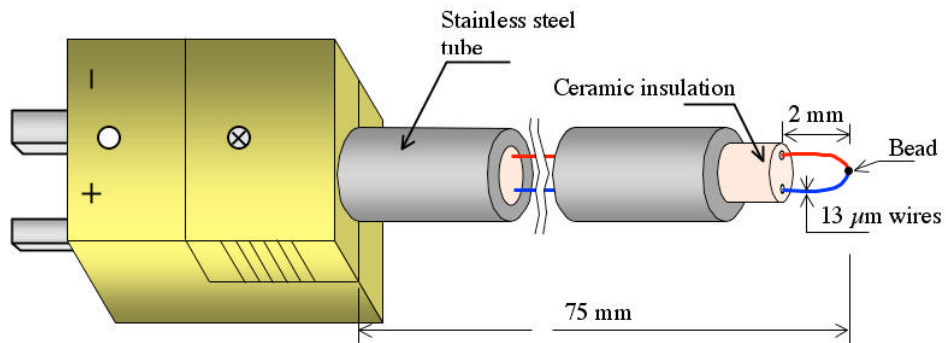


Figure 6. Micro-thermocouple probe assembly, 13 μm wire diameter type K.

at its extremities with high temperature cement. The probe is equipped with a mini-connector jack that is connected to a probe holder on a 10 μm -precision traverse. This assembly allows measurement of temperature profiles at accurate wall-normal location. The bead of the thermocouple extends 2 mm outside the ceramic and the stainless tube to avoid flow disturbances at the measurement location. Given Shaddix's recommendations [41], this distance is also sufficiently long for the axial thermal conduction to be negligible in the vicinity of the bead, even under the largest flow temperature gradients measured in the experiments. The data were recorded and digitized at a 20 kHz sampling frequency using a Labview data acquisition board.

Due to the small size of the thermocouple probe, the convection-dominated dynamics at the beads result in radiation and conduction losses being negligible. However even for a small thermocouple bead of 13 μm diameter, large fluctuations of temperature due to turbulent structures are attenuated at high frequencies due to the thermal inertia of the probe. This transient response of the probe can be analyzed by performing a heat balance on the bead where conduction and radiation are neglected. Noting T_g the actual gas temperature, T_b the bead temperature (i.e. temperature measured by the probe), and m_b , $C_{p,b}$ and A_b , the mass, specific heat and area of the bead respectively, the heat balance can be written as

$$m_b C_{p,b} \frac{dT_b}{dt} = h_{\text{conv}} A_b (T_g - T_b) \quad (26)$$

where h_{conv} is the convective heat transfer coefficient associated with the flow around the bead. The time constant of the transient heat balance, t_b , is defined by

$$t_b = \frac{m_b C_{p,b}}{h_{conv} A_b} \quad (27)$$

The time constant is a function of the bead physical properties and geometry, but also depends on the thermal and kinematic properties of the flow surrounding the bead, as evidenced by the dependence on the convective heat transfer coefficient. Introducing the time constant in the heat balance equation and solving for the actual gas temperature yields

$$T_g = T_b + t_b \frac{dT_b}{dt} . \quad (28)$$

The value of the time constant was estimated by measuring, in the test section, the transient response of the probe to an electrical heating-cooling cycle as described by Marshall [42]. The result of this analysis over a significant number of cycles shows t_b takes values between 1.5 to 2.3 ms depending on the relative position of the thermocouple to the wall and the operating conditions in the test section. Knowing the value of this parameter allows us to solve for the actual gas temperature, T_g , as a function of the measured temperature, noted T_b in this analysis. A digital compensation technique based on a spectral analysis of the raw signal allows one to correct for the thermal inertia of the probe and thus to recover the power of the temperature fluctuations at high frequencies. This procedure is reported by Cruz and Marshall [12], and for convenience for the reader in Appendix A1.

Statistical quantities of the compensated signal are computed to yield characteristics of the thermal mixing in the flow. Mean temperature and root-mean-square (RMS) are computed. Higher order statistical moments, such as the skewness and

flatness, are also computed to help analyze the probability density function (PDF).

2.1.3 Test matrix

Three different experimental velocity ratios ($VR = U_c/U_\infty$) were considered in this study: a wall-wake flow ($VR < 1.0$), a boundary layer type flow ($VR=1.0$) and a wall jet ($VR=2.0$). For each case two different wall thermal boundary conditions were examined: an adiabatic wall and a wall with nearly uniform temperature distribution on the backside. Actual experimental conditions are reported in Table 3. To facilitate the reference to key parameters of each experiment, the name of the test comprises a numeral referring to the velocity ratio (e.g. 0.5) and optional letters ‘AD’ referring to the adiabatic wall condition, if applicable. The velocity ratio, VR , and the blowing ratio, m , are parameters that describe the relative velocity and mass flux between the coolant stream and the mainstream. High velocity ratios are commonly encountered in gas turbine engine combustors [1] and low velocity ratios are mostly found in rocket thrust chambers and nozzles. Consequently, this study is relevant to film cooling applications for both rocket and gas turbine engines. Of particular interest to this study is the characterization, both experimental and numerical, of the near-wall turbulence that governs the film mixing in these flow regimes.

Adiabatic and non-adiabatic walls are considered in this study. The adiabatic wall experiments (VR0.5AD, VR1.0AD and VR2.0AD) allow direct measurement of the adiabatic wall temperature and the corresponding film cooling effectiveness. This latter parameter describes the effects of the thermal mixing of the film as mentioned earlier. Combining adiabatic and non-adiabatic experiments with identical inflow conditions

Table 3. Experimental operating conditions

Tests →	VR0.5AD	VR0.5	VR1.0AD	VR1.0	VR2.0AD	VR2.0
Wall →	Adiabatic	Backside cooled	Adiabatic	Backside cooled	Adiabatic	Backside cooled
U_c (m/s)	10.82	10.82	19.13	19.13	21.20	21.20
U_∞ (m/s)	24.86	24.86	22.10	22.10	11.10	11.10
$VR = U_c/U_\infty$	0.44	0.44	0.87	0.87	1.93	1.93
T_c (K)	304.78	306.11	298.88	304.43	296.33	301.54
T_∞ (K)	462.02	454.94	454.33	446.33	462.92	437.89
$TR = T_\infty/T_c$	1.52	1.49	1.52	1.47	1.56	1.45
Re_s	2652	2631	4857	4698	5466	5297
$m = VR TR$	0.66	0.65	1.32	1.27	3.01	2.80

yields the convective heat transfer coefficient for film cooling flows, as defined by Lefebvre [1].

2.1.4 Typical experimental uncertainties

In this section a discussion of experimental uncertainties is presented. Measurement errors can be divided into two major categories: random errors and systematic errors. The later is manifested when a physical phenomenon consistently alter the measure of a quantity (e.g. thermal radiation on a surface temperature). This type of error is usually avoided by applying a careful calibration of the instrument at a reference measurement point. Random errors however, cannot be avoided because of the very nature of the instrument that measures a physical quantity that sometimes has a random component. This leads to the measurement uncertainty, a parameter that quantifies the statistical distribution of the measured value. For a quantity, Q , expressed as a function

of directly measured quantities, w_i ,

$$Q = Q(w_1, w_2, \dots, w_n) \quad (29)$$

the overall uncertainty DQ is expressed as a function the measurement uncertainties, Dw_i , by [43]:

$$\Delta Q = \sqrt{\left(\frac{\partial Q}{\partial w_1} \Delta w_1\right)^2 + \left(\frac{\partial Q}{\partial w_2} \Delta w_2\right)^2 + \dots + \left(\frac{\partial Q}{\partial w_n} \Delta w_n\right)^2} \quad (30)$$

For brevity, the derivation of the expression for the uncertainty of the measured and derived quantities is reported in Appendix A2. Characteristic values and uncertainties of most important measured and derived quantities are reported in Table 4. Uncertainty in flow temperatures are small +/- 0.25 K, and are nearly independent of the temperature. The uncertainty of PIV measurements is difficult to evaluate. Based on the particle response time analysis, a 1% error has been selected here. The wall and casing temperatures have a higher uncertainty of +/- 0.5 K because of possible radiation effects. Based on these parameters, uncertainties in derived quantities are calculated. These uncertainties are very small for the blowing ratio, the slot Reynolds number and the film effectiveness. The uncertainty in the conductive heat flux depends on the temperature difference across the wall and is between 2 and 4 % under characteristics experimental conditions. The uncertainty in radiation heat flux is larger (13%) and nearly uniform. It is dominated by the uncertainty in the casing emissivity. Finally the uncertainty in the convective heat transfer coefficient is the largest particularly near the slot exit where there the difference between the adiabatic wall temperature and the wall temperature is small.

Table 4. Uncertainty in Measured and Derived Quantities

Characteristic measured quantities				
w_b , units	Value	Δw_i	$\Delta w_i / w_b \%$	Notes
T_c , K	300	± 0.25	± 0.08	Coolant temperature
T_∞ , K	450	± 0.25	± 0.06	Mainstream temperature
U_c , m/s	21.2	± 0.21	± 1.00	Coolant bulk velocity
U_∞ , m/s	11.1	± 0.11	± 1.00	Mainstream velocity
s , m	0.004	$\pm 50 \cdot 10^{-6}$	± 1.25	Slot height
T_{aw} , T_w , K	300 – 350	± 0.5	$\pm(0.14 - 0.16)$	Wall temperature
T_θ , K	400	± 0.5	± 0.12	Casing temperature
Derived quantities				
Q , units	Value	ΔQ	$\Delta Q / Q, \%$	Notes
m			± 1.42	
Re_s			± 1.61	
h	0.75 – 1.0		$\pm(0.37 - 0.76)$	
q_{cond} , W/m ²			$\pm(2.12 - 4.06)$	($T_w - T_{wb}$) from 50K to 10 K
q_{rad} , W/m ²			± 13.52	Nearly constant
q_{conv} , W/m ²			$\pm(4.30 - 5.20)$	
T^*_{aw} , K	300 – 350	± 0.64	$\pm(0.18 - 0.20)$	
h , W/(m·K)			$\pm(5.6 - 34)$	($T^*_{aw} - T_w$) from 20K to 2 K

2.2 Navier-Stokes Solver

With the increase in computing power, large-eddy simulations (LES) of turbulent flows have shown promising perspectives in the endeavor of understanding the physics of turbulent flows for which direct numerical simulations (DNS) would be practically unfeasible. The LES solver used in the present work is a derivation of an existing solver LES3D-MP developed by Anthony Keating ([25], [26]). The transport equation for a passive scalar (temperature), the LES eddy-diffusivity model, and the corresponding boundary conditions have been implemented. The existing RANS Spalart-Allmaras model was extended with a turbulent Prandtl number approach to model the eddy-diffusivity in RANS mode. The objective of the present section is to present the modeling approach for both LES and RANS modes.

2.2.1 Fundamental framework: RANS and LES

Large-eddy simulation is gradually gaining more interest from the engineering community in research and development initiatives. For the past decades Reynolds averaged Navier-Stokes (RANS) solvers have been the standard tool to simulate industrial turbulent flows. However due to the complexity and specificity of RANS turbulence modeling, the LES approach has emerged as a more universal and comprehensive tool for solving turbulent flow problems.

In contrast to RANS, where only time averaged quantities are calculated, LES distinguishes between grid resolved (large) and modeled subgrid (small) scales of turbulent motion. Consequently the problem and geometry dependent large scales are directly resolved while the more universal small scales are modeled. The modeling in LES consists mainly in expressing the contribution of the small scales to the large scales.

Most models calculate this contribution based on the energy contained in the large scales.

2.2.2 Governing equations

For the purpose of simulating the experimental conditions in the hot wind tunnel the incompressible flow assumption is assumed valid because of the low Mach number conditions in this facility. Consequently we consider the incompressible Navier-Stokes equations and the energy conservation equation for a non-reacting flow. These equations are non-dimensionalized using a reference length, velocity, and temperature, noted respectively L_R , U_R , and T_R . In addition, the Cartesian grid and velocity field are defined in tensor notation by

$$(x_i)_{i=1..3} = (x, y, z) \text{ and } (u_i)_{i=1..3} = (u, v, w)$$

Making use of Einstein tensor summation convention, the dimensionless governing equations are

$$\frac{\partial u_i}{\partial x_i} = 0 \quad (31)$$

$$\frac{\partial u_i}{\partial t} + \frac{\partial u_j u_i}{\partial x_j} = \frac{1}{Re} \frac{\partial^2 u_i}{\partial x_j \partial x_j} - \frac{\partial p}{\partial x_i}, \quad i = 1..3 \quad (32)$$

$$\frac{\partial T}{\partial t} + \frac{\partial T u_j}{\partial x_j} = \frac{1}{Re \cdot Pr} \frac{\partial^2 T}{\partial x_j \partial x_j} \quad (33)$$

where the Reynolds number and Prandtl number are defined by

$$Re = \frac{U_R L_R}{n(T_R)} \quad Pr = \frac{n}{a} = \frac{n r C_p}{k} .$$

In this formulation of the Navier-Stokes equations, the temperature is assumed to be a passive scalar, and the fluid properties are constant. The LES governing equations

are obtained by filtering the Navier-Stokes equations with a filter operator. In the LES approach only the filtered variables are solved directly while the subgrid part is modeled with a physical model. Given a filter operator G , the filtering operation of a variable $f(x)$ is noted by an overbar and defined by

$$\bar{f}(x) = \int f(x') G(x, x'; \bar{\Delta}) dx' \quad (34)$$

where $\bar{\Delta}$ is the characteristics length of the operator G . Because the present solver uses finite difference methods it is recommended to apply the top-hat filter, defined in physical space by

$$G(x) = \begin{cases} 1/\bar{\Delta} & \text{if } |x| \leq \bar{\Delta}/2 \\ 0 & \text{otherwise} \end{cases} \quad (35)$$

Consequently applying the top hat filter to the incompressible Navier-Stokes equations and the energy conservation equation (Eq. (1,2,3)) leads to the governing equations of the present LES solver

$$\frac{\partial \bar{u}_i}{\partial x_i} = 0 \quad (36)$$

$$\frac{\partial \bar{u}_i}{\partial t} + \frac{\partial \bar{u}_j \bar{u}_i}{\partial x_j} = \frac{1}{Re} \frac{\partial^2 \bar{u}_i}{\partial x_j \partial x_j} - \frac{\partial \bar{p}}{\partial x_i} - \frac{\partial \bar{t}_{ij}}{\partial x_j}, \quad i = 1..3 \quad (37)$$

$$\frac{\partial \bar{T}}{\partial t} + \frac{\partial \bar{T} \bar{u}_j}{\partial x_j} = \frac{1}{Re \cdot Pr} \frac{\partial^2 \bar{T}}{\partial x_j \partial x_j} - \frac{\partial q_j}{\partial x_j} \quad (38)$$

The subgrid-scale (SGS) stress tensor, \bar{t}_{ij} , and the subgrid-scale heat flux term, q_j , are the unresolved terms that contain the contribution of the small scales and need to be modeled. Given the filtering operation, these terms are mathematically defined by

$$t_{ij} = \overline{u_i u_j} - \bar{u}_i \bar{u}_j \quad (39)$$

$$q_j = \overline{T u_j} - \bar{T} \bar{u}_j \quad (40)$$

In the present study, the RANS solver uses the same governing equations as the LES version. A first major difference is that the filtered variables are actually Reynolds averaged. A second major difference lies in the expression of the model closure terms t_{ij} and q_j . To avoid confusion we refer to these terms as closure terms for RANS and subgrid scale (SGS) terms for LES.

2.2.3 Sub-grid scale and RANS closure terms

There exist several classes of SGS or closure models in the CFD literature. Among those most widely used is the family of gradient-based models: the eddy-viscosity model and eddy-diffusivity model. Spalart-Allmaras and Smagorinsky models both calculate the eddy-viscosity, η_t . For LES the dynamic eddy-viscosity model removes the need for an empirical *a priori* determination of the model parameter of the Smagorinsky model by dynamically calculating the model parameter as a function of time and spatial location. By analogy, eddy-diffusivity models are also used to model the SGS or closure term q_j .

Eddy-viscosity model

The eddy-viscosity modeling approach consists of expressing the subgrid-scale stresses, t_{ij} , as a function of the resolved strain rate tensor \bar{S}_{ij} and a subgrid-scale eddy-viscosity, η_t^{sgs}

$$t_{ij} - \frac{d_{ij}}{3} t_{kk} = -2 \eta_t^{sgs} \bar{S}_{ij} . \quad (41)$$

In this equation δ_{ij} is the Kroenecker symbol and the strain rate tensor is defined by

$$\bar{S}_{ij} = \frac{1}{2} \left(\frac{\partial \bar{u}_i}{\partial x_j} + \frac{\partial \bar{u}_j}{\partial x_i} \right)$$

One of the most commonly used eddy-viscosity subgrid-scale model is the Smagorinsky model [44], which can be expressed as

$$\eta_t^{sgs} = C_{ev} \bar{\Delta}^2 (2 \bar{S}_{ij} \bar{S}_{ij})^{1/2} = C_{ev} \bar{\Delta}^2 |\bar{S}| \quad (42)$$

In this model, the eddy-viscosity is the product of a model coefficient, C_{ev} , a length scale (the filter width $\bar{\Delta}$) and a velocity difference at that scale ($\bar{\Delta} |\bar{S}|$). The value of the coefficient C_{ev} depends on the position of the cutoff filter width in the spectral domain. C_{ev} has been reported for a variety of tests to be in the range 0.01 to 0.1 [45], with 0.032 being quoted for isotropic turbulence [46]. In the presence of shear and near wall boundaries the value of this coefficient needs to be lowered, hence complicating the *a priori* choice of the constant. Van Driest damping functions are widely used near a wall boundary. Eddy-viscosity models usually represent accurately the global dissipation at the small scales, but they do not calculate the local stresses well. Several other physical drawbacks have been associated with this type of model: the eddy viscosity does not vanish for laminar flows, backscatter of energy is not realizable because the eddy viscosity is always positive, and as a consequence too much diffusion is usually introduced into the flow [45].

For the RANS Spalart-Allmaras model, the eddy-viscosity is calculated based on a modified eddy-viscosity for which a transport equation is solved. Details about the Spalart-Allmaras model can be found in [47] and in Appendix A3.

Eddy-diffusivity model

Similarly, an eddy-diffusivity model calculates the subgrid-scale heat flux using a subgrid-scale eddy-diffusivity coefficient and the resolved temperature gradient [48]

$$q_j = -\alpha_t^{sgs} \frac{\partial \bar{T}}{\partial x_j}. \quad (43)$$

In this equation the subgrid-scale eddy-diffusivity, α_t^{sgs} , is calculated using an expression similar to the one for the subgrid-scale eddy-viscosity, with a different coefficient C_q

$$\alpha_t^{sgs} = C_q \bar{\Delta}^2 (2 \bar{S}_{ij} \bar{S}_{ij})^{1/2} = C_q \bar{\Delta}^2 |\bar{S}| \quad (44)$$

Published results from *a priori* tests indicate that the value of the ratio C_{ev}/C_q is in the range 0.4 to 0.6, with 0.5 being the optimal value for a mean scalar gradient in the wall normal direction [48].

For the RANS calculations the eddy-diffusivity is directly related to the eddy-viscosity via a turbulent Prandtl number, Pr_t , defined by

$$\text{Pr}_t = \frac{n_t}{\alpha_t} \quad (45)$$

Based on previous studies of heat transfer in wall bounded turbulent flows and recommendations by Kay and Crawford [49] the turbulent Prandtl number was kept constant and equal to 0.85.

Dynamic procedures for LES

As mentioned earlier, the determination of the model coefficients for gradient-based SGS models in LES is somehow empirical. Germano, Piomelli, Moin and Cabot [50] developed a procedure that dynamically calculates the SGS coefficients C_{ev} and C_q

based on the energy content of the smallest resolved scales, thus removing the *a priori* aspect of prescribing their value.

Rewriting the definition of the resolved stresses as a function of the total stresses and the subgrid-scales stresses, t_{ij} , one obtains

$$\bar{u}_i \bar{u}_j = \overline{\bar{u}_i \bar{u}_j} - t_{ij} \quad (46)$$

Defining a test filter, noted by the $\hat{\cdot}$ symbol, of width $\hat{\Delta}$ larger than the LES grid filter, and applying it to the previous equation yields the Germano identity

$$\underbrace{\hat{\bar{u}}_i \hat{\bar{u}}_j - \hat{\bar{u}}_i \hat{\bar{u}}_j}_{=L_{ij}} = \underbrace{\hat{\bar{u}}_i \hat{\bar{u}}_j - \hat{\bar{u}}_i \hat{\bar{u}}_j}_{=T_{ij}} - f_{ij} \quad (47)$$

where the tensor L_{ij} , sometimes referred to as Leonard stresses [51], represents the part of the turbulent stresses that is resolved, T_{ij} represents the subtest stresses (at the test filter level). For the case of an eddy-viscosity model, the subgrid-scale and subtest stresses are respectively calculated with

$$t_{ij} = -2C_{ev} \bar{\Delta}^2 |\bar{S}| \bar{S}_{ij} \quad (48)$$

$$T_{ij} = -2C_{ev} \hat{\Delta}^2 |\hat{\bar{S}}| \hat{\bar{S}}_{ij}. \quad (49)$$

Replacing these terms into Germano's identity yields a system of five independent equations (because the tensors are symmetric) and one unknown coefficient C_{ev}

$$C_{ev} M_{ij} = L_{ij}, \quad (50)$$

where the tensor M_{ij} is defined by, $M_{ij} = -\hat{\Delta}^2 |\hat{\bar{S}}| \hat{\bar{S}}_{ij} + \bar{\Delta}^2 |\bar{S}| \bar{S}_{ij}$. Using Lilly's method [52], the coefficient C_{ev} is obtained from Eq. (50) by solving a least-square problem

which leads to

$$C_{ev} = -\frac{1}{2} \frac{\langle L_{ij} M_{ij} \rangle}{\langle L_{ij} L_{ij} \rangle}. \quad (51)$$

In this equation, the coefficients are averaged (noted $\langle \cdot \rangle$) to remove the very sharp fluctuations that may lead to numerical instabilities. For simple flow geometries with one or two directions that are statistically homogeneous, the average is performed over these homogenous directions. However for more complex flows, Meneveau et al. [53] suggest that it is preferable to perform the average over a flow pathline. This Lagrangian average is the averaging procedure used in the present code.

With this procedure the eddy-viscosity tends to zero near the wall without resorting to a damping function. In addition, the coefficient C_{ev} and consequently the eddy-viscosity, can take negative values. Thus this model can capture regions of the flow containing backscatter of energy.

By analogy, the eddy-diffusivity model coefficient, C_q , is calculated based on a similar formulation [48]

$$C_q = -\frac{\langle F_j N_j \rangle}{\langle N_j N_j \rangle} \quad (52)$$

$$F_j = \hat{\overline{T}} \hat{\overline{u}}_j - \hat{\overline{T}} \hat{\overline{u}}_j \quad (53)$$

$$N_j = \hat{\Delta}^2 |\hat{\bar{S}}| \overbrace{\frac{\partial \hat{\bar{T}}}{\partial x_j}}^{\hat{\bar{T}}} - \overbrace{\hat{\Delta}^2 |\bar{S}| \frac{\partial \hat{\bar{T}}}{\partial x_j}}^{\hat{\bar{T}}} \quad (54)$$

The coefficient C_q is averaged using the Lagrangian treatment and is limited to positive values.

In general terms, the dynamic SGS models are able to account for important physical phenomena without the need to prescribe model constants. However this refinement of the SGS models leads to an increase of the computational cost.

2.2.4 Discretization and numerical methods

When using numerical methods to solve a set of equations one needs to verify that the discretized equations are consistent with the original set. In addition, it appears critical from a physical point of view that the discretized equations preserve certain key properties of the original equations, such as Galilean invariance, geometrical invariance (rotation, reflection) [46], mass, momentum, kinetic energy and pressure conservation [54].

LES3D-MP is an incompressible large-eddy simulation solver that is 2nd order accurate in space and 3rd order accurate in time. Variables are discretized on a staggered grid, as pictured in Figure 7. Velocity components are calculated at the face centers of the control volume while pressure and temperature are calculated at the center of the control volume. When using central differencing, the staggered grid arrangement has the advantage of preserving the conservation properties (i.e. momentum, kinetic energy, pressure-gradient conservation) of the momentum equation in their discretized form.

In the momentum equations, the viscous terms and the LES viscous cross derivative terms are discretized using second-order central differencing. The convective terms are discretized with a second-order conservative central difference scheme [55]. Optionally, the convective terms can also be calculated with the quadratic upstream interpolation for convection kinetics (QUICK) scheme of Leonard [56]. Similar discretization methods are used for the energy transport equation. The major difference

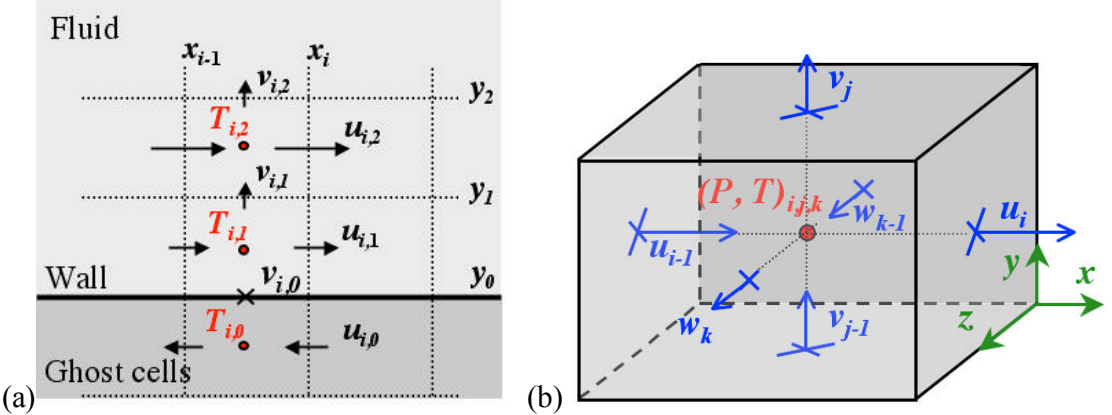


Figure 7. Discretization on a staggered grid with wall ghost cells

is that the temperature (stored at the cell center) needs to be interpolated to the centers of the faces of the control volume in order to calculate the convective terms. A linear interpolation or a QUICK scheme can be used for this matter. In the present work, the QUICK scheme of Leonard [56] was selected.

The treatment of the boundary conditions involves one or two ghost points depending on the convective scheme. However for solid wall boundaries a one-dimensional approximation is used, thus reducing to a unique ghost cell, as pictured in Figure 7-a. The values in the ghost cells are set to impose the correct streamwise and spanwise velocities, u and w , and temperature, T , at the wall by linear interpolation with the first fluid cell.

The discretized terms of the governing equations are advanced in time with a three-step low-storage third-order Runge-Kutta scheme [57]. However, in order to relax the time step limitation imposed by the stability constraints of this explicit scheme, the wall normal diffusion terms (in the momentum and energy equations) and the wall normal convection term in the energy equation are advanced implicitly using the Crank-Nicholson scheme.

2.2.5 Grid requirements for wall resolved LES

When dealing with wall bounded flows one is challenged, both experimentally and numerically, by the steep gradients of velocity and temperature at the wall. In particular, large eddy simulations necessitate an appropriate grid to resolve accurately the inner layer of a boundary layer. Chapman first derived the grid requirements for LES of wall-bounded flows [58]. In the outer region of a turbulent boundary layer, the characteristic length is the boundary layer thickness, d . To resolve a volume d^3 of this region of the flow, Chapman estimated that 2500 points are required. Thus for a developing boundary layer, for which d/x grows as a function of $Re^{0.2}$, resolving a volume $L_x \times d \times L_z$ will require a number of points that varies like $2500 Re^{0.4}$. In the particular case of a channel flow, the outer layer resolution does not depend on the Reynolds number since d is fixed.

For both internal and external boundary layer flows, resolving the inner layer is a much more computationally demanding process. In this region the most important eddies are the streamwise vortices which are characterized by a constant size in wall units. Quantities are normalized in wall units using the kinematic viscosity, η , and the friction velocity, u_t , defined by:

$$u_t = \sqrt{\tau_w / \rho} = \sqrt{\frac{\eta}{\rho} \frac{\partial \bar{u}}{\partial y}} \Big|_w \quad (55)$$

where τ_w is the wall shear stress and ρ is the density of the fluid. Piomelli reports that to resolve the inner layer, the streamwise and spanwise grid spacing in wall units should be $Dx^+ \approx 100$ and $Dz^+ \approx 20$ (with $x_i^+ = x_i u_t / \eta$) [51]. Additionally, to resolve the large gradients present in the viscous sublayer the first grid point away from the wall must

satisfy $Dy^+ < 1$. Consequently, assuming that the skin friction coefficient scales as $Re^{-0.2}$, it is found that the number of points required to resolve the viscous sublayer is proportional to $Re^{1.8}$ ([58], [51]).

When designing a grid for wall-resolved LES, the friction velocity can only be estimated *a priori* from simple scaling laws. Consequently, it is essential to verify the grid resolution *a posteriori* during the post-processing of the data. A grid sensitivity study is also recommended by analyzing the first moment statistics (mean quantities) in the flow to ensure a good grid resolution.

For the present flow configuration, the film injected through the slot is a turbulent channel flow and the mainstream flow is a turbulent boundary layer. Experiments indicate that the coolant flow is a fully developed turbulent channel flow, and also provide a measure of the boundary layer thickness for the mainstream. Based on fully developed turbulent channel flow theory, the velocity profile is approximated by the 1/7th power law [49]

$$u^+ = 8.6(y^+)^{1/7} \Leftrightarrow u/u_t = 8.6(y u_t / n)^{1/7}. \quad (56)$$

Integrating this profile from the wall to the half-slot height, $s/2$, yields the classical relation $U_{cm}/U_c = 8/7$, where U_{cm} is the centerline maximum velocity and U_c the bulk velocity. The derivation of this integral also yields:

$$U_c/u_t = \frac{2}{s} \int_0^{s/2} 8.6(y u_t / n)^{1/7} dy = 8.6 \frac{8}{7} \left(\frac{s u_t}{2 n} \right)^{1/7} \quad (57)$$

Then solving for the friction velocity as a function of the bulk velocity, one obtains

$$u_t = \left(\frac{8}{7} \frac{U_c}{8.6} \right)^{7/8} \left(\frac{n}{s/2} \right)^{1/8} = U_c \left(\frac{8}{60.2} \right)^{7/8} \left(\frac{2}{Re_s} \right)^{1/8} \quad (58)$$

From this expression the friction velocity depends only on the slot Reynolds number ($Re_s = U_c s / n$) and the bulk slot velocity. Since these parameters are obtained from measured quantities, this relation provides an easy estimate of the friction velocity used for the construction of the initial grid.

2.2.6 Inflow conditions

Ideally the flow field provided at the inlet plane should contain the temporal and spatial information of the turbulent flow structures and their contribution to the resolved scales in the simulation. For an inflow plane with normal in the x -direction this implies that the velocity vector is a function of y, z and time. Furthermore, the first and second order statistics of the velocity, the spectra and the phase information need to be specified. The later requirement is difficult to match with synthetic turbulence because the coherence of eddies, shape and structure interaction, depend on the type of flow. If the phase information is not provided correctly, the flow may undergo an adjustment, even relaminarization [60]. This is often experienced when using synthetic turbulence because it makes use of random distributions to construct turbulence with prescribed statistics.

A different category of inflow methods makes use of recycling information at the outflow to be injected back into the inflow plane. The simplest of these methods is the periodic boundary conditions, which prescribes the inflow to be equal to the outflow, and can only be used to study fully developed regions of simple flows (channel, pipe). A more elaborate method proposed by Spalart and Watmuff [61] uses a “fringe” region at the end of the computational domain. In this region, a source term is added to the

governing equations to decrease the boundary layer thickness, thus allowing periodic boundary conditions to be used for more complex flows. Another technique for boundary layers was proposed by Lund et al. [62] and makes use of rescaling arguments. The velocity at the inflow is taken several boundary-layer thicknesses downstream at the same wall-normal distance in wall units, y^+ . In the near-wall region, the mean velocity is recalled to match the law of the wall and the fluctuations to match the prescribed root-mean square (RMS). In the outer layer the rescaling is based on a law-of-the-wake. However the rescaling argument in both the fringe and rescaling method may not always be valid because there is no equilibrium region. More importantly these methods may lead to unwanted periodicity in the data.

Another family of methods makes use of precursor simulations to derive the inflow conditions. For one such method, a channel or boundary layer LES is performed with periodic boundary conditions. Slices of the flow are saved in a database every time step at a streamwise location where the friction coefficient and the boundary layer thickness are matched. This database can then be read and assigned at the inflow plane for the complex flow LES. Although this method is relatively simple and provides real turbulent structures at the inflow, it does have an extra computational cost associated with building the database of inflow slices. In the present study this method has been applied to produce the LES inlet planes of the mainstream and film flows.

2.3 Validation of the Solver

The objective of this section is to validate the RANS and LES models used in the study. The test case selected for the validation is that of a two-dimensional fully developed turbulent channel flow with constant heat flux at the wall. This simple flow geometry provides an ideal configuration for testing the performance of the models against DNS data by Kasagi et al. [63]. Of particular interest to this validation process is the wall resolution in terms of heat transfer coefficient and wall shear stress.

2.3.1 Fully developed turbulent channel flow background

The geometry of the problem is a two-dimensional channel with walls separated by a distance of $2d$, as illustrated in Figure 8. Because the solution for the fully developed channel flow is sought, periodic boundary conditions are used in the streamwise and spanwise directions. A constant time averaged heat flux is applied at the walls, thus providing heating to the flow. The present test flow configuration corresponds

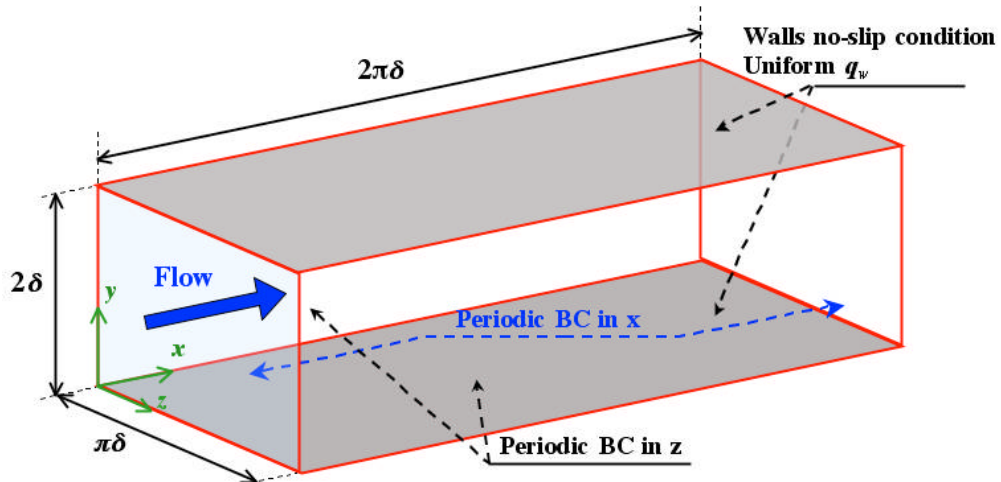


Figure 8. Computational domain for the fully developed turbulent channel flow simulation.

to that of the DNS by Kasagi et al. [63]. In this work they demonstrate that this isoflux condition is equivalent to the mean local wall temperature increasing linearly with streamwise distance. Because of a global heat balance on the channel this also results in the mean bulk temperature increasing linearly with streamwise distance. This condition can be written as,

$$\frac{\partial \langle T_w \rangle}{\partial x_1} = \frac{\partial \langle T_m \rangle}{\partial x_1} = \frac{\partial \langle T \rangle}{\partial x_1} = \text{const.} \quad (59)$$

Then, they introduce a dimensionless temperature Θ that satisfies the same boundary conditions as the velocity and is defined by

$$\Theta(x, y, z, t) = (\langle T_w \rangle - T(x, y, z, t)) / T_{ref} = [(\langle T_w \rangle - T(x, y, z, t))] / [q_w / (r C_p U_m)] \quad (60)$$

This new variable is introduced into the filtered Navier-Stokes equations, which are normalized by the bulk velocity, U_m , the half-channel height, d , and the reference temperature, T_{ref} ,

$$\frac{\partial \bar{u}_i}{\partial x_i} = 0 \quad (61)$$

$$\frac{\partial \bar{u}_i}{\partial t} + \frac{\partial \bar{u}_j \bar{u}_i}{\partial x_j} = \frac{1}{Re} \frac{\partial^2 \bar{u}_i}{\partial x_j \partial x_j} - \frac{\partial \bar{p}}{\partial x_i} - \frac{\partial \bar{t}_{ij}}{\partial x_j} + d_{i,l} f, \quad i = 1..3 \quad (62)$$

$$\frac{\partial \bar{\Theta}}{\partial t} + \bar{u}_j \frac{\partial \bar{\Theta}}{\partial x_j} = \frac{1}{Re \cdot Pr} \frac{\partial^2 \bar{\Theta}}{\partial x_j \partial x_j} - \frac{\partial \bar{q}_j}{\partial x_j} + \frac{\bar{u}_i}{U_m} \quad (63)$$

The forcing term in the streamwise momentum equation, $\delta_{l,i} f$, is zero when the equations are normalized with the bulk flow (constant mass flux in the channel). If the equations are normalized in wall units, the flow is driven by a constant pressure drop and the forcing term is $f = 1$. Because of the normalization of the temperature, the energy

transport equation displays a source term (last term on the right-hand side). This term arises from the convective term $\bar{u}_1 \frac{\partial \langle T_w \rangle / T_{ref}}{\partial x_1}$, which is simplified using an enthalpy balance in the channel and the definition of the reference temperature.

At the walls, no-slip boundary conditions are applied for the velocity components and $Q_w = 0$ is applied for the dimensionless temperature. The domain size is represented in Figure 8 and the number of grid points is reported in Table 5. The grid is uniform in all directions except for the wall-normal direction where a stretching is applied to capture the viscous sublayer. Because of the normalization by the bulk quantities, the input Reynolds number is Re_d and Re_t is a result of the simulation (i.e. measure of the wall-shear stress). The DNS of Kasagi was obtained in wall units, thus Re_t was prescribed and consequently Re_d calculated. Both RANS and LES provide excellent predictions of the wall shear stress since Re_t compares very well with DNS data.

Table 5. Computational grid and Reynolds numbers, (*) simulation input.

	Re_t	Re_d	Grid (x, y, z)
Current RANS	149.5	2290 (*)	$2\pi \times 2 \times \pi$, domain 48 x 65 x 64 points
Current LES	150.2		
DNS [63]	150 (*)	2290	$5\pi \times 2 \times 2\pi$, domain 128 x 96 x 128 points

2.3.2 Computation Details and Post-Processing

The computational domain is initialized with uniform streamwise velocity and temperature with 40% random noise. The simulation is then started and the flow

develops to a fully developed turbulent channel flow. This regime is reached when the turbulent kinetic energy in the domain reaches a steady state. The recorded data are post-processed to produce the one-dimensional statistical data ensemble averaged over time and the homogeneous direction of the flow (i.e. x and z).

The statistical variables are expressed in wall units in order to compare the results with wall turbulence scaling laws, experimental data and DNS data. Variables are normalized by the kinematic viscosity, η , the friction velocity, u_t , and the friction temperature, T_t . The later parameters are defined by:

$$u_t = \sqrt{\tau_w / r} = \sqrt{\eta \partial \bar{u} / \partial y} \Big|_w \quad (64)$$

$$T_t = \frac{q_w}{r C_p u_t} \quad (65)$$

Where the wall heat flux, q_w , is defined by $q_w = -k (\partial \bar{T} / \partial y) \Big|_w$

2.3.3 Validation Results

The Nusselt number for the channel flow is defined by,

$$Nu = \frac{2d h}{k} = \frac{2d q_w}{k (T_w - T_m)}, \quad (66)$$

where T_m is the bulk mean temperature of the flow. Using the normalized variables in simulation units, the Nusselt number is simply defined by,

$$Nu = \frac{2 \text{Re}_d \text{Pr}}{\Theta_m}, \quad (67)$$

where Θ_m is the normalized bulk temperature, $(T_w - T_m) / T_{ref}$. The Nusselt number calculated from the present simulations was 14.9 and 15.6 for the LES and the RANS.

Both values compare very well with the value of 15.4 obtained from the DNS calculation of Kasagi et al [63].

Mean statistics

Figure 9-a shows the current RANS and LES results for the mean velocity profile compared to the DNS data of Kim et al. [64]. The velocity is normalized by the centerline velocity, and the wall-normal distance is normalized by the half-channel height. Both RANS and LES results show good agreement with the DNS data. The dimensionless temperature, Q , is normalized by the centerline value as pictured in Figure 9-b. RANS and LES results display excellent agreement with the DNS data of Kasagi et al. [63] and the experimental data of Kader [65].

In Figure 10, the mean velocity and temperature results, expressed in wall units, are compared to published DNS and experimental data and the law of the wall. The velocity profiles for the current results are presented in Figure 10-a. The comparison

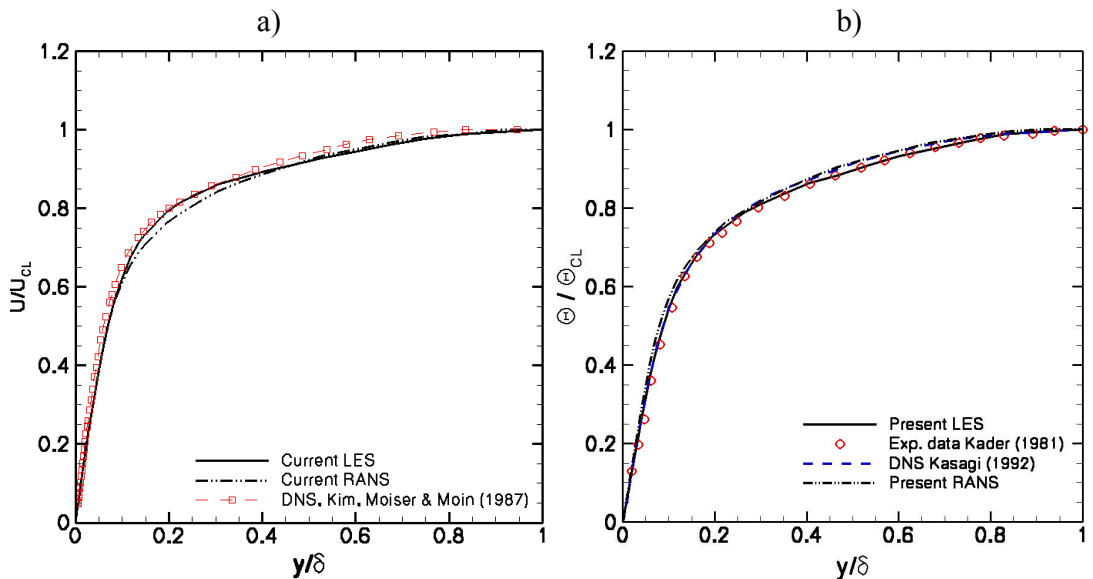


Figure 9. Mean profile: a) streamwise velocity, and b) temperature, normalized by the maximum centerline value.

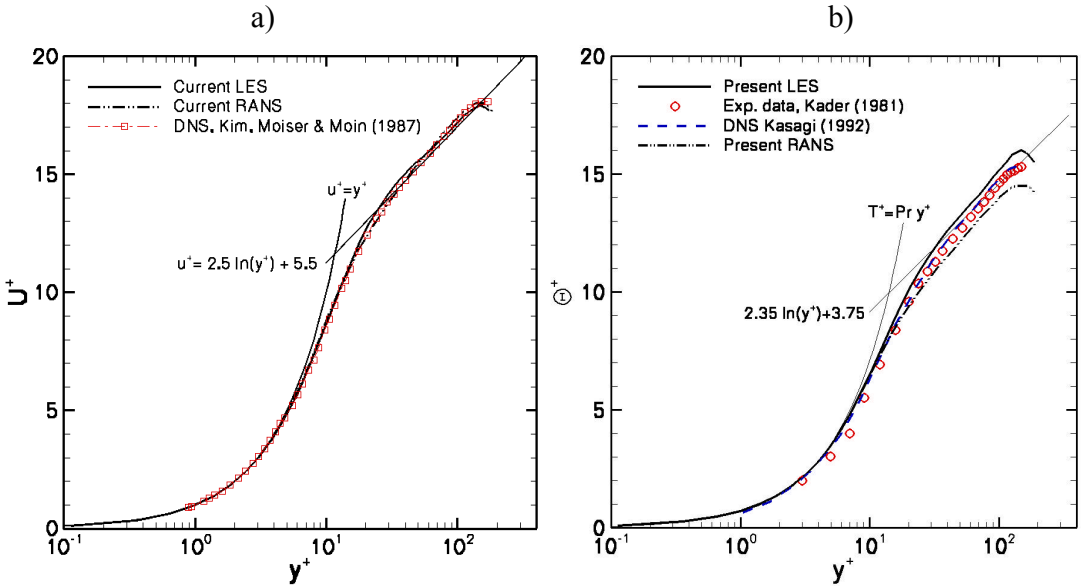


Figure 10. Mean profiles in wall units: a) streamwise velocity profile, and b) mean temperature profile, compared to DNS of Kasagi [63], experimental data of Kader [65], and law of the wall.

with the available DNS data is excellent. In the current simulations, the first grid point was located at approximately 0.1 wall units from the wall (i.e. $y^+ \approx 0.1$), thus providing a very good resolution of the viscous sublayer ($U^+ = y^+$). Present results also compare very well with the law of the wall (logarithmic region). Between the viscous sub-layer and the logarithmic layer, results indicate that the buffer layer extends from $y^+ = 5$ to about 25, in accordance with the DNS data.

The temperature profiles in wall units presented in Figure 10-b, also show good agreement with the DNS data of Kasagi et al. [63] and the experimental data of Kader [65]. The viscous sublayer is well captured. Some scatter is evidenced in the logarithmic region, because the log law for temperature is not as universal as the one for the velocity [49]. Nonetheless, the present RANS and LES results are within less than 3% of the DNS data and therefore display a good performance.

Higher order statistics

The profile of dimensionless RMS temperature in wall units, \mathbb{Q}_{rms} , is compared to the DNS data in Figure 11-a. The results show excellent agreement in the viscous sublayer. The location of peak RMS at $y^+ \approx 20$ matches the DNS data, but the LES overpredicts by nearly 4% the RMS value at the peak. In the logarithmic layer range, the RMS is well predicted but then tends to be overpredicted at the center of the channel ($y^+ = 150$). Overall the agreement between current LES results and the DNS data is good.

The streamwise and wall-normal turbulent heat fluxes are presented in Figure 11-b and expressed in wall units. The streamwise turbulent flux, $\overline{u'^+\Theta'^+}$, is always positive and peaks at the location of maximum temperature RMS. The LES results compare very well in the viscous sublayer but then tend to overpredict the streamwise turbulent heat flux by nearly 7%. The wall-normal turbulent heat flux term, $\overline{v'^+\Theta'^+}$, is negative

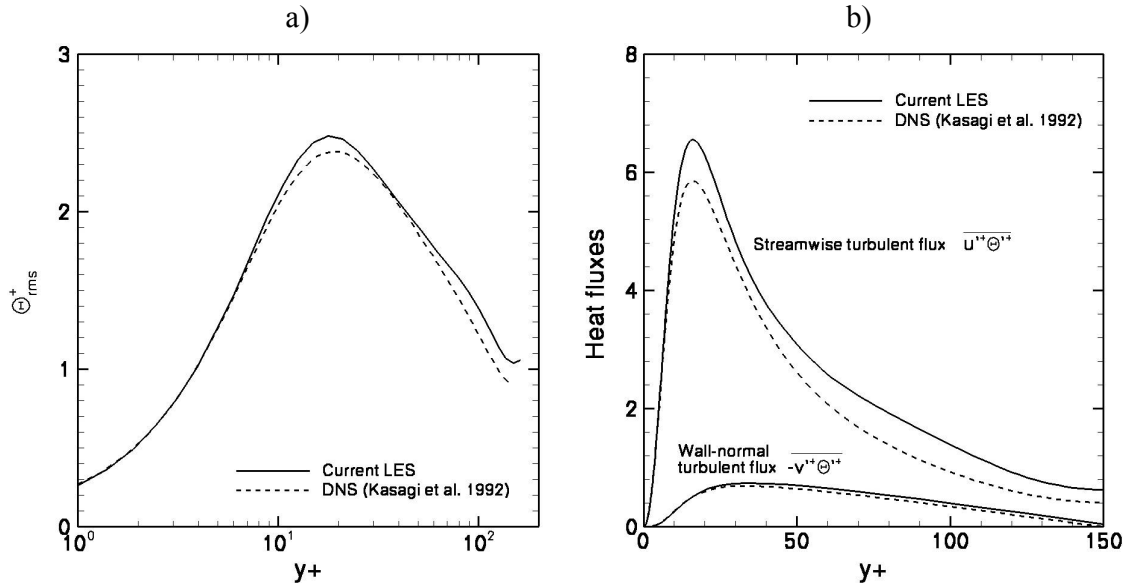


Figure 11. Temperature statistics in wall units; a) RMS of the dimensionless temperature, and b) streamwise and wall-normal turbulent heat fluxes.

everywhere except at the wall and at center of the channel where it vanishes. This is in accordance with turbulent channel theory. For this term, the LES results agree nearly perfectly with the DNS data.

2.2.4 Summary of the validation test

The validation test showed that both RANS and LES predict accurately the near-wall quantities: the wall shear stress (i.e. Re_t) and the Nusselt number are well predicted. Mean quantities such as the streamwise velocity and the temperature profiles are in excellent agreement with DNS and experimental data. The simulation results also match the scaling in the viscous sublayer and logarithmic region.

Since the Spalart-Allmaras model used in the RANS simulations does not provide information on the first and higher order statistics, RMS quantities are only available in the LES results. The temperature RMS and turbulent heat fluxes in the streamwise and wall-normal directions display good agreement with the DNS data.

Consequently, the RANS and LES models implemented in the code can be used with confidence to tackle the slot film-cooling problem.

Chapter 3: Film Cooling Flow Analysis

The objective of this chapter is to analyze the main mechanisms that govern the mixing of the coolant film based on experimental data obtained in the hot wind tunnel facility. First we present an overview of the physical phenomena that have been identified to contribute to the film mixing and the loss of film cooling effectiveness in previous studies. From this overview we emphasize the fact that determining the film cooling effectiveness is a pure mixing problem. For the non-adiabatic wall cases, the heat transfer problem is influenced by the mixing and the near-wall transport. Both of these aspects are explored using detailed flow and surface measurements.

3.1 Introduction

3.1.1 Overview of the physics

The basic characteristics of the film cooling flow are pictured in Figure 12. The coolant flow is injected through a two-dimensional slot of height, $s = 4$ mm, and flow downstream creating a layer that thermally protects the wall. In addition to the velocity difference between the coolant and mainstream a region of strong shear is created behind the louver lip of thickness $t = 0.76$ mm. The flow in this region is complex since it displays characteristics common to a wake flow and a mixing layer. We can define the Reynolds number, Re_t , based on the louver thickness and the characteristic velocity $(U_\infty + U_c)/2$. For all the cases considered in this study, Re_t reaches low values in the range 760 to 1000. Consequently Kármán vortex instabilities are expected behind the louver in the wake region [32]. In the mixing layer region, Kelvin-Helmholtz instabilities are

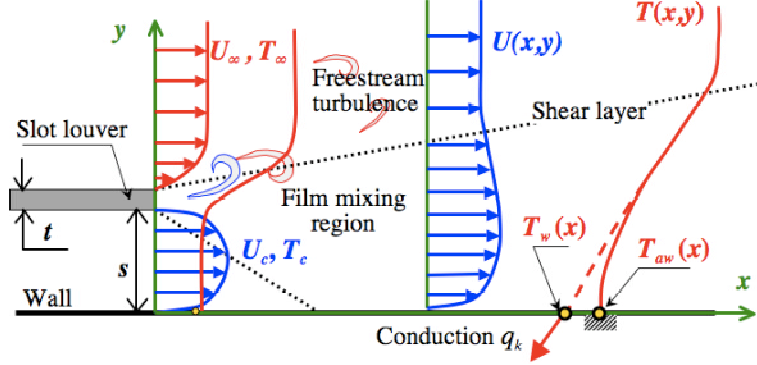


Figure 12. Schematic of the film cooling flow physics

generally created when the velocity ratio is not equal to unity [32]. These main mechanisms drive the initial mixing of the film, which is also influenced by the turbulence levels in the coolant and the mainstream [69]. From the interaction of the flow with the wall and between the two streams, pockets of high temperature fluid are transported towards the wall. In the case of a perfectly insulated wall the resulting adiabatic temperature, T_{aw} , distribution along the wall indicates the level of thermal mixing and thus the performance of the film. When normalized by the inlet temperatures, the adiabatic wall temperature becomes the adiabatic film cooling effectiveness, \hbar_{aw} , defined by [11]

$$\hbar_{aw} = (T_{\infty} - T_{aw}) / (T_{\infty} - T_c). \quad (68)$$

This parameter represents the effects of the thermal mixing at the wall in terms of inlet temperature conditions. It takes values of zero in the mainstream and unity near the slot exit.

In the case of a non-adiabatic wall (i.e. heat transfer through the wall), the resulting wall temperature is smaller than the adiabatic wall temperature as indicated in Figure 12. In this case, Goldstein [11] demonstrated that the convective heat flux (per

unit area), q_c , should be evaluated by using T_{aw} as the reference temperature in Newton's law of cooling,

$$q_c = h(T_{aw} - T_w) = h(T_\infty - \hbar_{aw}(T_\infty - T_c) - T_w). \quad (69)$$

Rewriting this expression in terms of \hbar_{aw} gives significant insight into the meaning of the adiabatic effectiveness. If \hbar_{aw} is equal to zero (i.e. when the film is destroyed) the convective heat flux at the wall is governed by the mainstream temperature, T_∞ , similar to the classic isothermal boundary layer configuration. If \hbar_{aw} equals unity (i.e. when the film is unaltered) q_c is governed by the coolant temperature, T_c . Therefore \hbar_{aw} represents the effective mixing of the film near the wall. The convective heat transfer coefficient h quantifies the degree of augmentation of transport from the flow to the wall. Both parameters strongly depend on the flow characteristics of transport and mixing. Furthermore \hbar_{aw} and h are equally important in evaluating the convective heat flux to solve the heat transfer problem in a real combustor or thrust chamber. Consequently these quantities need to be accurately calculated for engineering design and development.

Inlet conditions must be accurately characterized to serve the analysis of the measurements of \hbar_{aw} and h . Mean measurements of the velocity and temperature are useful, however turbulence statistics (RMS) of these quantities at the inlet also constitute valuable information. Several investigations have studied the effect of freestream turbulence on the film cooling effectiveness demonstrating the importance of this parameter. When the film is injected through inclined discrete holes, high freestream turbulence has been shown to reduce the effectiveness at low blowing ratios because increased mixing of the film causes high temperatures near the wall ([67], [68]). But at high blowing ratios, high turbulence intensity actually increases the film effectiveness

because it reduces the jet lifting and results in better film spread and better wall coverage [67]. Previous experimental studies ([7], [69]) have also shown that when the film is injected through a tangential slot, high freestream turbulence invariably leads to a reduction in film cooling effectiveness for high and low blowing ratios. Finally Simon [8] showed that for the slot film-cooling configuration, both the freestream and coolant wall-normal RMS levels are important to the film effectiveness. Furthermore, the freestream turbulence is shown to have a reduced effect at high blowing ratios. Even though the objective of the present study is not to investigate the effects of inlet turbulence *per se*, we acknowledge the importance of this parameter and aim to provide detailed inlet turbulence data because they are critical for the understanding of the flow and for performing advanced numerical simulations such as LES.

3.1.2 Experimental conditions

The experimental operating conditions are summarized in Table 6. Experimental cases are categorized by the velocity VR , defined by U_c/U_∞ , rather than by the blowing ratio, m , because all the cases have the same density ratio or temperature ratio ($TR \approx 1.5$). Decoupling the effects of the density ratio allows for focus on the kinematic mixing mechanisms of these flows. Three situations are investigated: a wall-wake case (VR0.5), a boundary layer case (VR1.0) and a wall-jet case (VR2.0). For each situation, adiabatic and backside cooled wall experiments are conducted.

Table 6. Experimental operating conditions

Tests →	VR0.5a	VR0.5	VR1.0a	VR1.0	VR2.0a	VR2.0
Wall →	Adiabatic	Backside cooled	Adiabatic	Backside cooled	Adiabatic	Backside cooled
U_c (m/s)	10.82	10.82	19.13	19.13	21.20	21.20
U_∞ (m/s)	24.86	24.86	22.10	22.10	11.10	11.10
$VR = U_c/U_\infty$	0.44	0.44	0.87	0.87	1.93	1.93
T_c (K)	304.78	306.11	298.88	304.43	296.33	301.54
T_∞ (K)	462.02	454.94	454.33	446.33	462.92	437.89
$TR = T_\infty/T_c$	1.52	1.49	1.52	1.47	1.56	1.45
Re_s	2652	2631	4857	4698	5466	5297
$m = VR \ TR$	0.66	0.65	1.32	1.27	3.01	2.80

3.2 Comparison of Cases

In this section we compare the performance of the experimental cases in terms of film cooling effectiveness, wall temperature, and wall heat flux.

3.2.1 Pure mixing, the film cooling effectiveness

Previous film cooling studies have emphasized that a successful characterization of the film mixing is intimately related to well defined inlet conditions. Consequently mean inlet velocity and temperature profiles are presented in Figure 13. The velocity profiles pictured in Figure 13-a were obtained from PIV measurements during the experiments using the settings described in Chapter 2. Temperature profiles displayed in Figure 13-b were measured with the micro-thermocouple probe. Both velocity and temperature data are normalized by the hot mainstream conditions.

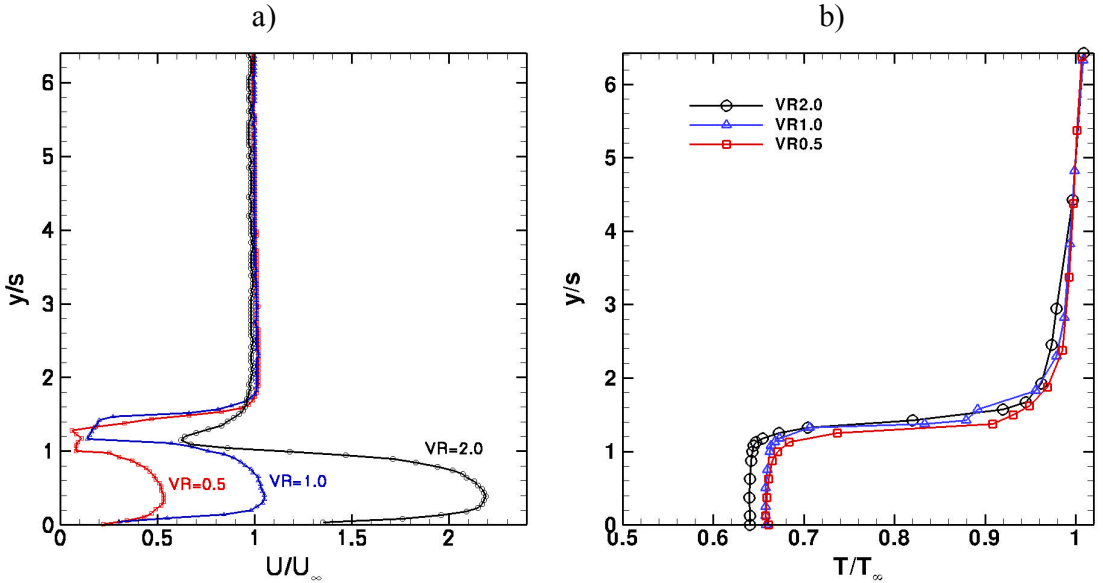


Figure 13. Experimental inlet conditions for the adiabatic cases; a) Mean velocity profiles normalized by the mainstream velocity U_∞ , b) Mean temperature profiles normalized by the mainstream temperature T_∞ . Mainstream velocity and temperatures are reported in Table 6 for the three adiabatic cases presented.

The profiles for the wall-jet (VR2.0), minimum shear case – boundary layer case – (VR1.0) and the wall-wake flow (VR0.5) are all normalized by their respective mainstream streamwise velocity and temperature reported in the test matrix of Table 6. The three cases selected in this work display different characteristics. The wall-jet case (VR2.0a) displays a strong negative velocity gradient from the coolant to the mainstream, further emphasized by the wake resulting from the louver lip or splitter plate. Opposite to this case is the wall wake case (VR0.5a) with a strong positive velocity gradient from the coolant to the mainstream. Finally, the baseline boundary layer case (VR1.0a) completes the test matrix with a minimum shear between the coolant and the mainstream.

The normalized mean temperature profiles display similar shapes for all the cases presented in Figure 13-b. Within the slot, $y/s \leq 1$, the temperature of the coolant is uniform with a zero-gradient condition at the wall illustrating the effective thermal

insulation and adiabatic wall condition. The temperature ratio T_∞/T_c was kept constant for all the cases considered in this study. Consequently, all of the normalized temperature profiles take approximately the same values around 0.65 near the wall. Steep temperature gradients are observed behind the louver lip and the temperature then reaches the hot mainstream conditions within a short wall-normal distance. Small differences are noticeable in the boundary layer region of the mainstream (i.e. $y/s \geq 1.19$) due to different pre-cooling conditions through the louver created by the different coolant flow conditions. This is particularly noticeable for cases VR1.0 and VR0.5, which have similar mainstream conditions but VR0.5 has a lower coolant flow rate thus providing less pre-cooling of the mainstream thermal boundary layer.

Measured adiabatic wall temperature distributions along the wall are presented in Figure 14-a for the wall-jet, boundary layer and wall-wake flow. Due to data recording issues, the temperature measurements for the wall-wake case (VR0.5) cannot be presented. However, measurements at nearly identical conditions were previously taken in the same facility and published [12] (case 2). The conditions for this case ($m = 0.76$, $VR = 0.46$, and $Re_s = 1790$) match very well the present conditions in Table 6, despite a smaller Reynolds number. Near the slot exit, the adiabatic wall temperatures in Figure 14-a are different because the slot coolant temperature varies from one case to the other. This variation cannot be avoided because it results from differences in ambient conditions and more importantly because of different flow pre-heating conditions through the louver. Nevertheless one can easily notice that the boundary layer case (1.0AD) presents the least increase in temperature along the wall. The wall-wake flow (0.5AD) has the largest slope and temperature increase indicating that film is being vigorously destroyed.

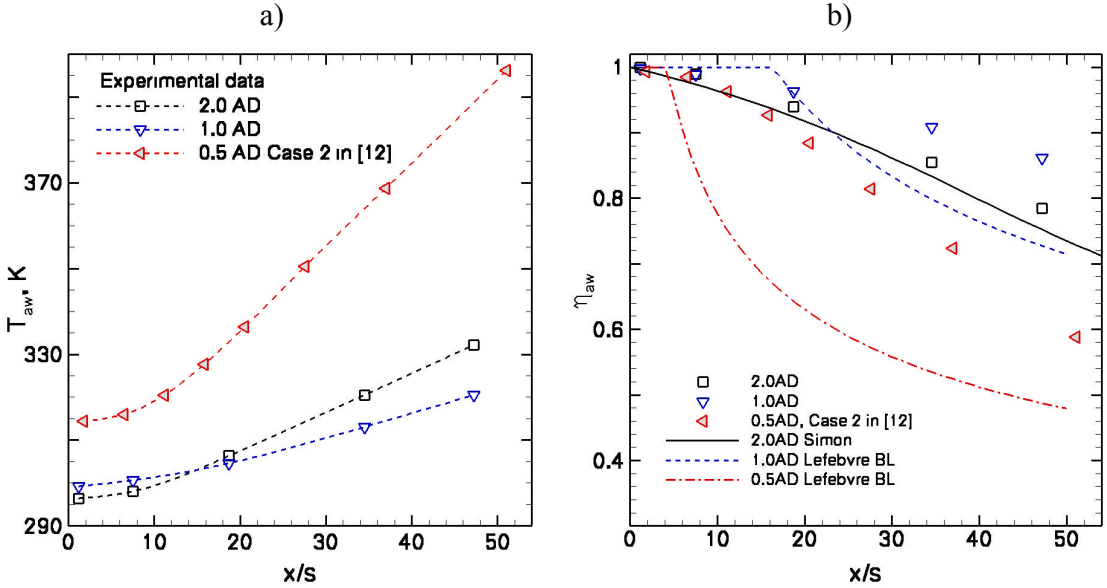


Figure 14. Adiabatic wall temperature distribution; a) absolute adiabatic wall temperature, T_{aw} , in Kelvin, b) dimensionless form the film cooling effectiveness, $h_{aw} = (T_\infty - T_{aw}) / (T_\infty - T_c)$.

Interestingly for the wall jet case (2.0AD) T_{aw} increases strongly and almost linearly after 10 slot heights downstream of the injection.

The measured adiabatic film cooling effectiveness, h_{aw} , and predictions from correlations of Simon [8] and Lefebvre [1] are compared in Figure 14-b. This comparison reveals that the Simon model provides a reasonable estimate of h_{aw} for the wall jet case (VR2.0) with a slight under-estimate of less than 5%. For the boundary layer case (VR1.0), Lefebvre's correlation does not capture the general trend and only provides a rough estimate of h_{aw} with errors as large as 10%. Lefebvre's correlation performs even worse for the wall-wake case (VR0.5), where the effectiveness is strongly under-predicted by nearly 20%. Measurements show that the difference in effectiveness over a wide range of velocity ratios does not exceed 25% and most importantly that VR1.0 provides the best film effectiveness along the entire wall, a trend not evidenced from the correlations. The hypothesis that this is due to smaller initial shear resulting in

less mixing will be investigated through an analysis of the flow statistics. Measurements also reveal that the wall wake case (VR0.5) performs quite well except in the far field where the adiabatic wall temperature has reached high values, and thus the effectiveness is low.

The comparison illustrates that in general the correlations perform poorly except the Simon model for the wall jet. This is significant because even a 5% error in the effectiveness can lead to large errors in the heat flux calculation, which also requires an estimate of the convective heat transfer coefficient. To analyze the wall heat fluxes, we consider the non-adiabatic experiments with backside cooling, a configuration characteristic of both liquid fuel rockets and gas turbine combustors.

3.2.2 Effect of backside cooling

In this section we present experimental measurements for the non-adiabatic wall versions of cases VR0.5, VR1.0 and VR2.0. Table 6 shows that the inlet and operating conditions are nearly identical to the corresponding conditions for the adiabatic wall. This was necessary to ensure that the heat transfer measurements can be related to the adiabatic film cooling effectiveness.

Figure 15 shows the streamwise distribution of the wall temperatures normalized by the inlet temperatures for all the non-adiabatic cases. This temperature normalization facilitates a direct comparison between the cases since 0 corresponds to the film coolant temperature and 1 to the hot mainstream[†]. The wall temperature, T_w , the backside wall temperature, T_{wb} , and the film coolant temperature, T_c , are plotted in Figure 15. The

[†] This normalization is equivalent $1-h$, where h is the effectiveness.

backside temperature is nearly constant and the same for all the cases, a feature obtained by having the same backside coolant mass flow through the cooling channel. The wall temperature of VR1.0 increases less than the other cases, thus illustrating that the film also performs best for this flow under cooled wall conditions. Cases VR0.5 and 2.0 display a lower and similar performance in that respect. Since experiments were carried out with the same wall, the difference ($T_w - T_{wb}$) is proportional to the conductive heat flux through the wall and also to the level of thermal stresses the wall sees. From this perspective, VR1.0 also performs best in reducing the thermal stresses. Near the injection region, one notices that the wall temperature remains lower than the film coolant injection temperature for a short distance. This effect is due to the backside cooling of the film layer close to wall and is more pronounced for the wall-wake flow (VR0.5) where the coolant flow rate is lower than in the other cases.

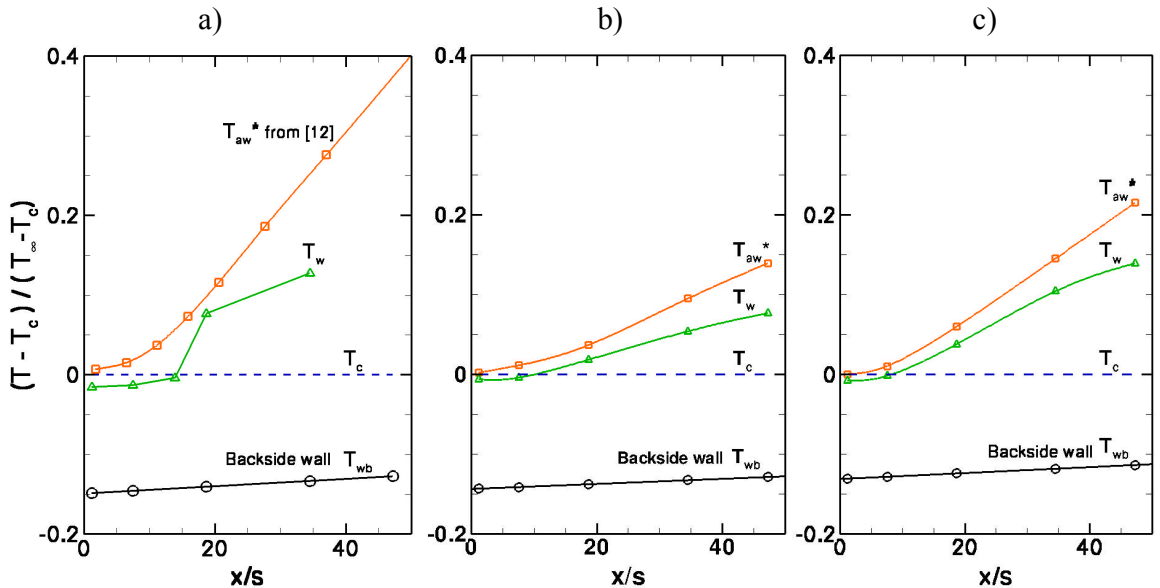


Figure 15. Wall surface temperatures normalized by $(T - T_c)/(T_\infty - T_c)$, illustrating the effect of backside cooling; a) Wall wake flow VR0.5 , b) Boundary layer case VR1.0, and c) Wall-jet case VR2.0

The plots also include T_{aw}^* , the corrected adiabatic wall temperature that accounts for the small differences in inlet temperature between the adiabatic and non-adiabatic experiments using

$$T_{aw}^* = T_\infty - h_{aw}(T_\infty - T_c), \quad (70)$$

where T_c and T_∞ are taken from the non-adiabatic experiments and h_{aw} is determined from the corresponding adiabatic experiments. For all the cases, T_w is less than T_{aw}^* illustrating the effectiveness of backside cooling in wall temperature reduction. In the far field, T_{aw}^* is highest in the wall-wake and lowest in the boundary layer case. The profiles of T_{aw}^* display similar increasing trends as the wall temperature profiles, but tend to deviate further downstream. The wall temperature for the wall-wake case increases sharply at $x/s = 18.7$. The difference ($T_{aw}^* - T_w$) is an important quantity since it is related to the convective heat flux at the wall through the relation $q_c = h (T_{aw}^* - T_w)$. The data show that the difference ($T_{aw}^* - T_w$) is the largest in the wall-wake flow and smallest in the wall-jet case. This illustrates the difference in near wall convective heat transfer of these flows.

The three heat transfer modes (i.e. radiation, conduction and convection) computed from experimental data are presented in Figure 16. The reader is reminded that the conduction heat flux (q_k) is obtained from direct measurements using Eq. (22), the radiation (q_r) is estimated from measured surface temperatures, the convective heat flux (q_c) is determined from an energy balance.

$$q_c = q_k - q_r \quad (71)$$

See Eqs. (22)-(24) and Figure 5 in Chapter 2. Figure 16 shows that in all cases, the radiation heat flux is small compared to the other terms and that it decreases with streamwise distance as the wall temperature increases to approach the casing temperature. While radiation is small it cannot be neglected and is especially near the injection location.

In the near-field region ($0 \leq x/s \leq 10$), the convection is largest for VR1.0, followed by the wall-wake and finally the wall-jet case but the differences are relatively small. Further downstream significantly different behaviors are noticeable. For VR1.0, the streamwise rate of increase of the convection is small compared to the other cases, resulting in convective heat fluxes of 1100 W/m^2 by the end of the measurement region. The wall-wake case shows a different behavior with a steep increase in the convective heat flux at $x/s = 15$. The last measurement point indicates large heat flux levels of

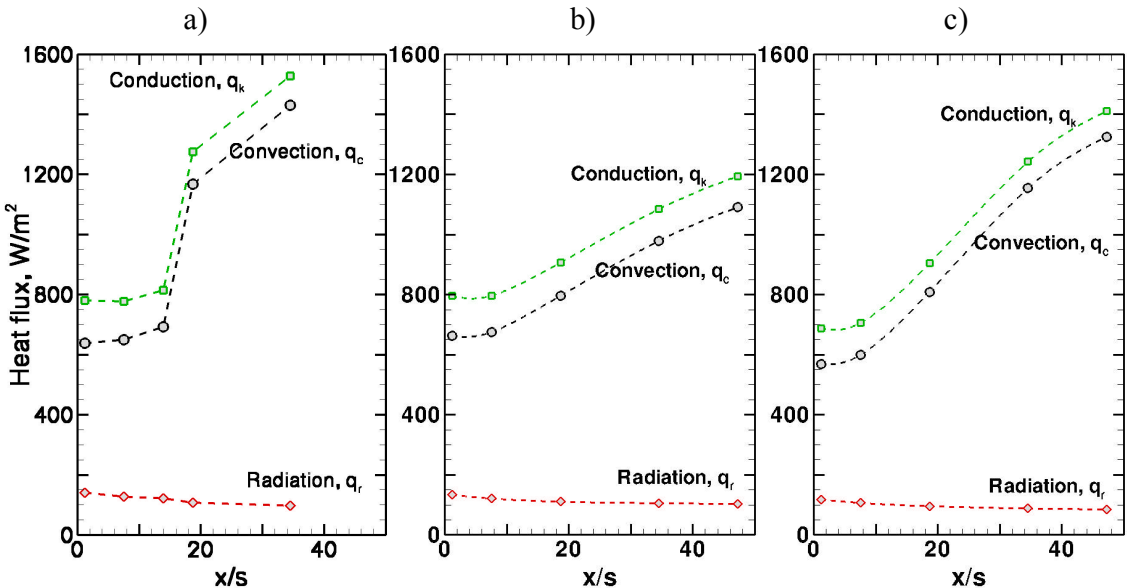


Figure 16. Measured heat fluxes at the film cooled wall in W/m^2 ; a) VR0.5NA, b) VR=1.0NA, c) VR=2.0NA.

1500W/m² at $x/s = 35$. The levels of heat flux are directly related to the large wall temperatures that result from the strong mixing and film destruction.

The heat transport at the wall is generally quantified by the convective heat transfer coefficient, h , which along with the effectiveness, is the most important parameter of the film-cooling problem. Obtained from experimental data by the relation $h = q_c / (T_{aw}^* - T_w)$, the results for this coefficient are reported in Figure 17-a with the error bars corresponding to the uncertainty. The convective heat transfer coefficient is not presented for the wall-wake case because the adiabatic and non-adiabatic wall temperatures were not obtained at the exact same conditions and Reynolds number. Therefore only the wall jet case and boundary layer case are presented. The relative uncertainty in h is large when the difference $(T_{aw}^* - T_w)$ is small. Therefore the uncertainty in h is large near the film injection point. Nevertheless the data obtained in this study are valuable for better understanding convective heat transport in the near field - a region that has been overlooked in previous studies. Figure 17-a indicates that the wall jet and boundary layer cases have similar convective heat transfer coefficients, with large values in the near field that decrease with streamwise distance. Since both cases (VR1.0 and VR2.0) have similar film injection velocities, this illustrates the fact that h is mainly governed by the slot flow dynamics and transport properties. In the far field, h of wall jet case is decreasing at a higher rate, thus indicating that the heat transport is reducing due to the expected decrease in the maximum velocity of the wall jet. Further analysis of the flow kinematics (next section) will shed some light on the flow scaling and at what x/s do the freestream dynamics take over the transport mechanism.

Figure 17-b shows h normalized by the mainstream conditions in the form of the

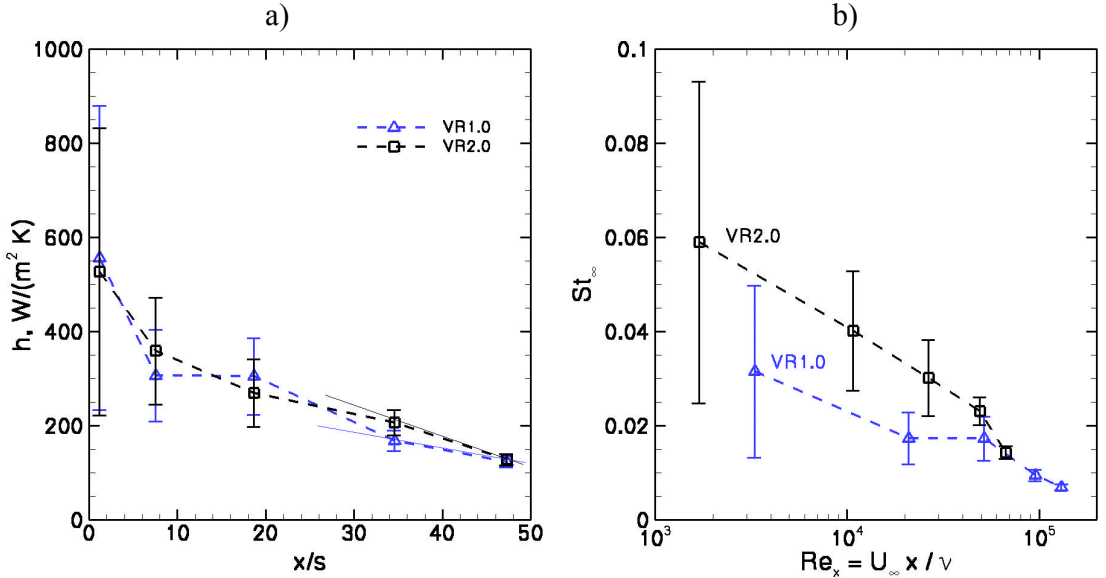


Figure 17. Convective heat transport; a) convective heat transfer coefficient in $\text{W}\cdot\text{m}^{-2}\cdot\text{K}^{-1}$, b) Stanton number $St = h / (\rho C_p U_\infty)$ versus $Re_x = x U_\infty / \nu$, in logarithmic scale.

Stanton number, St_∞ , plotted against Re_x , the local Reynolds number based on the freestream conditions and the distance downstream of the slot exit. Normalizing the data with the freestream conditions emphasizes the heat transport differences in the near field, where the wall-jet case displays the highest Stanton number. The rate of decay of the Stanton number is also different for these two cases. This illustrates the inherent differences between these flows, especially in the near-field region where the transport is governed by the coolant flow. However, further downstream the curves tend to collapse into a single Stanton number profile, indicating that transport becomes dominated by the freestream. Even though the measurement domain is not long enough to explore this trend further downstream, we remind the reader that this work is focusing on the near and mid field ($x/s \leq 50$) because this region is critical for engineering applications and remains poorly characterized in the literature.

In order to further understand the thermal transport in these flows, one needs to

examine the flow velocity and temperature measurements.

3.3 Thermal and Momentum Mixing

In this section we analyze measurements of flow temperature and velocity profiles and some aspects of the scaling relevant to the mixing behavior of the flows.

3.3.1 Temperature mixing and scaling

For each experimental case, temperature profiles were measured at various streamwise distances from the film injection point. Sampled at 20 kHz over 15 seconds, the raw data were post-processed and compensated for the thermal inertia of the probe using the signal processing method described in Chapter 2. This method allows the recovery of most of the power of the turbulent temperature fluctuations. In this section, we aim at presenting the main differences between the experimental cases in terms of thermal mixing.

Mean temperature profiles

First it appears necessary to understand the impact of the wall boundary condition on the temperature profiles. Figure 18 shows the dimensionless temperature profiles, \hbar , for the adiabatic and non-adiabatic wall conditions of the wall jet case VR2.0. Both cases display similar profiles with cold flow near the wall and hot flow in the mainstream. The first profiles present large gradients that tend to be smoothed out further downstream. Most of the differences between the adiabatic and non-adiabatic conditions are restricted to the near-wall region. Zero-gradient conditions at the wall are observed for all the adiabatic profiles whereas for the non-adiabatic case, the initially negligible gradient gradually increases downstream. Of particular interest is the fact that the temperature at

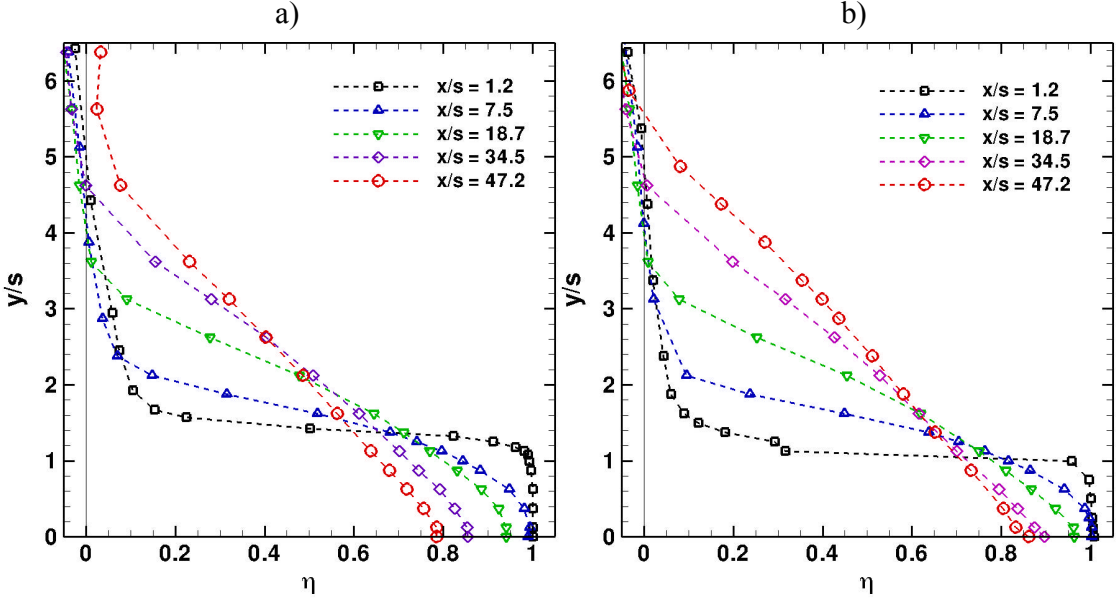


Figure 18. Comparison of dimensionless temperature profiles for adiabatic (a) and non-adiabatic (b) conditions for the wall jet cases of $VR=2.0$. $h = (T_\infty - T)/(T_\infty - T_c)$

the wall is cooler (i.e. h closer to unity) in the non-adiabatic case. This feature, due to backside cooling effects, has been described earlier. However, the effects of this boundary condition change are less pronounced further away from the wall. For instance, at the furthest streamwise location the mainstream temperature is reached nearly at the same wall-normal location in the adiabatic and non-adiabatic case. These observations indicate that the flow temperature differences between the adiabatic and non-adiabatic wall experiments are small and are restricted to the near-wall region. Consequently, we will investigate the thermal mixing characteristics of the different flows only for the adiabatic wall experiments.

Mean temperature scaling

Based on his early experimental data, Wieghardt [3] proposed scaling quantities for the flow temperature and the wall-normal distance that collapse the data into a

similarity profile once the flow reaches the self-similar regime. The temperature is scaled based on freestream and local adiabatic wall temperatures,

$$q = \frac{T_\infty - T}{T_\infty - T_{aw}}, \quad (72)$$

and the wall-normal distance is normalized by the thermal thickness d_T defined by

$$d_T(x) = \int_0^\infty \frac{T_\infty - T(x,y)}{T_\infty - T_{aw}} dy. \quad (73)$$

Figure 19-a shows the dimensionless temperature profiles of case VR2.0AD normalized using Wieghardt similarity variables. Experimental data are plotted against Wieghardt semi-empirical scaling law derived in the self-similar region of the flow [3],

$$q \equiv \frac{T_\infty - T}{T_\infty - T_{aw}} = \exp \left[-0.768 \left(\frac{y}{d_T} \right)^{13/6} \right]. \quad (74)$$

Near the slot injection, at x/s of 1.2, the experimental profile deviates from the similarity profile. However the thermal mixing rapidly acts on the flow such that at 7.5 slot heights downstream of the injection, the experimental profile is approximated within 4% by the scaling law. Further downstream (beyond $x/s = 18.7$) experimental data collapse very well on top of Wieghardt profile, indicating that the flow has reached a state of thermal self-similarity.

This behavior is also observed for the other cases (boundary layer and wall wake), as pictured in Figure 19-b. Even though these flows have very different heat transport properties and flow kinematics, the temperature profiles follow the similarity profile of Wieghardt starting at a distance less than 20 slot heights downstream of the injection. This finding is remarkable because it validates the assumption of temperature profile

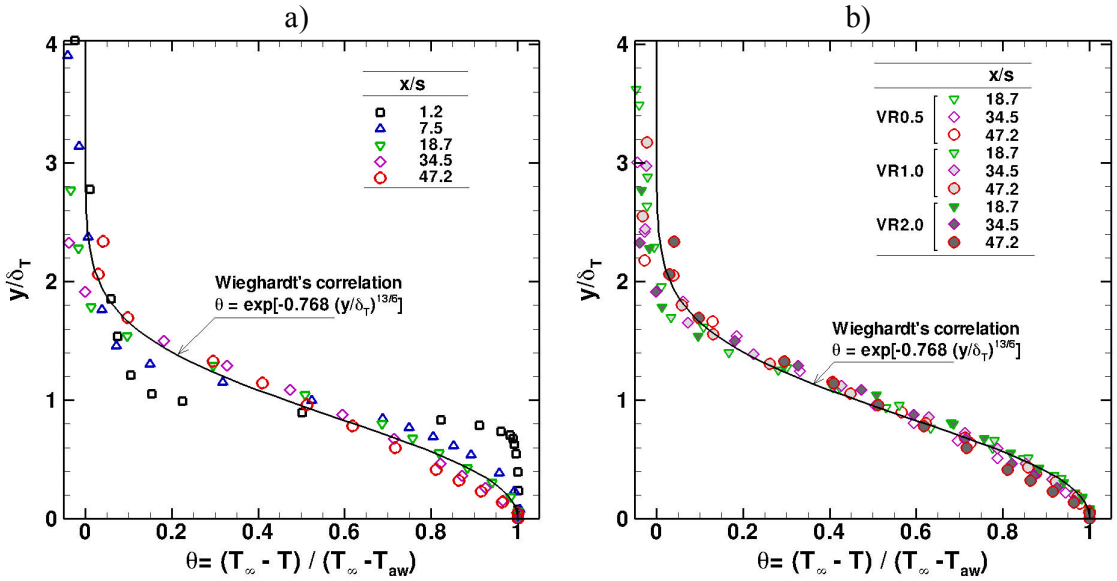


Figure 19. Dimensionless temperature profile with Wieghardt similarity scaling; a) Adiabatic wall jet case VR2.0, b) All the adiabatic cases (VR0.5, VR1.0, and VR2.0) downstream of $x/s = 18.7$.

similarity used to derive the film cooling effectiveness correlations, as explained in Chapter 1. However, if used from x/s of 0 to about 10, this assumption can introduce errors in the correlation for h_{aw} . Very often these errors are deemed negligible since the mixing is not very strong in this region and the effectiveness is usually close to unity.

Although the temperature profiles scale very well with the Weighardt profile, the thermal mixing in these flows is different. For instance the thermal thickness (d_T) grows at different rates with the streamwise distance, as illustrated in Figure 20. This measure is a characteristic length scale representing the mixing region normal to the wall. According to Wieghardt's profile in Figure 19, at $y = d_T$ the flow temperature has increased from the adiabatic wall temperature by 56% of the range ($T_\infty - T_{aw}$). At $2d_T$ away from the wall the flow temperature has reached 97% of that same range and is nearly equal to the freestream temperature. This helps us to understand that most of the thermal

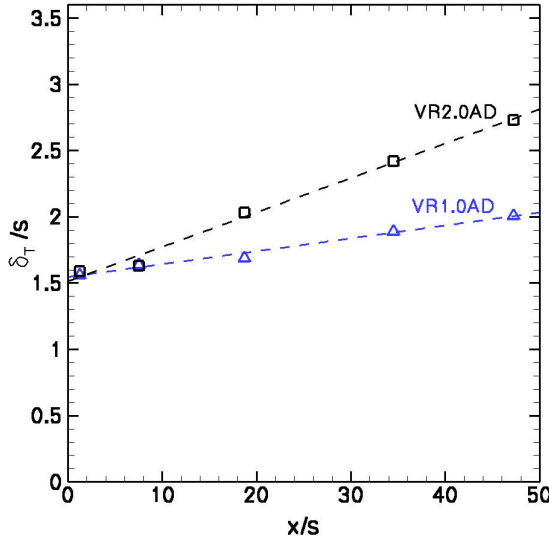


Figure 20. Wieghardt thermal thickness along the wall, adiabatic cases.

mixing actually occurs between the wall and $2d_T$. The streamwise evolution of d_T is presented in Figure 20 for the wall jet and boundary layer case. The experimental data indicate that d_T starts nearly at the same value and increases linearly in both cases. The slope of the wall jet is larger than that of the boundary layer case, indicating that the thermal spreading rate is much faster for the wall jet. The thermal mixing for the wall jet case is occurring within a significantly larger region (large scale mixing), which partially explains why the film cooling effectiveness is better in the boundary layer case. So far, we have seen that the thermal mixing is characterized by a length scale. However, it is also characterized by a temperature scale that indicates the level of turbulent mixing. Therefore, we will also examine the temperature RMS data for both of these cases to further characterize the thermal.

Flow temperature statistics

The profiles of flow temperature RMS shown in Figure 21 are normalized using

Wieghardt scaling, i.e. T_{rms} is normalized by the difference between the local adiabatic wall temperature and the freestream temperature. Unlike the mean temperature profiles, it is apparent that the RMS of the temperature does not scale to a single similarity profile. For both the boundary layer and wall jet cases, the RMS starts with low values at the injection (low mixing) then increases further downstream. The normalization of the wall-normal distance by the thermal thickness, d_T , shows that the peak RMS is initially located at $y = d_T$, for both cases. Using the wall distance normalized by d_T also provides an easy access to the local mean temperature when analyzing the RMS profiles. Indeed, according to Wieghardt scaling, the mean temperature reaches 56% and 97% of $(T_\infty - T_{aw})$, at d_T and $2d_T$ respectively. For the boundary layer flow, the peak RMS remains at $y = d_T$ further downstream, whereas for the wall jet case the location of peak RMS shifts away from the wall ($y = 1.3d_T$) toward the high temperature freestream. The peak temperature RMS is larger for VR1.0 than for VR2.0. This fact may seem surprising since we have seen that VR1.0 produces less mixing at the wall and a better effectiveness. However, temperature RMS profiles in the near-wall region confirm this trend as the RMS levels at the wall are lower for VR1.0. In fact the thermal mixing for the wall jet is not only spreading to the outer layer but also to the inner layer close to the wall, as evidenced by the nearly flat profile at the furthest streamwise location. A very different behavior is witnessed for the boundary layer case, where the region of strong mixing does not interact as strongly with the near-wall region.

In conclusion, even though the peak RMS is higher in the boundary layer case, the active mixing region remains contained in the outer layer ($y = d_T$) thus resulting in small effects on the inner layer (near the wall) and the corresponding wall temperature. On the

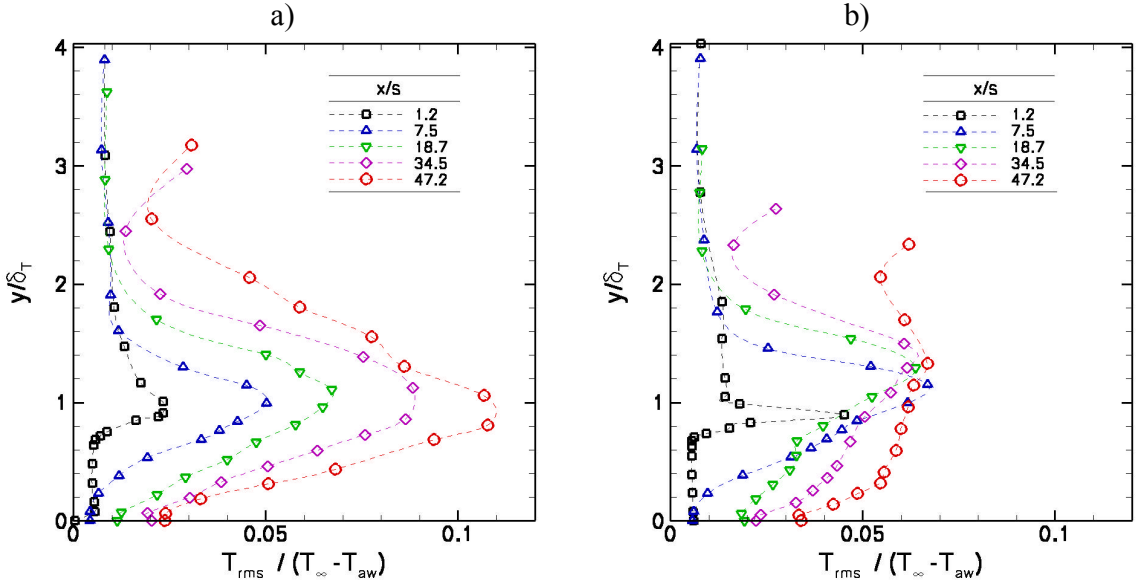


Figure 21. Profiles of flow temperature RMS normalized the local scale ($T_{\infty} - T_{aw}$); a) case VR1.0AD, and c) VR2.0AD

other hand, the mixing region of the wall jet spreads in the wall normal direction towards the wall and the freestream, thus resulting in stronger mixing near the wall. The thermal mixing is mainly governed by the flow transport properties. Given the different flow kinematics of these cases we will investigate the velocity data.

3.3.2 Characteristics of the momentum mixing

In this section, we analyze the velocity data obtained from PIV measurements for the flow configurations considered in this study. The mean streamwise velocity profiles at the inlet of the test section were presented at the beginning of this chapter, and illustrated the differences between the wall-wake, boundary layer and wall-jet (respectively VR0.5, VR1.0 and VR2.0). Differences in the velocity field have already been identified as the main mechanism driving the thermal mixing and hence the film performance. Therefore the momentum mixing is explored in this section.

Mean and RMS velocity profiles

The velocity was measured with the planar PIV system using a 50 by 50 mm field of view. Consequently the PIV system was traversed at four downstream locations to obtain velocity measurements of the flow field in the entire domain for x/s in the range 0 to 50. At each streamwise station, 1000 pairs of images were acquired to produce the turbulent statistics. This number of samples was deemed sufficient to obtain convergence of the first and second order statistical moments (i.e. mean and RMS).

Figure 22 shows the mean streamwise velocity profiles normalized by the freestream velocity for the three velocity ratios considered in this study. The profiles are shown at the streamwise locations corresponding to the flow temperature measurements. For all of the flows, the velocity deficit behind the louver lip is quickly dissipated and virtually vanishes at 7.5 slot heights downstream of the inlet. For the wall-wake flow (VR0.5), the extra velocity deficit introduced by the slow moving coolant flow transitions

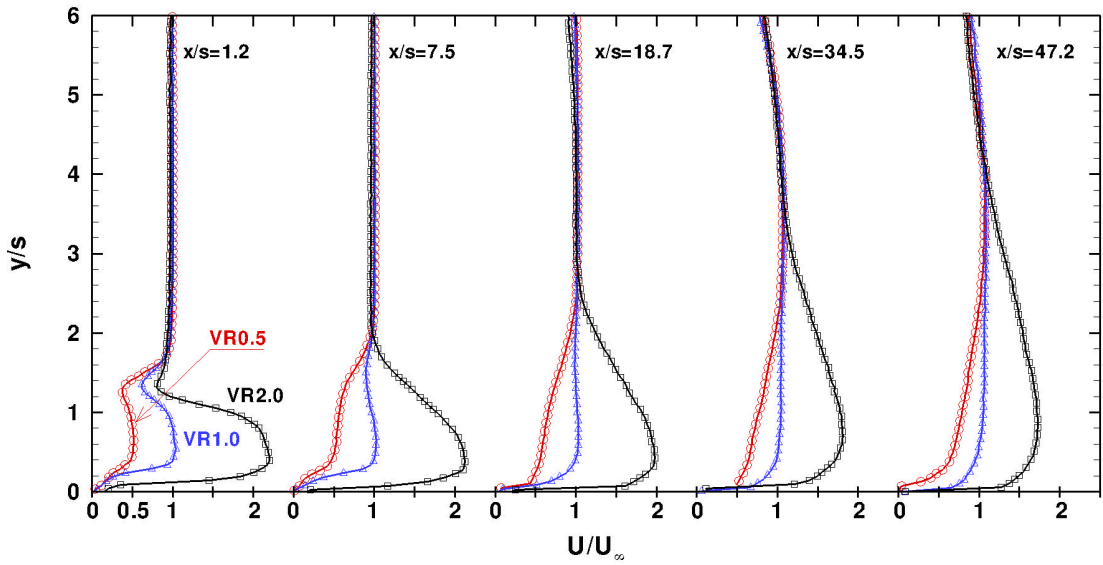


Figure 22. Experimental streamwise velocity profiles normalized by the freestream velocity, from PIV measurements at selected streamwise locations. -O-VR0.5, -Δ- VR 1.0, and - - VR2.0.

to a boundary layer flow by the fourth measurement location. This flow acceleration near the wall is the result of entrainment of the high momentum and temperature mainstream flow. This observation is consistent with the observation that the effectiveness is relatively good up to x/s of 20, but then drops significantly. The data in Figure 22 suggest that this is because the flow has transitioned to a boundary layer driven by the mainstream at $x/s \geq 20$.

Since the coolant and mainstream velocities are nearly identical for the boundary layer case (VR1.0), only in the small region behind the louver lip does the shear produce thermal mixing between the coolant and the mainstream. Mean velocity profiles indicate that the shear region is quickly dissipated, as the profile resembles that of a traditional boundary layer flow for x less than 20 slot heights downstream of the injection point. Therefore, in this region, the high temperature fluid in the outer layer of the boundary layer remains isolated from the wall and the flow provides a good film cooling effectiveness.

In the wall-jet case (VR2.0), the streamwise velocity profiles show large gradients at the wall and at the interface between the coolant and the mainstream. This interaction region grows in size as the maximum velocity of the wall-jet decreases due to mixing. This decrease in maximum velocity is particularly evident when comparing the profiles at the first and last locations.

Figure 23 shows the profiles of streamwise velocity RMS, U_{rms} . These profiles illustrate the main differences between the three flows. The initial shear for VR0.5 and VR1.0 produces high RMS levels that are dissipated rapidly, especially for VR1.0. VR0.5 and VR1.0 are mainly characterized by high levels of RMS near the wall, as

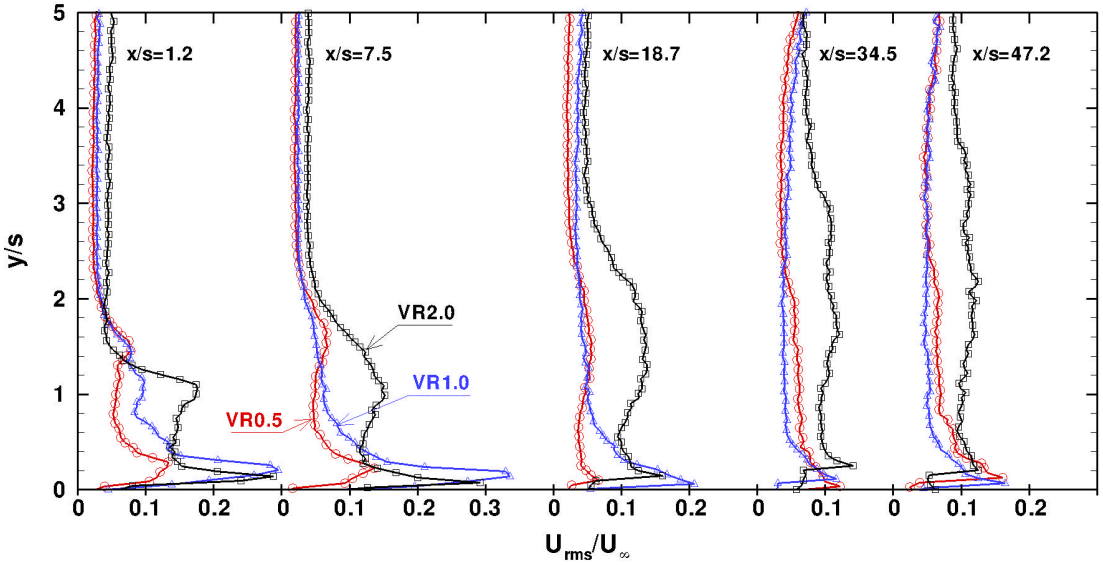


Figure 23. Streamwise velocity RMS normalized by the mainstream velocity; -O- VR0.5, - Δ - VR1.0, and - - VR2.0.

expected for turbulent wall-bounded flows. For the wall-jet case, however, the shear at the interface region remains large and spreads over a large region further downstream. This region of high RMS levels is consistent with the one identified in the temperature RMS data. This region is most often referred to as the outer mixing region, and it plays an important role in the maximum velocity decay. However, the near-wall region of the wall-jet, characterized by high levels of RMS, plays an equally crucial role in terms of mixing and transport.

Wall jet skin friction coefficient, C_f

Even though the current PIV measurements do not resolve the viscous sublayer, the wall-shear stress can be obtained from the wall-jet scaling theory. Several experimental and analytical studies have focused on wall jets in a configuration similar to that of the present study. Abramovich [66] conducted an analytical study of wall jets. One of the most remarkable studies is that of Kruka and Eskinazi [70], where similarity

variables supported by experimental data are found for the near-wall and mixing regions. Lauder and Rodi [71] presented an exhaustive review of the particular characteristics of the wall-jet. Even though these studies were conducted under isothermal flow conditions, they provide great insight into the present flow. The findings of these studies lead to the generalized diagram of the wall jet problem presented in Figure 24. The maximum velocity decays with the streamwise direction as a result of the spreading of the jet. In the near-wall region, self similarity is achieved when the velocity is normalized by the maximum velocity, U_m , and the wall-normal distance is normalized by the location of maximum velocity, d_m . In the outer layer, the flow scales with the maximum velocity deficit ΔU_m , and the difference between $d_{1/2}$ and d_m . These scaling variables have been verified in previous studies [70], [71], and [72]. The skin friction coefficient, C_f , can be determined from the velocity measurements using the self-similarity method based on scaling arguments developed by Mathieu [72], and Kruka and Eskinazi [70].

The important physical parameters to estimate the skin friction coefficient are the

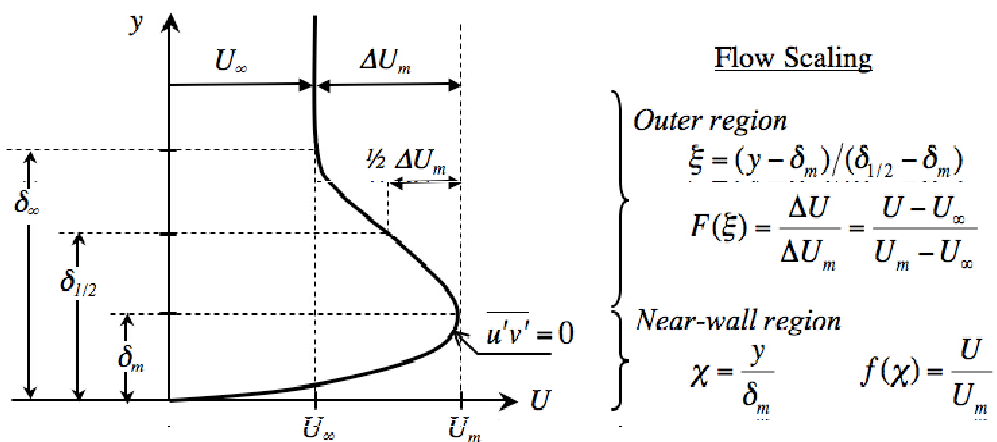


Figure 24. Wall-jet schematic with notations and similarity variables and function

wall-jet spreading rate and the maximum velocity decay. Figure 25-a shows the wall-jet spread quantified by the streamwise growth of d_m and $d_{1/2}$, which for both quantities is nearly linear starting at x/s of 8. Of importance to the C_f calculation is the growth of d_m , fitted by

$$d_m/s = ax/s + b, \quad (75)$$

where the slope for VR2.0 is $a = 0.013$ and the intercept $b = 0.2430$. This is illustrated in Figure 25-a. The slope is within 19% of the value of 0.0109 previously reported [70], which was obtained from a large number of experiments that had a significant scatter around the line.

The wall-jet spreading results in the decay of the maximum velocity, U_m , illustrated in Figure 25-b. The reduction in maximum velocity is followed by a similar decay in $U_{1/2}$, although the rate of decay is smaller. The presence of the wall and a

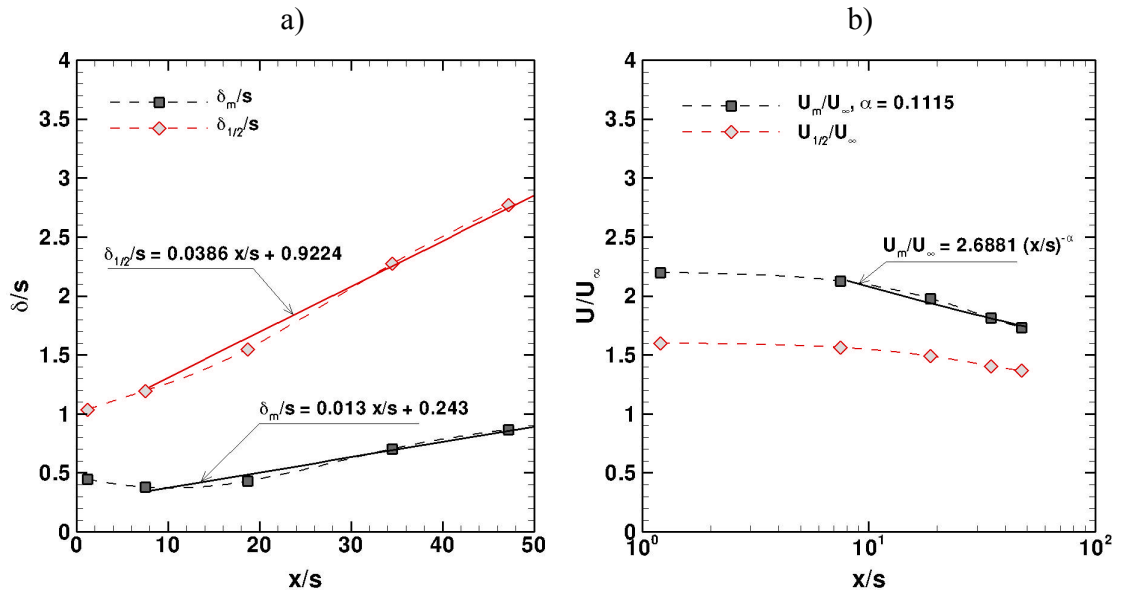


Figure 25. Effects of wall-jet spreading; a) linear growth of d_m and $d_{1/2}$, b) Characteristic velocity decay in the near-wall and mixing region

moving freestream suggest that the rate of decay should be different from that of an unconfined jet. For the present wall jet case, the decay of U_m is fitted using a power law,

$$\frac{U_m}{U_\infty} = c \left(\frac{x}{s} \right)^a \quad (76)$$

where the exponent a and the constant c are equal to 0.1115 and 2.6881, respectively. The exponent a varies significantly in the literature [70] where it is shown to depend on the inlet velocity ratio and other particularities of experimental setups.

In the near-wall region, the similarity variable c is defined by y/d_m and the similarity function $f(c)$ is given by U/U_m . From the similarity theory of the wall jet [70], the skin friction coefficient based on the local maximum velocity is given by:

$$C_{f,m} \equiv \frac{2t_w}{rU_m^2} = 2a[ay + (f - y)(1 - a)]. \quad (77)$$

In this expression, y and f are defined by

$$y = f(c_m) \int_0^{c_m} f(z) dz, \quad \text{and} \quad f = \int_0^{c_m} f^2(z) dz, \quad (78)$$

One should note that these integrals are constant along the streamwise direction if the flow is in the self-similar regime. Therefore, $C_{f,m}$ should be constant in this region since all the other terms are constants. Verification of this property is important since it validates the methodology.

The skin friction coefficient, $C_{f,m}$, is calculated from the PIV measurements using this methodology and plotted against the streamwise distance x/s in Figure 26-a. $C_{f,m}$ is shown to be nearly constant along the wall (0.0037-0.0039), in accordance with the similarity theory. The current data also lie within the range of experimental data from

Kruka and Eskinazi for a wall-jet with similar velocity ratio and Reynolds number. The present $C_{f,m}$ data are compared to the data of Kruka and Eskinazi in Figure 26-b, where the x -axis is the local Reynolds number based on U_m and d_m , $Re_m = U_m d_m / \eta$. The logarithmic scale emphasizes the fact that the current data are independent of Re_m in accordance with the similarity theory. The data of Kruka and Eskinazi show some dependence to this parameter as illustrated by the slope of the curve fit. Other early wall jet experiments show a similar behavior, although there is no consensus in the literature on the degree of variation of $C_{f,m}$ with the Reynolds number Re_m [70]. Insufficient near-wall resolution and contamination of the measurements by the hot-wire probe may explain this disagreement. The present data obtained from non-intrusive measurements do demonstrate the constancy of $C_{f,m}$. This comparison illustrates the quality of the PIV measurements and the applicability of the similarity theory in the near-wall region to obtain the skin friction coefficient.

Because $C_{f,m}$ uses a normalization of the wall shear stress based on the local maximum velocity, it can be difficult to relate to more global quantities. Thus, the wall shear stress is also normalized by freestream conditions to produce $C_{f,\infty}$ obtained from,

$$C_{f,\infty} = C_{f,m} \left(\frac{U_m}{U_\infty} \right)^2 \frac{r_c}{r_\infty}. \quad (79)$$

The profile of $C_{f,\infty}$ in Figure 26-a starts from high values near the slot injection and decreases to lower values further downstream. Since this parameter is directly proportional to the wall shear stress, the latter also follows the same streamwise evolution. This decrease in the wall-shear is due to the fact that the maximum velocity of the wall-jet is decreasing, thereby reducing the streamwise velocity gradients near the

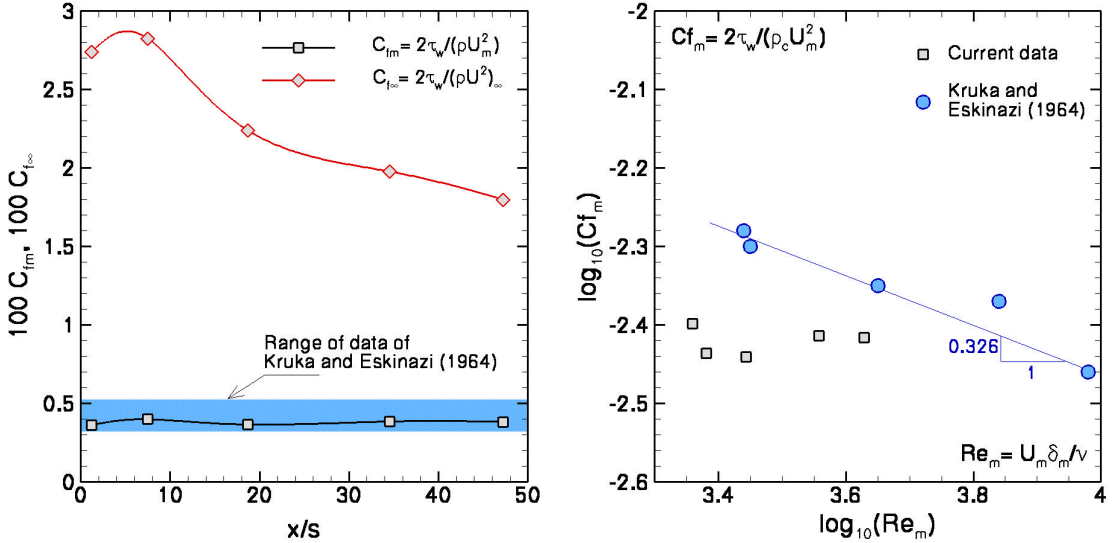


Figure 26. Friction coefficient for the wall-jet case VR2.0; a) C_f distribution along the wall, b) Comparison with data from Kruka and Eskinazi [70].

wall. Thus for wall jet, the near-wall transport is governed by the coolant flow near the injection point. Once the film starts mixing with the mainstream the near-wall transport is affected. This behavior is consistent with that of the Stanton number described in the heat transfer analysis.

3.4 Summary of Experimental Results

Detailed surface and flow measurements were obtained in a hot-wind tunnel facility specifically designed to study film-cooling flows. The three families of flows (wall-wake, boundary layer and wall-jet) displayed different behaviors and film cooling effectiveness. Backside cooled experiments resulted in a reduction of wall temperature when compared to the adiabatic wall temperature. For each case, the radiation heat flux was shown to be small compared to the conduction across the wall. The convective heat transfer coefficient, h , and the Stanton number were obtained from the convective heat flux data. When defined using the freestream conditions, the Stanton number emphasizes

the different heat transport properties of the three flows near the wall. They are strongly influenced by the initial slot coolant flow.

The thermal mixing of the flow was related to the adiabatic wall temperature and, when normalized by the inlet conditions, to the film cooling effectiveness. Case VR1.0 provided the best film effectiveness because of reduced thermal and momentum mixing. This was demonstrated by the flow velocity and temperature RMS measurements. It is apparent from the measurements that the initial shear between the film and the mainstream plays an important role in the mixing dynamics of the flows. The flow temperature profiles for adiabatic cases are shown to follow Wieghardt similarity expressions, thus validating its use in the derivation of film cooling effectiveness correlations.

For the wall jet case, the flow scaled successfully with the similarity variables. The skin friction coefficient showed good agreement with previous experimental data. The constancy of the skin friction coefficient based on the maximum velocity was very good, thus providing a validation of the similarity theory. However, this methodology cannot be applied to the boundary layer and wall-wake cases to obtain their skin friction coefficient. Therefore, the behavior of the skin friction in these cases will be explored in the numerical simulations.

Engineering correlations for the film cooling effectiveness showed poor performance overall. In the next chapter, we will try to use CFD modeling to predict the film cooling effectiveness and heat transfer at the wall.

Chapter 4: Evaluation the Spalart-Allmaras RANS Model

The objective of this chapter is to explore the performance of the Spalart-Allmaras RANS model in predicting the important quantities for the film-cooling problem. Since the film cooling effectiveness correlations showed poor agreement with experimental data, we propose here to evaluate the performance of the Spalart-Allmaras model [47]. Since experimental data show that the film remains attached to the wall, we believe that we can expect reasonable performance from this model [13].

Computational details for the domain and boundary conditions are presented first. Earlier, the Spalart-Allmaras model showed excellent agreement for the test case of Kasagi, a turbulent channel flow with heat transfer (cf. §2.3). However, it is necessary to further validate the model on the wall jet case (VR2.0) through a detailed comparison of simulation results with experimental data. Finally, computational results of interest for the film-cooling problem (i.e. effectiveness, wall heat flux) are compared to experimental data for all the cases, to provide a general overview of the performance of the model.

4.1 Computational Details

4.1.1 Computational domain and boundary conditions

The Navier-Stokes equations are normalized by a reference length (chosen as the slot height, s), velocity (bulk slot velocity, U_c) and temperature (coolant temperature, T_c). Therefore, the corresponding Reynolds and Prandtl numbers of the simulation are the slot Reynolds number, Re_s , and the Prandtl number at the coolant conditions. Both are computed using the experimental values reported in Table 6.

The extent of the computational domain is set to match the measurement domain for x/s in the range 0 to 50 and y/s from 0 to 7.3, as indicated by the schematic diagram of Figure 27. The boundary condition at the top boundary imposes zero normal gradients for the variables, thus representing the symmetry conditions expected at the center of the test section. An outflow convective boundary condition is applied at the outflow plane, $x/s = 50$. A no-slip boundary condition is imposed for the velocity components at the wall. The thermal boundary condition is zero temperature gradient for the adiabatic cases.

For the backside-cooled cases, the measured convective heat flux is not applied directly at the wall because it contains significant uncertainties, especially near the slot injection region. Furthermore, since the measurement uncertainty of the backside wall temperature, T_{wb} , is much smaller, this temperature is applied as a boundary condition at the backside wall. The wall temperature, T_w , is then solved at each time step so that there is continuity between the conduction heat flux into the wall and the gas-to-wall convection heat flux. Heat conduction in the solid is treated as one-dimensional in the

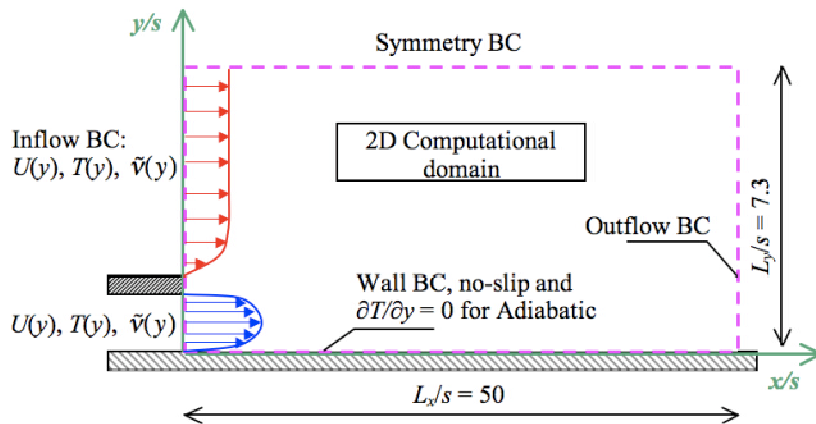


Figure 27. Computational domain for the RANS simulations with the Spalart-Allmaras model.

wall-normal direction. Considering that the conduction heat flux may be approximated by the its steady state expression, we write,

$$-\frac{k}{\Delta y_{cl}}(T_l - T_0) = -\frac{k_w}{t_w}(T_w - T_{wb}), \quad (80)$$

where k is the thermal conductivity of air, and t_w and k_w are the thickness and thermal conductivity of the UDEL plate. The temperatures and grid spacing are described in the schematic of Figure 28. Given that the wall temperature is obtained by linear interpolation between the first fluid point and the ghost cell, $T_w = (T_l + T_0)/2$, and inserting this relation into the heat flux continuity equation, we can solve for the ghost point temperature, T_0 ,

$$T_0 = \frac{(1-b)T_l + 2bT_{wb}}{(1+b)} \quad (81)$$

where the dimensionless constant b is defined by $b = (k_w \Delta y_{cl})/(2 k t_w)$. Therefore, the value of the ghost point is a function of the prescribed backside wall temperature and the calculated fluid temperature at the first grid point. This formulation is valid for any linear normalization of the temperature T . This simple boundary treatment removes the need to simulate the backside flow and the heat conduction inside the wall, thus considerably

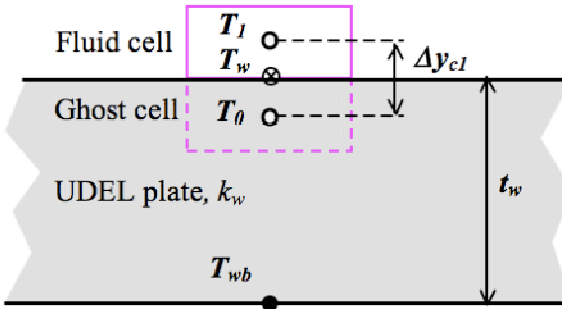


Figure 28. Schematic of the thermal boundary conditions for the backside cooled wall.

reducing the computational cost.

4.1.2 Methodology for the inflow conditions

The mean streamwise velocity and temperature profiles measured experimentally are prescribed at the inflow plane of the computational domain as detailed in Appendix B. The Spalart-Allmaras model solves a transport equation for the modified eddy-viscosity $\tilde{\eta}_t$, which is used to obtain the eddy-viscosity η_t . Consequently, caution must be taken for the boundary conditions of $\tilde{\eta}_t$. A Dirichlet boundary condition is applied at the wall, and a Neumann condition is applied at top boundary $y = L_y$ and the outflow plane. The value of the modified eddy-viscosity needs to be prescribed at the inflow plane to better describe the turbulence in this critical region. To do so, two precursor simulations are run: one for a turbulent channel flow corresponding to the slot exit conditions, and one for the mainstream boundary layer flow. For each of these simulations, the wall normal profile of modified eddy-viscosity is saved to a file. The two resulting profiles are combined into a single file that is read during the film cooling simulation to prescribe $\tilde{\eta}_t$ at the inflow plane (see Appendix B-3). The Spalart-Allmaras model also requires specification of a turbulent length scale, d , which represents the distance of a grid point from the nearest wall. For the film cooling simulation, this distance is the minimum between the distance to wall and the distance to the louver lip.

4.1.3 Grid details

The domain has 192 points in the streamwise direction and 79 points in the wall-normal direction. Only 4 points are used in the spanwise direction for these two-dimensional RANS simulations. This number is necessary for the QUICK scheme. The wall-resolution of the grid was excellent for all the cases, as illustrated in Figure 29. The

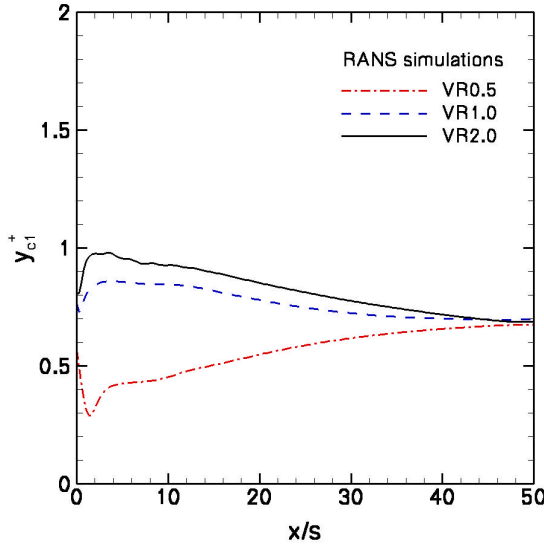


Figure 29. First cell center distance away from the wall in wall units.

first cell center distance from the wall, y_{cl} , is expressed in wall units ($y_{cl}U_t/\eta$) and plotted against the streamwise distance x/s . For all the cases this quantity is smaller than one wall unit along the entire wall, thus showing that the viscous sublayer is well resolved (note that the viscous sublayer extends from the wall to $y^+ = 5$).

4.2 Quantitative Validation for the Wall Jet Case

This section deals with the comparison of the RANS predictions with the experimental data of the wall jet case (VR2.0) to provide an assessment of the performance of the RANS model.

4.2.1 Wall temperatures

The adiabatic film cooling effectiveness is compared to the experimental data and to the correlation of Simon [8] in Figure 30-a. The reader is reminded that the film cooling effectiveness is a dimensionless form of the adiabatic wall temperature defined by

$$\hbar_{aw} = (T_\infty - T_{aw}) / (T_\infty - T_c). \quad (82)$$

The RANS results show excellent agreement with the experimental data even though the effectiveness is slightly overestimated far downstream. This indicates that the temperature mixing is well captured, except in the far field. With an overall deviation less than 2% from experimental data, the RANS simulation provides a better prediction of the effectiveness than the correlation of Simon [8]. It is quite remarkable that the Spalart-Allmaras model calculates accurately the effectiveness whereas most two-equation RANS models (i.e. $k-e$, $k-w$) have been shown to largely overpredict this quantity [17] [22]. Therefore, we can expect the Spalart-Allmaras mode to predict the thermal mixing equally well.

The distributions of wall temperatures for the non-adiabatic case are compared in Figure 30-b. The temperatures are normalized by the inlet conditions in the form of the effectiveness to allow comparison between the adiabatic and non-adiabatic cases. Therefore \hbar is equal to 1 at the coolant temperature and 0 at the freestream temperature. The backside wall temperature and coolant temperature are input conditions for the non-adiabatic simulations. The backside cooling results in an improved effectiveness when comparing adiabatic and non-adiabatic results. Although RANS correctly predicts the adiabatic wall effectiveness, it overpredicts the effectiveness in the backside-cooled case by nearly 6% of $(T_\infty - T_c)$ in the far field. While this deviation from measurements may seem large because of the normalization, it only represents a 3% underestimate of the absolute wall temperature. Near the injection point, the backside cooling reduces the wall temperature thereby increasing the effectiveness. This phenomenon appears to be slightly overpredicted in the simulation at this initial location. There is good confidence

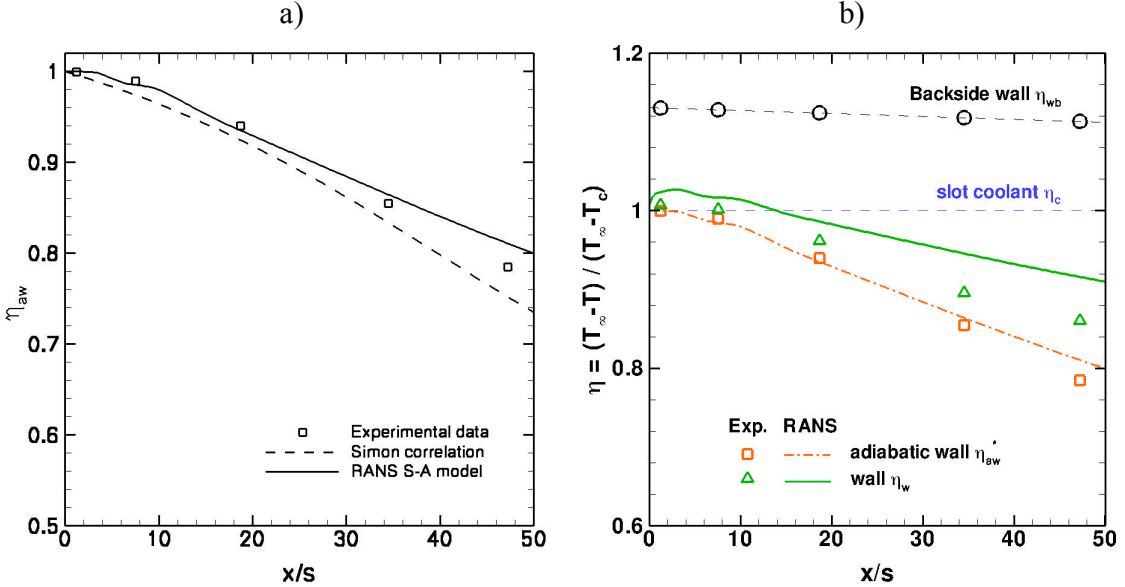


Figure 30. Comparison between predictions of wall temperatures by RANS for VR2.0; a) Adiabatic film cooling effectiveness for VR2.0AD, and b) dimensionless wall temperatures for VR2.0NA

in the value of the backside wall temperature prescribed as boundary condition in the simulation. However, the manufacturer of the UDEL plate does not specify the variation with temperature of the thermal conductivity of this material. Small errors in that property may result in wall temperature differences between the simulation results and the measurements. Obviously, the thermal conductivity of the plate does not play a role in the adiabatic case, thus explaining why the RANS results for η_{aw} compare better with the measurements. Consequently, the RANS also overpredicts the temperature difference ($T_{aw} - T_w$), an important quantity for the definition of the convective heat transfer coefficient of film cooling flows.

4.2.2 Heat transfer prediction

The absolute value of the convective heat flux, q_c , is compared to the experimental data in Figure 31-a. Given that the backside wall temperature is imposed, the heat flux can be calculated by the conduction across the wall or the convection on the

fluid side. Either method provides the same result within machine precision, since the viscous sublayer is resolved. In the experiment the convection is equal to the conduction across the solid minus the radiation loading from the hot casing to the wall. Even though the RANS underestimates the wall temperature in the near field, the convective heat flux is slightly overestimated. Further downstream the heat flux increases at a lower rate than the measurements, leading to a 10% underestimate of the heat flux in the far field.

For film cooling, the convective heat transfer coefficient, h , is defined by

$$h = |q_c| / (T_{aw} - T_w). \quad (83)$$

Therefore, S_{tc} , the Stanton number based on the coolant conditions, is equal to

$$S_{tc} \equiv \frac{h}{r_c C_{pc} U_c} = \frac{1}{Re_s Pr} \frac{(\partial q / \partial y_s)_w}{q_{aw} - q_w}, \quad (84)$$

where, the Reynolds and Prandtl numbers are those of the simulation, q is the dimensionless temperature in the simulation ($q = T/T_c$) and y_s is the dimensionless wall-normal distance y/s . Finally the Stanton number based on the freestream conditions, $S_{t\infty}$, is obtained by the relation $S_{t\infty} = S_{tc} m C_{pc} / C_{p\infty}$, where m is the blowing ratio and the ratio of specific heat is nearly unity in the current temperature range.

The comparison of $S_{t\infty}$ with experimental data in Figure 31-b shows significant discrepancies near the injection. These differences need to be put into perspective given the large errors bars in the experimental data. Further downstream the agreement is much better. The present RANS results underestimate the Stanton number mainly because of an underestimation of the temperature difference ($T_{aw} - T_w$). Nevertheless, the results capture the general decreasing trend of the measurements.

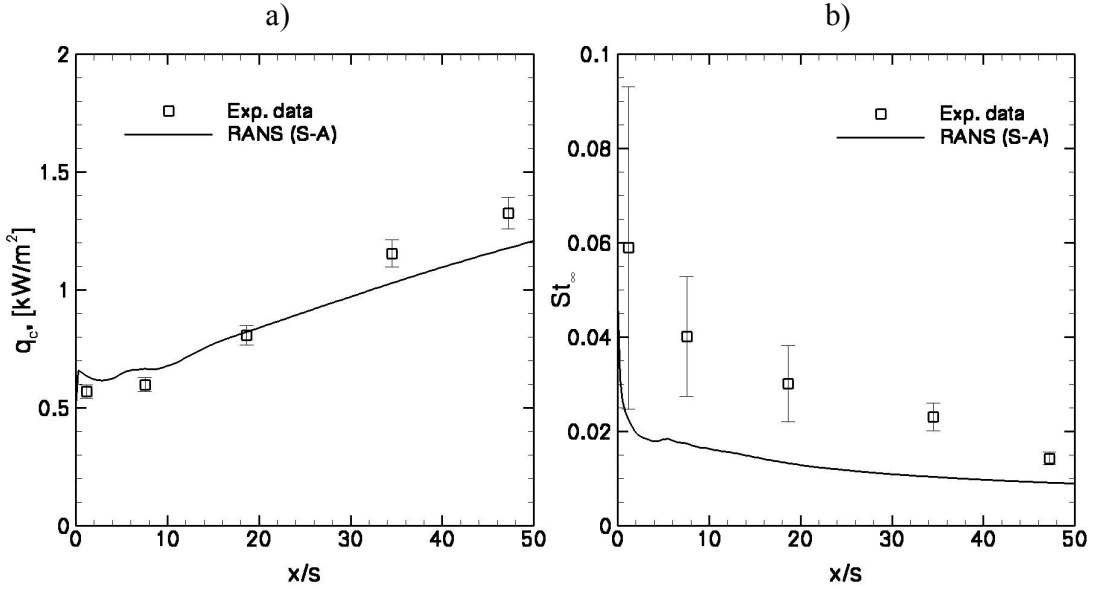


Figure 31. Heat transfer results for VR2.0NA; a) Convective heat flux, $|q_c|$, and b) Stanton number normalized by the freestream conditions, $S_{t_\infty} = h/(r U C_p)_\infty$

4.2.3 Assessment of the flow predictions

The streamwise velocity profiles normalized by the freestream velocity are compared to the PIV data of case VR2.0AD in Figure 32-a. The profiles are displayed at the streamwise locations corresponding to the measured temperature profiles.

Near the injection, at x/s of 1.2, the velocity profiles agree very well because the inlet experimental profile has been prescribed at the inflow. In the RANS, the initial shear behind the louver lip is not dissipated as fast as the measurements indicate. At the next location, the agreement is good, but the RANS results show a lower jet spreading and traces of the initial shear. Further downstream, the rate of decay of the maximum velocity is overestimated in the RANS but the location of the maximum velocity agrees well with the measurements. In the far field, the errors in the prediction of the peak velocity are noticeable. At x/s of 47.2 the maximum velocity is underpredicted by 22.8%

compared to the measured peak value. Numerical errors on mass conservation are not present since the incompressible flow solver used in this study strictly conserves mass within machine precision [25]. However, the incompressibility assumption (i.e. constant density equal to r_c) used in the simulation shows its limitations when the temperature of the high speed jet increases (i.e. density decreases). Using the measured temperature at the location of maximum velocity ($T = 348$ K) we can form the ratio of the coolant density to the local density, which is equal to 1.17. To first order the effect of variable density can account for 17% of the simulation error on the maximum velocity. The remaining error can be attributed modeling errors (Spalart-Allmaras model) and to imperfections in the experiment. A secondary flow was produced by entrainment of ambient air through a leaky window on the opposing wall. The measurements indicate that the freestream velocity is reduced for $y/s > 5$ at the last three profiles, consistent with the presence of a flow disturbance. This flow disturbance deflects the freestream and contributes to the acceleration of the maximum velocity beyond expected values.

In Figure 32-b, the flow temperature is normalized by the inflow temperatures in the form of the effectiveness, h , so that the value at the wall corresponds to the adiabatic film cooling effectiveness. The RANS results are compared to the measurements obtained with the micro-thermocouple probe. Overall, the shape and evolution of the temperature profiles are well predicted. The evolution of the interface between the hot stream ($h = 0$) and the coolant ($h = 1$) is also well captured, although the measurements indicate that the coolant penetrates further into the mainstream than what the RANS predicts. These differences become smaller far downstream.

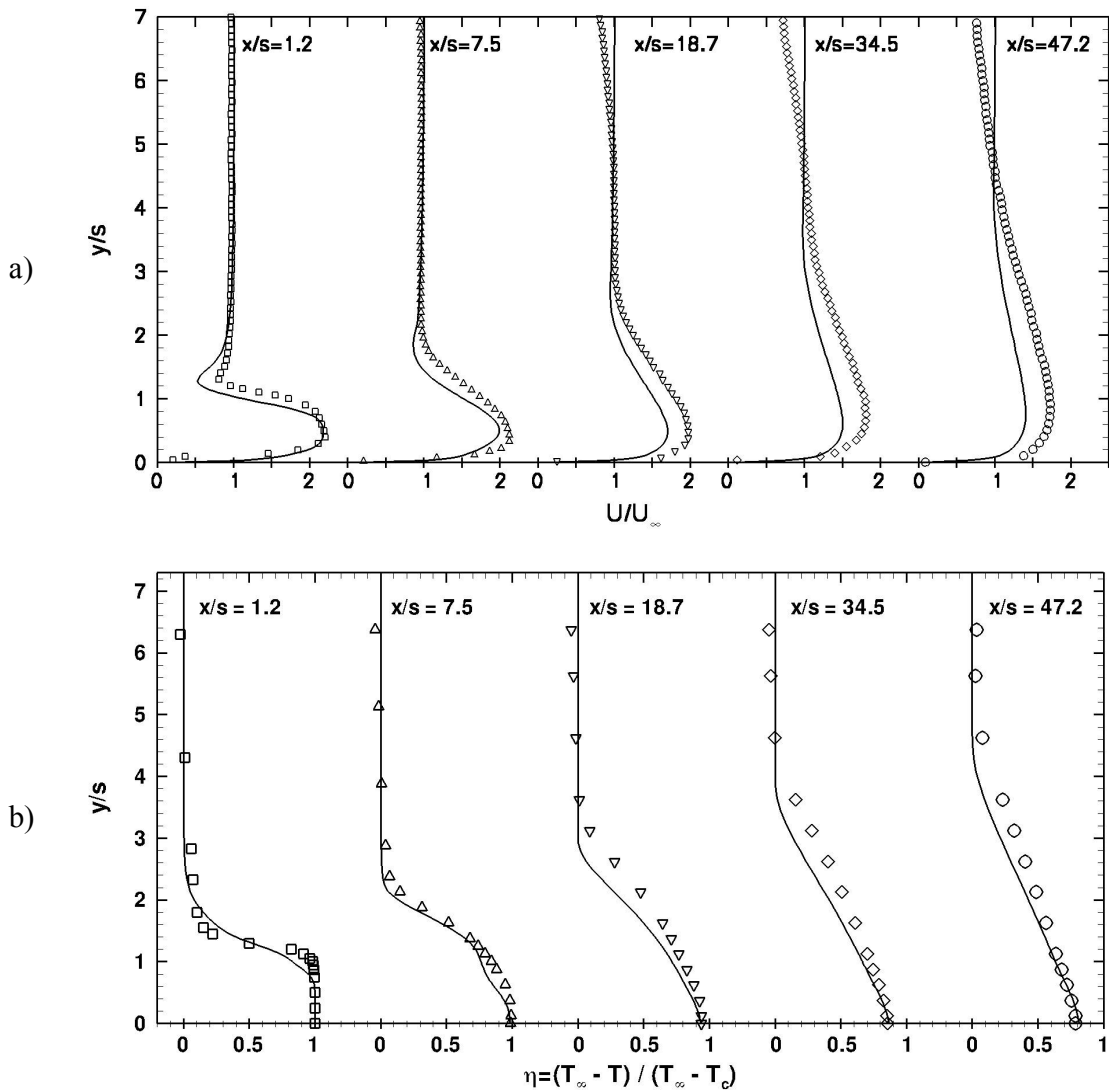


Figure 32. Velocity and temperature profiles for VR2.0AD; a) Normalized mean streamwise velocity, U/U_∞ , b) normalized temperature $\eta = (T_\infty - T) / (T_\infty - T_c)$. RANS results (lines), experimental data (symbols).

4.2.4 Skin friction coefficient

The skin friction coefficient, C_{fc} , is the wall shear stress normalized by the coolant kinetic energy, $C_{fc} \equiv 2t_w / (\tau_c U_c^2)$. Using the normalized simulation variables, $U_s = U/U_c$, and $y_s = y/s$, the skin friction coefficient C_{fc} can be written as:

$$C_{fc} = \frac{2}{\text{Re}_s} \left. \frac{\partial U_s}{\partial y_s} \right|_w . \quad (85)$$

Alternatively, we can define the skin friction coefficient as the wall shear stress normalized by the freestream kinetic energy, $C_{f\infty}$, which is then given by the relation

$$C_{f\infty} = C_{f,c} m VR, \quad (86)$$

where m is the blowing ratio and VR is the velocity ratio. The comparison of the predicted and measured C_{fc} is shown in Figure 33. The RANS results capture the general trend with an increase in wall shear stress after the point of injection followed by a slow decrease further downstream. Near the injection, the skin friction is overpredicted by nearly 30% when compared to the experimental data. However, the experimental skin friction was obtained using the similarity theory of Kruka and Eskinazy [70] despite the fact that the flow is not technically speaking self-similar in this region. The present measurements compared well

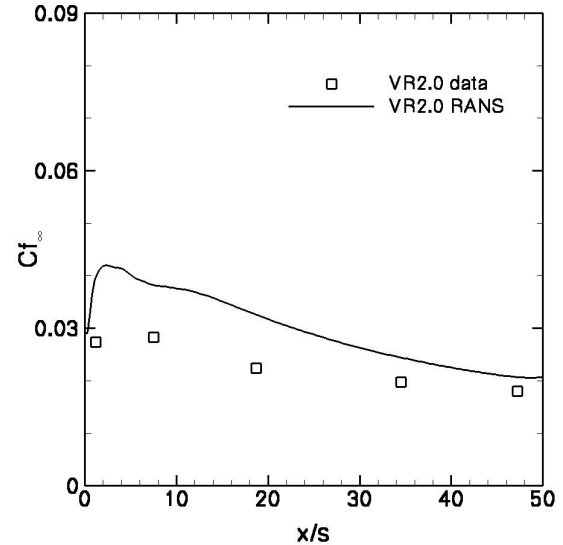


Figure 33. Skin friction coefficient for the wall jet case VR2.0, $C_{f\infty} = 2t_w / (\tau_c U_c^2)$.

with previous data, but the uncertainty on the measure is difficult to quantify. Nevertheless, the RANS results compare better further downstream and capture the trends indicated by the measurements. The underpredicted maximum velocity certainly influences the value of the predicted wall-shear stress, but to a lower extent since the error on the skin friction coefficient is about 10% in the far field.

4.2.5 Summary of the validation

The adiabatic effectiveness obtained with the Spalart-Allmaras RANS model is in excellent agreement with the measurements. The near-wall temperature mixing is well captured as evidenced by the temperature and velocity profiles. The heat transfer results for the non-adiabatic case show reasonable agreement for the heat flux but the Stanton number is largely underpredicted. Although the skin friction is overpredicted near the injection, better agreement is reached further downstream.

4.3 Wall-Wake and Boundary Layer Cases

The objective of this section is to briefly provide an assessment of the performance of the RANS Spalart-Allmaras model in predicting the mixing and heat transfer quantities for the other cases (VR0.5 and VR1.0).

4.3.1 Film cooling effectiveness

The film cooling effectiveness is compared to experimental data and to the correlation of Lefebvre [1] for VR0.5 and VR1.0 in Figure 34. In Chapter 3, we have discussed the fact that the present adiabatic wall temperature measurements for VR0.5AD are not available but that the data from Case 2 in [12] are applicable since they were obtained at similar inlet conditions ($VR = 0.46$, $m = 0.76$, $Re_s = 1790$). Therefore, the RANS results for VR0.5AD are compared to the experimental data of [12] and the

Lefebvre correlation [1] in Figure 34-a. The simulation results are in good agreement the experimental data, thus indicating that the mixing is well captured by the Spalart-Allmaras model. The mixing appears to be overpredicted in the far field. This discrepancy could be a result of the higher Reynolds number in the simulation (i.e. 2652 versus 1790 in the experiment). Overall the comparison is satisfactory with a deviation from measurements of less than 5%. Furthermore, the RANS results provide an improved estimation of the effectiveness when compared to the correlation of Lefebvre.

For the boundary layer case (VR1.0), the RANS results are in good agreement with the present experimental data, as illustrated in Figure 34-b. The Spalart-Allmaras model produces less mixing for this case, thus overestimating the effectiveness by 3%, a value comparable to what was seen for the wall jet case. Finally, Lefebvre correlation underestimates the effectiveness by nearly 15% in the far field. This correlation

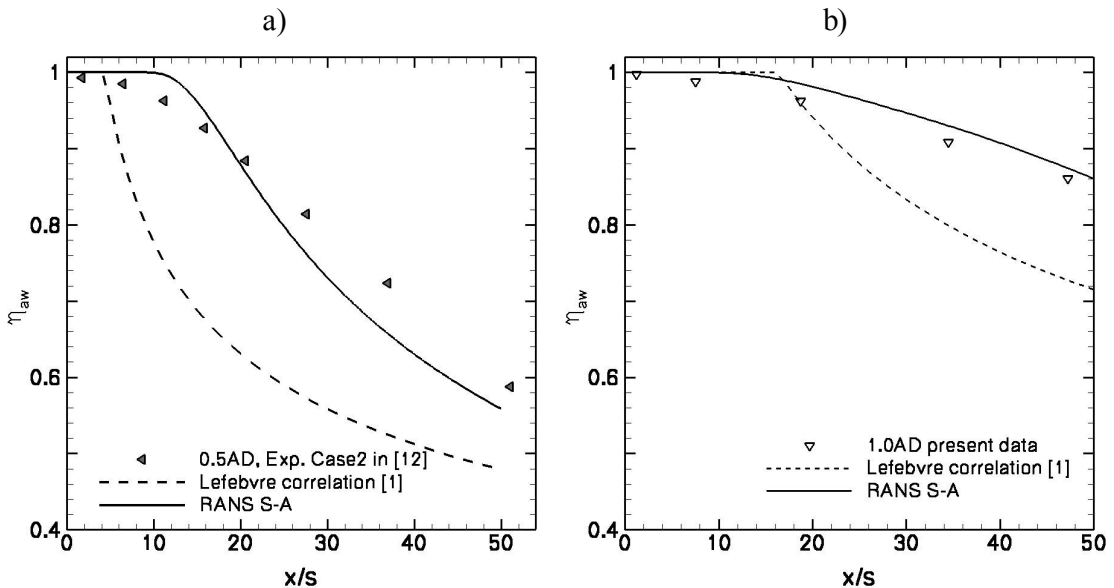


Figure 34. Adiabatic film cooling effectiveness; a) case VR0.5AD, b) case VR1.0AD. Experimental data (symbols), RANS (line), correlation (---) [1].

overpredicts the initial mixing of the film as indicated by the large slope of decay of effectiveness. This behavior has been pointed out in a previous study using a large set of experimental data [12]. The Spalart-Allmaras model performed well for the three different flows considered in this study and could be used to provide a better estimation of the film cooling effectiveness when compared to Lefebvre correlation.

4.3.2 Wall heat flux and shear stress

The convective heat flux and the Stanton number, $S_{t\infty}$, are compared to the experimental data in Figure 35. For the boundary layer case (VR1.0), the heat flux is in good agreement with the experimental data. The heat flux increases slowly with the streamwise distance but remains small compared to the wall-wake case. This is consistent with the fact that the film mixing is the least strong for the boundary layer case. The hot gases from the mainstream remain isolated from the wall. On the contrary, the wall-wake case presents strong mixing resulting in high temperature fluid being transported to the wall, thus generating a strong increase in the heat flux at the wall. At x/s of 10, a steep increase in heat transfer is noticed in the RANS results and confirmed by the experimental data. This increase in wall heat flux can be related to the sharp increase in the adiabatic wall temperature observed at the same location. This suggests that the film is being mixed with hot freestream, which results in an increase of heat transfer. In the limiting case of a backward facing step (e.g. $VR = 0$), the point of reattachment occurs at about 7 step heights downstream. At this point there is an increase in heat transfer due to the downwash effect of the impingement mentioned by Keating et al. [26]. Although the present flow configuration is different similar phenomena produce the increase in wall heat flux observed at x/s of 10.

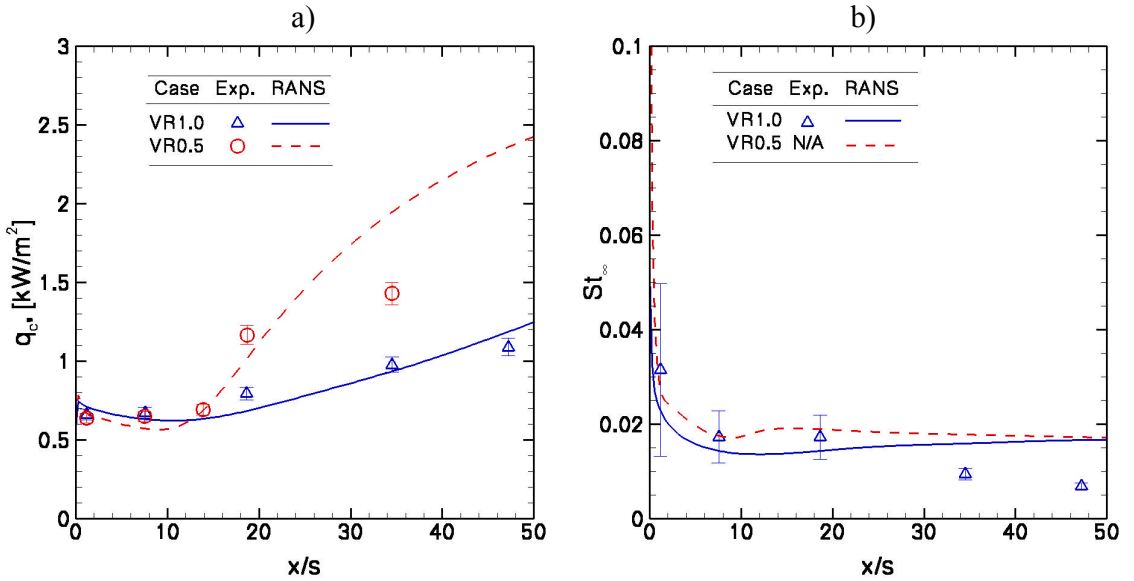


Figure 35. Heat transfer for VR0.5 and VR1.0; a) Convective heat flux, b) Stanton number based on freestream conditions

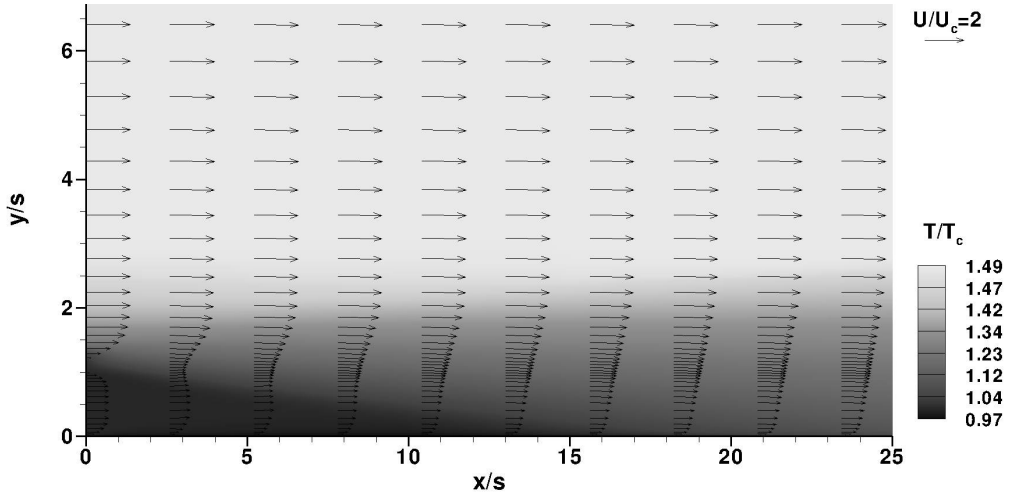


Figure 36. Downwash effect for the wall-wake case.

The Stanton number, $S_{t\infty}$, plotted in Figure 35-b) also presents a noticeable increase 10 slots downstream of the injection plane, thus confirming that the downwash effect of the freestream results in an increase in heat flux and convective heat transfer coefficient. This effect on the Stanton number is reduced further downstream. The downwash effect can be visualized in Figure 36, where the mean velocity vectors are

superimposed on top of the contour of the normalized flow temperature, T/T_c . High temperature fluid is transported from the freestream to the wall, as evidenced 10 slots downstream of the injection

Interestingly, the heat flux and Stanton number for the boundary layer case do not display a similar behavior because the film and the freestream have nearly the same velocity. Furthermore, the Stanton numbers for VR0.5 and VR1.0 achieve the same value far downstream, thus indicating that both flows are governed by the freestream. The Stanton number for VR1.0 matches the experimental data up to x/s of 20, but is largely overpredicted further downstream.

The streamwise profiles of the skin friction coefficient, C_f^∞ , are presented for all the cases in Figure 37. The wall jet and the boundary layer display similar wall shear stress behaviors. Downstream of the injection the shear stress increases then slowly decreases further downstream. In the case of the wall-wake flow (VR0.5), the wall shear

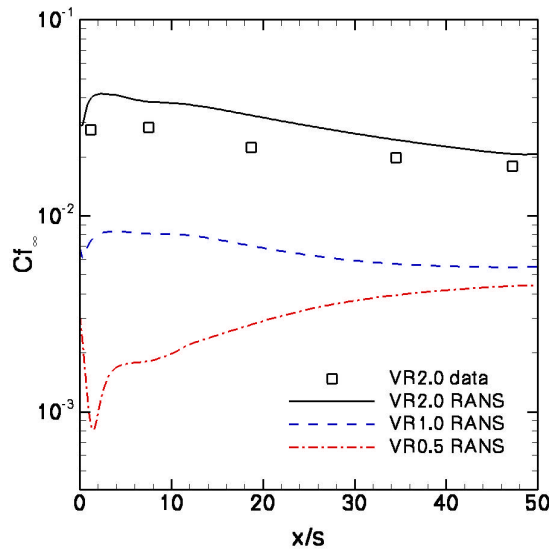


Figure 37. Skin friction coefficient for all the cases.

stress decreases downstream of the injection plane, suggesting that the flow is adapting to the shear induced by the inflow velocity profile. A noticeable slope increase is observed at $x/s \approx 10$, corresponding to the Stanton number and heat flux increase. Far downstream the skin friction coefficients tend to converge to a constant value of 0.0042 and 0.0055, for VR0.5 and VR1.0 respectively. This far field behavior is also consistent with the Stanton number. Both the Stanton number and the skin friction indicate that the flow transport properties at the wall are mainly governed by the freestream far downstream.

4.3 Summary: Performance of the Spalart-Allmaras Model

In general, the RANS results obtained with the Spalart-Allmaras model compare favorably with the present experimental data. Although significant deviations from the measurements are noticed in the far field, the proposed backside boundary condition for the non-adiabatic wall cases provides a reasonable estimate of the heat flux and wall temperatures. This method could be improved to include multi-dimensional solid conduction using a well-characterized thermal conductivity of the UDEL plate. A simpler method would be to directly prescribe the wall temperature as boundary condition. In this case, the wall temperature needs to be measured with high spatial resolution (e.g. infrared thermography) and accuracy to capture the important physics of the flow.

Overall, the streamwise velocity profiles compared well with the PIV measurements. However, the peak velocity of the wall jet was significantly underestimated in the far field. The constant density assumption used in the incompressible solver shows its limits in this region of the flow where the film temperature increases. Leakage through the top window during the PIV measurements

could also explain the reduced decay in maximum velocity observed experimentally. Additionally, modeling errors introduced by the RANS model could also affect the comparison with experimental data. Nevertheless, the flow temperature profiles were in good agreement with the measurements, thus providing confidence that the thermal mixing is well captured through the use of the turbulent Prandtl number assumption for modeling the eddy-diffusivity (cf. Chapter 2).

Most importantly, the film cooling effectiveness is calculated with good accuracy, thereby proving that the Spalart-Allmaras model could be a viable improved alternative to using semi-empirical correlations. However this model would be limited in the presence of large-scale freestream turbulence that would interact with the film. In this case, more sophisticated unsteady RANS models or large-eddy simulation models must be used.

Chapter 5: Large-Eddy Simulation of Wall Jet Film Cooling

The two-dimensional turbulent wall jet in a moving stream presents characteristics common to turbulent wall-bounded flows near the wall and mixing layers in the outer mixing region. The complexity of the flow is materialized by the two-layer scaling, which has been verified in various experimental studies ([70], [71]), LES [23], and DNS [24]. The present experimental data and RANS results have shown that the wall jet configuration provides stronger mixing than the boundary layer case even though both flows have nearly the same slot Reynolds number. Experimental data also suggest that the strong mixing in the wall jet case is a consequence of higher shear between the film and the mainstream. At the interface between the two streams, the large-scale structures grow with the streamwise location and interact closer to the wall, thus transporting pockets of high temperature fluid near the wall. This mechanism, identified experimentally, causes the mixing of the film and the reduction in film cooling effectiveness. We propose in this chapter to further study this mechanism by analyzing large-eddy simulation results for the wall jet case VR2.0 under adiabatic wall conditions.

5.1 LES Computational Details

Similarly to the RANS simulations, the Navier-Stokes equations are normalized by the reference length, s , the reference velocity, U_c , and the reference temperature, T_c . Consequently, the Reynolds number of simulation is $Re_s = 5466.11$ and the Prandtl number is $Pr = 0.7082$, taken from the experimental conditions for case VR2.0AD reported in Table 6.

5.1.1 Computational domain and boundary conditions

The computational domain for the large-eddy simulation is similar to the one for the RANS simulations, except that it extends in the spanwise direction to capture the three-dimensional turbulent structures. The computational domain is set to match the measurement range in the streamwise direction. Consequently it extends for x/s in the range 0 to 50, and y/s from 0 to 7.3, as indicated by the schematic of Figure 38. The length of the domain in the spanwise direction is πs with periodic boundary conditions at both ends to model an infinitely wide channel. The symmetry boundary condition at the top boundary ($y/s = 7.3$) imposes zero normal gradients for all the variables, thus representing the symmetrical conditions expected at the center of the test section. At the outflow plane (i.e. $x/s = 50$), an outflow convective boundary condition is applied for the streamwise velocity and the transported passive scalar, i.e. temperature. At the wall a no-slip boundary condition is imposed for the three velocity components. Since for the case

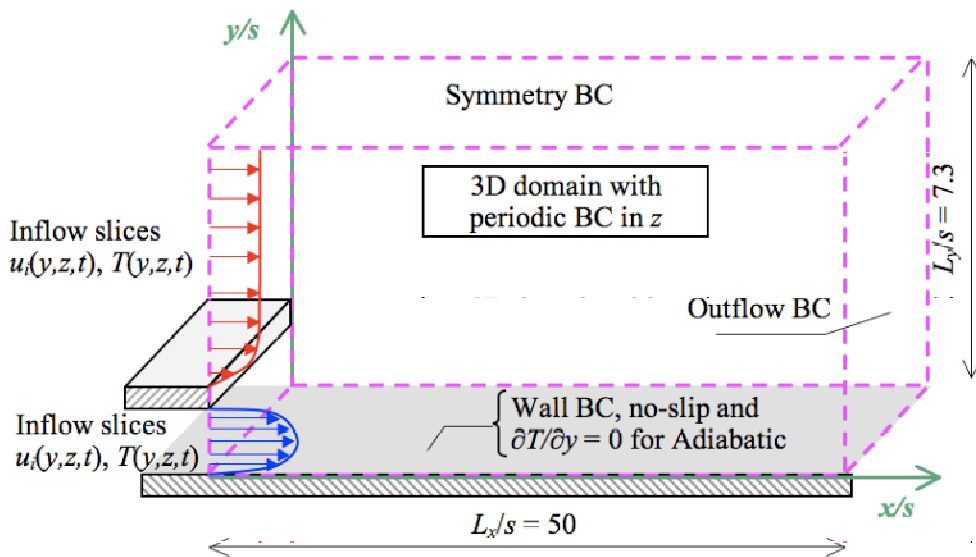


Figure 38. Computational domain for the large-eddy simulation

VR2.0AD the wall is adiabatic a Neumann condition (zero temperature gradient) is applied at the wall.

Setting the inflow conditions for LES is a challenging task as emphasized in Chapter 2. The flow prescribed at the inflow plane must display the temporal and spatial information of the resolved turbulent flow structures, as illustrated in Figure 38.

5.1.2 LES inflow from precursor simulations

In the present work, the inflow velocity and temperature are read from a database containing temporal slices in the y - z plane of the flows corresponding to the coolant slot exit and the mainstream boundary layer. The database is obtained from precursor large-eddy simulations for both of these flows.

Slot coolant flow

At the exit of the slot, the flow can be accurately represented by a two-dimensional fully developed turbulent channel flow. Therefore, this flow is computed in a three-dimensional LES of the channel flow at the Reynolds number $Re_s = 5466.11$ with periodic boundary conditions in the spanwise and streamwise directions. In this precursor simulation, the streamwise periodic condition is equivalent to having the computational domain traveling downstream with the mean flow as the flow develops. The flow in the computation is initiated with random noise added to a bulk velocity and temperature initial field. It takes several flow-through times for coherent turbulent eddies to develop. The computation is stopped once the steady state regime is reached (i.e. mean statistics are invariant with time). Diagnostics are performed to validate the grid spacing for wall-resolved LES, and then the computation is restarted to save y - z slices of data at each time step at a given x -location (middle of channel in this work). The slices

contain the instantaneous flow field (u , v , w) and the instantaneous temperature at a given time step.

Mainstream flow

Computing the developing boundary layer in the freestream with LES requires more computational resources and complex inflow methods. In this work a simplified approach was taken. It is based on the fact (supported by the present measurements) that most of the turbulence in the freestream boundary layer is contained near the wall. The PIV measurements provide the boundary layer mean profile, from which we can extract the boundary layer thickness, d , and the momentum thickness, q . Based on the PIV data we obtain $d/s = 0.79$ and $q/s = 0.087$.

The Reynolds number based on the momentum thickness, $Re_q = U_\infty q/\nu$, is an important quantity used to characterize turbulent boundary layers. Based on the measurements $Re_q = 239$ for the mainstream flow at the inlet plane. Therefore, this quantity was matched in a channel flow simulation by adjusting the Reynolds number, Re_d , which was found from RANS simulations to be 2240. Finally, a large-eddy simulation of a channel flow at $Re_d = 2240$ (d is the half channel height) was computed to produce the inflow for the mainstream. The results of this simulation were saved to slices at the same frequency (in physical time units) as for the slot precursor LES.

Combining the slices

In the final step of the inflow plane generation, the slices for the two streams are combined into a single slice, where a region of zero velocity behind the louver lip is added for $y/s = 1$ to 1.19. Furthermore, the mainstream flow receives extra work since the precursor simulation was performed over a channel flow and that only the bottom

boundary layer is of interest. The velocity and temperature fluctuations are extracted from the instantaneous data and rescaled according to the length and velocity scales used in the film cooling LES (the same as in the slot flow precursor). Furthermore the rescaled fluctuations are filtered to remove the turbulence in the upper boundary layer. These fluctuations are then added to the mean velocity and temperature profiles obtained experimentally at the mainstream inlet plane.

Finally the resulting combined slice is written to a database that is read directly by the subroutine that sets the inflow plane conditions. This method implemented by Keating [25] performs an interpolation in space (grid) and time (between slices) at each time step of the film cooling simulation. Recycling is used once the last slice in the database has been read. In the present work, the database contains 5000 combined slices. This number was deemed sufficient because it corresponds to more than one flow-through time in the actual film cooling simulation, thus reducing unwanted periodicity effects introduced in the computation due to the recycling method.

5.1.3 Grid details

The grid is uniform in the streamwise and spanwise direction and contains 256 and 64 points, respectively. In the wall-normal direction the grid is non-uniform and contains 128 points. The grid spacing is refined to resolve the viscous sublayer at the wall and the shear region behind the louver lip at the interface between the mainstream and the coolant wall jet. The corresponding RANS simulation was used to determine the correct grid spacing in wall units, $\Delta x_i^+ = \Delta x_i U_t / n$, where U_t is the friction velocity. For the present computation the viscous sublayer was well resolved since the center of the first cell point away from the wall was between 0.3 and 0.46 wall units. The grid also

provided a good resolution of the streamwise structures with $30 \leq Dx^+ \leq 60$, and the spanwise structures with $7.5 \leq Dz^+ \leq 15$ along the wall. The grid spacing in wall units corresponds to the recommended values for wall-resolved LES [59], although the grid spacing in the streamwise direction could be reduced near the injection to enforce $Dx^+ \leq 50$ for the entire domain.

5.1.4 Post-processing and statistics

After 3 flow-through times, the flow reaches a steady state for the mean quantities. Of particular interest for film cooling, this regime is also indicated when the adiabatic wall temperature reaches a steady state. The computation is restarted to save samples every $0.5 t_s$, where t_s is the characteristic simulation time scale defined by $t_s = s/U_c$. Sampled over nearly two flow-through times, the 115 samples are used to calculate the statistics of the flow. Because the flow is homogenous in the spanwise direction, two-dimensional statistics are obtained by ensemble averaging over the homogeneous spanwise direction and by time averaging over the samples.

5.2 Large-Eddy Simulation Results

5.2.1 Film cooling effectiveness and mixing

The film cooling effectiveness, h_{aw} , obtained from the present LES is presented in Figure 39. The LES results are compared to the measurements and to the results obtained with the Spalart-Allmaras RANS model. Both computations compare favorably with the experimental data. However, it appears that the LES predicts more mixing (i.e. lesser effectiveness) than what the measurements indicate. The analysis of the RANS velocity profiles indicated the limitations of the constant density assumption, when compared to

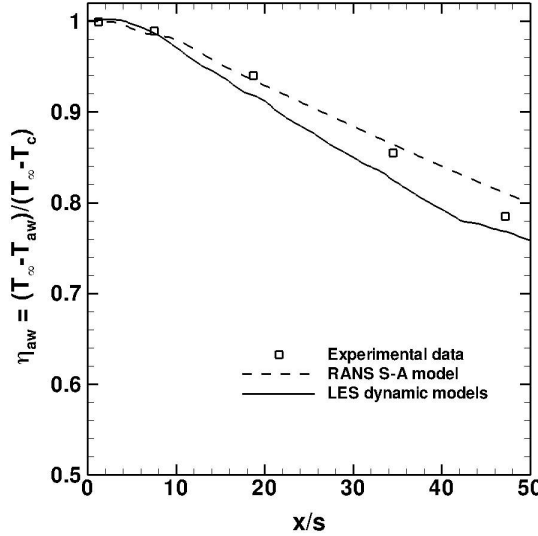


Figure 39. Film cooling effectiveness, LES, RANS and measurements

the present experiments. Similar limitations are also expected in the LES, and will be explored in the next section. However, the present LES provides valuable information on the turbulent transport of a passive scalar in the case of a wall jet in a moving stream.

The decay of film cooling effectiveness is a direct consequence of the interaction of large-scale structures between the coolant flow and the hot mainstream. LES provides the opportunity to visualize the mixing of the film since the grid resolves the large scales of motion. Figure 40-a shows the contour of instantaneous streamwise velocity at the center of the domain in the spanwise direction (i.e. $z/s = \pi/2$). The high-speed streaks exiting the slot coolant flow are represented by white colors, whereas darker colors represent lower velocities. Ejection events are clearly visible at locations where high velocity fluid penetrates into the mainstream flow. The opposite reaction (i.e. sweeping of low speed fluid into the jet) is also observed. This mixing interaction between the two streams contributes to the velocity mixing and the decay of the jet maximum velocity,

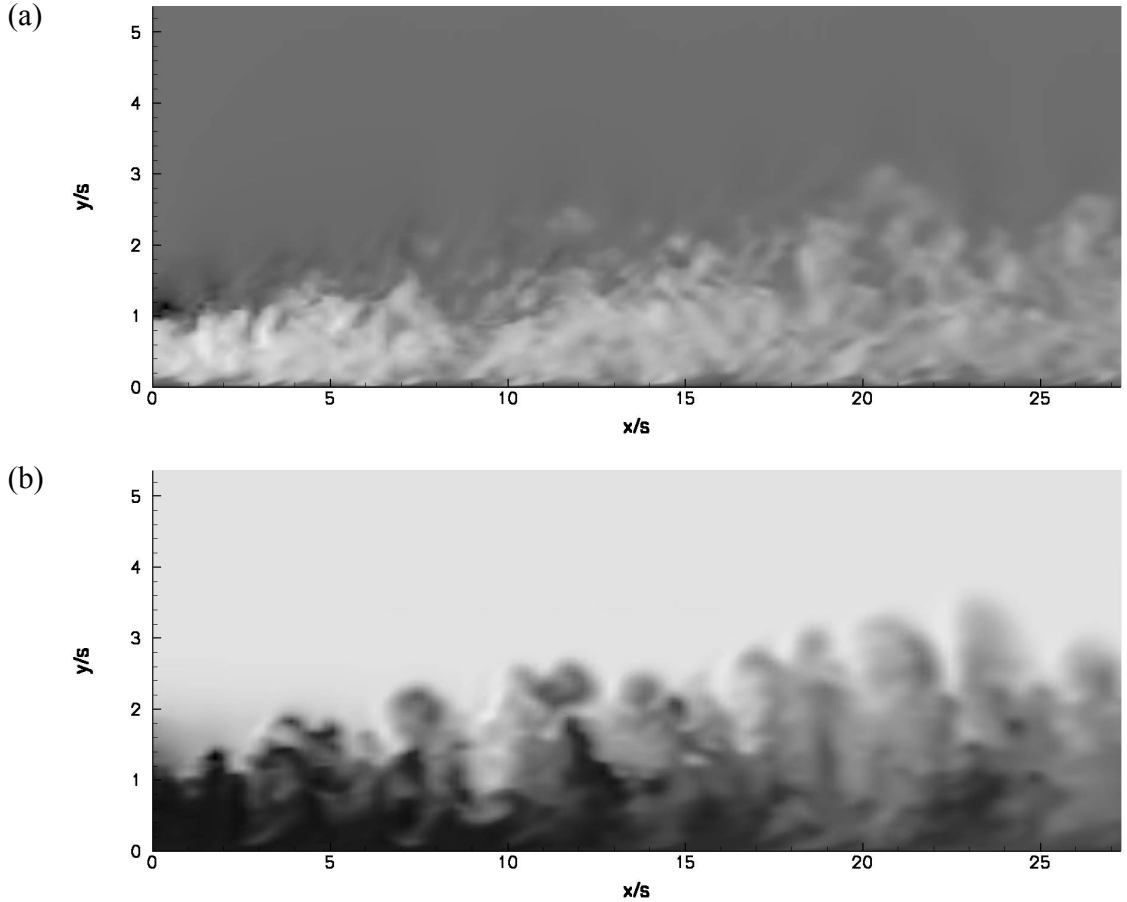


Figure 40. Instantaneous contours of streamwise velocity (a), and temperature (b). White color indicates high velocity and high temperature regions

evidenced by the darker colors associated with the lower velocity of the jet far downstream.

Similar patterns are found in the temperature mixing, assumed to be a passive scalar in the computation. The contours of instantaneous temperature in the same z -plane are presented in Figure 40-b. A similar convention is adopted, with light colors representing high temperature fluid and vice-versa. Pockets of low temperature fluid are ejected into the hot mainstream due to the transport properties of the turbulent scales. Reciprocally, high temperature fluid is also entrained (swept) towards the wall. These

large-scale structures lead to intense scalar mixing, as evidenced by the lighter colors of the film far downstream. Sweeping and ejection events for the temperature contours correspond to similar event in terms of velocity, thus emphasizing the scalar transport is induced by the flow velocity structures. A significant sweeping event is clearly visible for both the velocity and the temperature at $x/s = 9$. Before analyzing more in detail the turbulent fluxes and Reynolds stresses, we propose first to examine the mean flow statistics.

5.2.2 Mean flow statistics

The profiles of mean streamwise velocity normalized by the freestream velocity are presented in Figure 41-a. In the near field, the LES results are in good agreement with the present PIV measurements for the wall jet case VR2.0AD. However, further downstream the maximum velocity is underpredicted. This effect was pointed out in Chapter 4, and is due in part to the limitations of the constant density assumption used in the code. The other source of error comes from the measurements, where leakage through the window on the opposing wall produced entrainment of ambient air. This flow disturbance at the top wall is believed to have accelerated the maximum velocity of the jet. Despite these discrepancies, the simulated temperature profiles normalized in the form of the effectiveness show good agreement with the measurements in Figure 41-b.

In previous investigations of turbulent wall jets [74], a logarithmic overlap region has been found although it was shown to be in a limited region [23]. Figure 42 shows the mean streamwise velocity profiles scaled in wall units, $U^+ = \bar{U}/U_t$, plotted against the wall-normal distance in wall units, $y^+ = yU_t/\eta$. The velocity profiles show good agreement in the viscous sublayer with the linear relation. The profiles show some

overlap with the logarithmic inertial relation of Osterlund [73], especially far downstream. Ahlman et al. [24] noticed limited overlap in the logarithmic region with this relation (only up to $y^+ = 13$), but explained that this may be due to the low Reynolds number of the flow ($Re_s = 2000$) in their DNS. The inner scaling overlap in the present study extends to a larger region but is limited above $y^+ = 60$. The location of maximum velocity, d_m , is located within the range $y^+ = 133$ to 205 at the 5 streamwise locations considered in this study, as reported in Table 7.

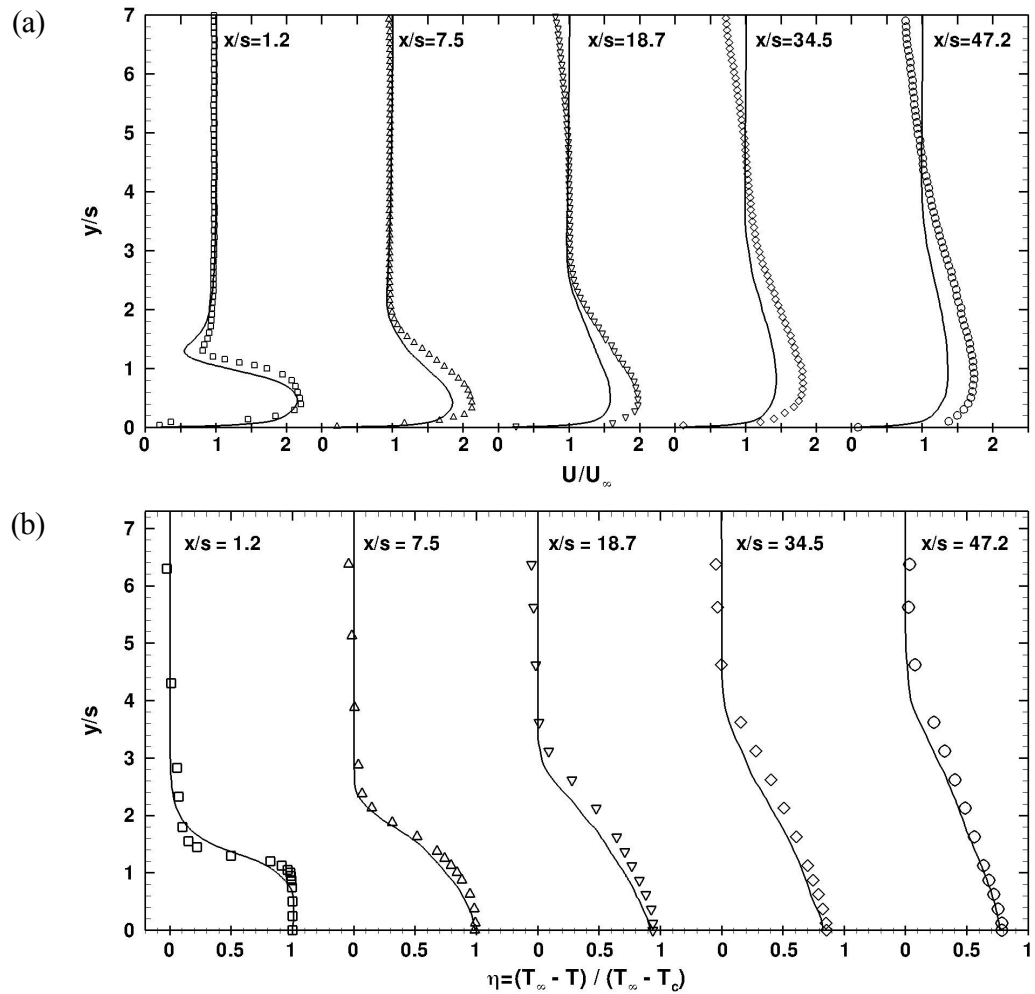


Figure 41. Mean profiles streamwise velocity (a) and temperature (b) compared to the present measurements.

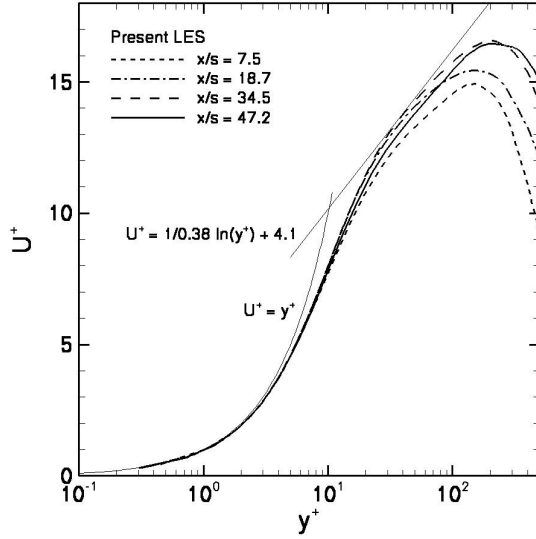


Figure 42. Profiles of mean velocity in wall units, comparison to the law of the wall of [73].

Table 7. Location of maximum velocity normalized by the slot height and in wall units, d_m/s and d_m^+ .

x/s	1.2	7.5	18.7	34.5	47.2
d_m/s	0.431	0.431	0.503	0.827	0.874
d_m^+	133.3	151.2	145.3	203.0	205.0

The skin friction coefficient, C_{fc} , defined as the wall shear stress normalized by the coolant kinetic energy, $C_{fc} = 2t_w/(r_c U_c^2)$, is compared to the present measurements in Figure 43-a. Similarly to the RANS results poor agreement is found with the measurements, which could be explained by the effects of variable density on the near-wall transport and by the measurement uncertainties to estimate the skin friction. Far downstream, the computation overestimates the skin friction by nearly 15%. However the computed friction velocity, U_t , normalized by the maximum velocity at the exit of the

slot, $U_{c,max}$, is in good agreement with the DNS data of Ahlman et al.[24], as indicated in Figure 43-b. The fact that the friction velocity is larger in far field could be attributed to the lower Reynolds number in the DNS (2000 versus 5466 in the present LES). It is important to point out that the LES and DNS data presented in Figure 43-b do not correspond to the exact same flow conditions and that the comparison remains therefore qualitative.

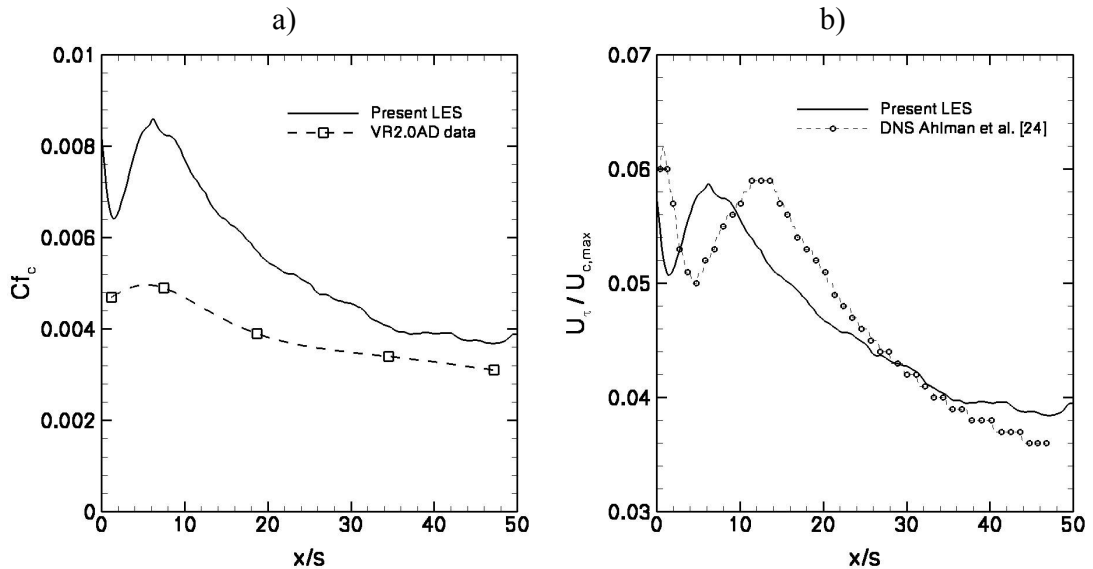


Figure 43. Skin friction coefficient (a) and friction velocity compared to the DNS of [24] (b).

5.2.3 Higher order statistics

Velocity field

To further study the turbulent mixing characteristics of the velocity field we examine the resolved fluctuation intensities (root-mean square) expressed in wall units, i.e. normalized by the friction velocity, as pictured in Figure 44. The profiles of

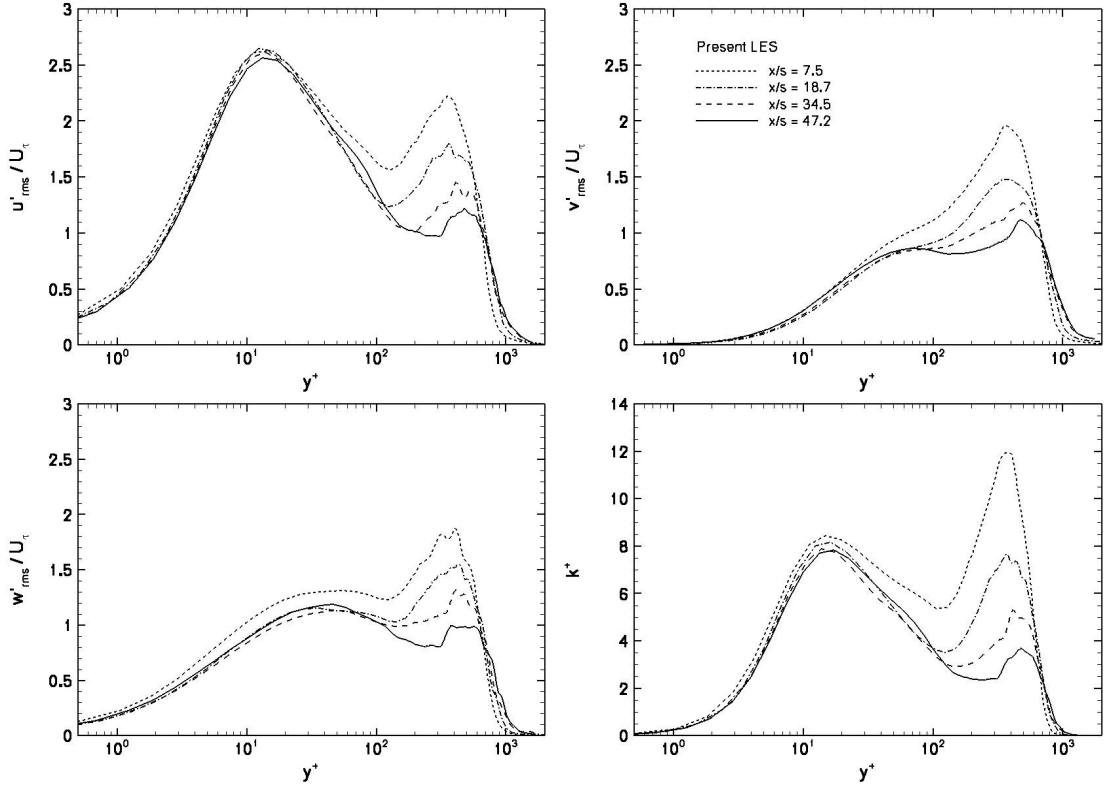


Figure 44. Grid resolved normal Reynolds stresses and their contribution to the turbulent kinetic energy.

streamwise fluctuation intensity present a double peak: a first peak between the wall and the location of maximum velocity, d_m^+ , and a second peak above d_m^+ in the outer mixing region. This finding is consistent with the LES of Dejoan et al. [23] and the DNS of Ahlman et al. [24]. The value of the inner peak is similar at several downstream locations, thus illustrating that the inner part of the flow can be appropriately scaled in wall units. The outer peak for the streamwise intensity is reduced with the streamwise distance. This effect, not as pronounced in [24] ($VR = 10$), is due to low external shear in the present simulation (i.e. $VR \approx 2.0$) and more importantly to the fact that the inner scaling does not collapse the outer layer data.

The wall-normal and spanwise fluctuation intensities present a single peak in the outer mixing region (near $y^+ = 400$). The anisotropic nature of the mixing is significantly influenced by the presence of the wall, as evidenced by the stronger streamwise fluctuations in the inner region when compared to the other two components. In the inner region, the spanwise fluctuation intensities increase then present a narrow plateau rather than a peak, a behavior consistent with [24]. The turbulent kinetic energy, k , for an incompressible flow is normalized in wall units by the relation

$$k^+ = k / \left(\frac{1}{2} U_t^2 \right) = \overline{u_i'^2} / \left(U_t^2 \right). \quad (87)$$

In Figure 44 the turbulent kinetic energy displays peaks in the inner and the outer layer. The inner layer peak occurs for y^+ between 13 and 14 at the various streamwise locations considered. This result compares well with channel flow results [32], and the wall jet DNS results of Ahlman [24]. The second peak in outer layer (above the maximum velocity) reduces with streamwise distance, suggesting that the production of turbulent kinetic energy decreases due to a reduction in the mean shear mechanism as the two streams mix. This effect is visible in a previous DNS [24] ($VR = 10$) but not as pronounced in the present LES since the velocity ratio is five times smaller. In between the two peaks of turbulent kinetic energy, minima are observed and correspond very well with the locations of maximum velocity (zero shear). All these elements point to the fact that the mean shear contributes largely to the levels of turbulent kinetic energy.

The resolved Reynolds shear stress, $\overline{u'v'}$, normalized in wall units by the friction velocity, U_t , is presented in Figure 45. Similar to turbulent wall bounded flows, the streamwise and wall-normal fluctuations are negatively correlated in the inner layer. When a given point in the flow sees a positive v' , on average, this event is associated with

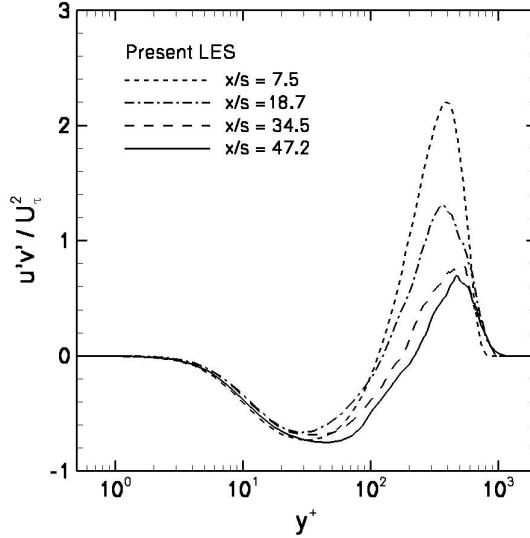


Figure 45. Resolved Reynolds shear stress in wall units

a negative u' . This mechanism is characteristic of the ejection and sweeping events [32].

Further away from the wall, the Reynolds shear stress increases towards large positive values in the outer layer. The peak in the outer layer decreases with the streamwise distance. An important feature of the wall jet flow is that the location of zero turbulent shear stress does not exactly coincide with the zero mean shear point (i.e. d_m), but is located closer to the wall in the inner layer.

Temperature field

The profiles of temperature RMS normalized by the local difference between the freestream and the adiabatic wall temperature are presented in Figure 46. Inner scaling is not possible because of the adiabatic wall condition (zero-gradient) therefore the results do not collapse in the inner layer. The temperature RMS in that region is small and increases further in the outer layer. The location of maximum temperature RMS is above the location of maximum shear stress. At the two last streamwise locations, the peak

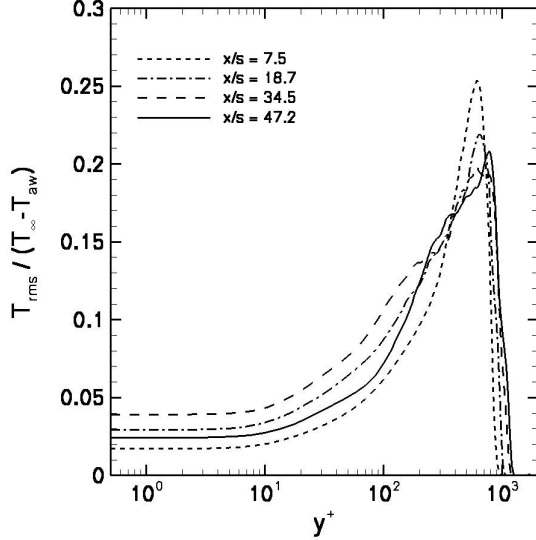


Figure 46. Temperature RMS normalized by the local temperature difference ($T_{\infty} - T_{aw}$)

RMS value indicates some degree of scaling around 0.20, which is in good agreement with the reported value of 0.18 [24].

Figure 47 shows the profiles of resolved turbulent heat fluxes in the streamwise and wall-normal direction, $\overline{u'T'}$ and $\overline{v'T'}$, normalized by the friction velocity and the local temperature scale ($T_{\infty} - T_{aw}$). Both the streamwise and the wall-normal fluxes are zero at the wall. In the inner layer, the fluctuations of temperature and streamwise velocity are positively correlated, thus indicating that when u' is positive, T' is also positive (local temperature increase). This event is due to the local transport of hot fluid towards the wall because when $v' < 0$, $u' > 0$ (recalling that $\overline{u'v'}$ is negatively correlated in this region). In the outer layer, u' and T' are negatively correlated due to positive correlation between u' and v' in this region (cf. Figure 45). The wall-normal turbulent fluxes are always negative illustrating that a positive v' is associated with a negative T' , and vice-versa. In other words, an ejection event is always associated with the transport of a pocket of fluid cooler than the local mean temperature. These valuable temperature

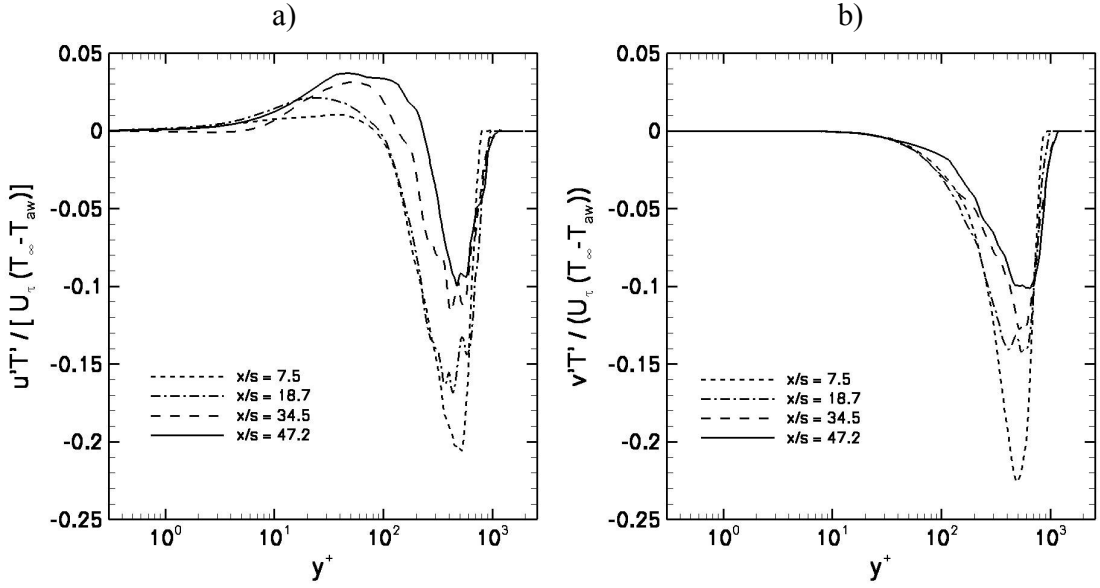


Figure 47. Turbulent streamwise (a) and wall-normal (b) heat fluxes

and velocity statistics confirm the observations obtained from the instantaneous contours of u and T , which showed the interaction between ejection and sweeping events.

5.3 Summary of the Main LES Results

A large-eddy simulation of a wall jet flow ($Re_s = 5466$ and $VR \approx 2.0$) with transport of a passive scalar was performed in this study. The temperature is treated as a passive scalar, which was found to be an inaccurate assumption when comparing the measurements to the simulation results. The variable density of the flow in the experiment leads to acceleration of the wall jet near the wall, a phenomenon that could not be captured by the current constant density solver. However, the LES results for the effectiveness and the flow temperature are in very good agreement with the measurements.

The current results were carefully analyzed to verify known physical properties associated with wall jets. For instance, the skin friction compares favorably with DNS data taken from the literature. The logarithmic overlap region was found to be limited to a narrow region in wall units, as pointed out in previous studies. This effect could also result from the low Reynolds number of the flow. More importantly, the present computation provides detailed velocity and scalar mixing statistics that quantify the main mechanisms responsible for the reduction of the jet velocity and the mixing of the coolant flow temperature. The velocity statistics show a first peak of turbulent kinetic energy inside the inner layer for y^+ in the range 13 to 14, and a second peak in the outer layer. The flow in the inner layer is strongly anisotropic because the streamwise fluctuation intensity is much larger than the other components. The Reynolds shear stress is negative in the inner layer then increases towards positive values in the outer layer, changing sign before the location of maximum velocity. The streamwise and wall-normal turbulent heat fluxes are negative in the outer layer and of comparable magnitude. These turbulent statistics provide valuable information about the complex flow mixing mechanisms that cannot be obtained from measurements. Finally, the RANS models could be challenged by the strong anisotropy of the flow in the inner layer.

Chapter 6: Conclusions

This study presents an experimental and numerical investigation of turbulent slot film cooling flows. Three coolant-to-mainstream velocity ratios were considered in this work: a wall jet, a boundary layer flow and a wall-wake flow. For each flow, measurements were taken for an adiabatic wall and a backside cooled wall configuration. Comprehensive flow and surface measurements were carried out under realistic hot flow conditions. The mean and RMS temperature profiles were obtained with a fast response micro-thermocouple probe. The mean and RMS velocities were measured using PIV under hot flow conditions. This study provides guidance for seeding the flow and a general methodology to carry out challenging near-wall measurements using the PIV technique. The comprehensive experimental database obtained in this study provides valuable detailed information on the turbulent mixing of the flow that can be used to explore the performance of and validate the turbulence models used in CFD.

Numerical simulations were performed using the Spalart-Allmaras RANS model for all the experimental cases. Aside from its relative simplicity, this model has the advantage of well predicting attached turbulent wall bounded flows. Its performance is explored by comparing the results to the present measurements. To further explore the mixing characteristics, a wall resolved large-eddy simulation of the wall jet with scalar transport was performed. This work also provides details on a methodology to prescribe the LES inflow plane conditions by using precursor simulations of the coolant and the mainstream. This approach makes use of physical scaling arguments to prescribe the

fluctuations in the mainstream flow. The LES results are compared to the present measurements and published DNS data. This highly resolved LES provides valuable information and physical insight into the mixing mechanisms responsible for the decay in film cooling effectiveness. The following sections highlight the principal aspects of this study and the noteworthy observations and contributions to the field therein.

Experimental Results

- Adiabatic experiments show that the boundary layer case provides the minimum shear and the best film cooling effectiveness, followed by the wall jet. The wall-wake case initially provides a good effectiveness that rapidly decreases due to the mixing of the film. Engineering correlations for the film cooling effectiveness showed overall poor agreement with the measurements in the near field considered in this study ($0 \leq x/s \leq 50$).
- Velocity and temperature statistics indicate that the mixing is strongly influenced by the mean shear in the flow. In the wall jet case the length scale associated with the thermal mixing is larger than that of the boundary layer case, therefore the wall jet mixing mechanisms interact closer to the wall. Mean temperature profiles demonstrated the appropriate outer layer scaling of Wieghardt. Therefore, these results justify the use of Wieghardt similarity profile in the derivation of the film cooling effectiveness correlations regardless of the inlet flow type for $x/s > 18$.
- In the backside-cooled cases, the wall-wake flow displays a strong increase in wall heat flux, corresponding to the location of strong decrease in effectiveness. The convective heat transfer coefficient obtained from the measurements contains large

uncertainties near the injection because of the small difference (T_{aw} - T_w). However, the Stanton number results indicate that the heat transport at the wall is initially governed by the coolant flow but tends to be governed by the freestream kinematics further downstream as the film mixes.

- The skin friction coefficient for the wall jet flow was obtained using a similarity approach described in previous studies. The constancy of the skin friction coefficient, C_{fm} , was observed in accordance with theory and previous studies.

Numerical Simulations

- The Spalart-Allmaras RANS model preformed quite well in predicting the film cooling effectiveness and the heat flux. This suggests that the Spalart-Allmaras model could be used as an alternative to semi-empirical correlations in this region. The temperature profiles are also in good agreement with the measurements.
- However, the maximum velocity of the wall jet was significantly underpredicted in the far field. This discrepancy is attributed to two contributing factors. First, the passive scalar assumption (constant density solver) shows its limitations in the temperature range of the experiments. Secondly, the entrainment through the top window in the experiments created a flow disturbance that contributed to the acceleration of the flow.
- To the author's knowledge, the present study presents the first LES with passive scalar transport performed for the wall jet case. Despite the limiting assumption of a constant density when comparing to the present measurements, this highly resolved

LES with the dynamic subgrid scale models provides fundamental insight into the turbulent transport mechanisms.

- The velocity statistics were examined and showed two peaks of turbulent kinetic energy: a first peak located in the inner layer ($y^+ = 13-14$), and a second peak in the outer layer. The streamwise fluctuation intensity is much larger than the other components in the inner layer, thus revealing the anisotropic nature of the flow in this region. The Reynolds shear stress is positive in the inner layer then changes sign right before the location of maximum velocity in accordance with previous studies.
- The streamwise and wall-normal turbulent heat fluxes are negative and of comparable magnitude in the outer layer. These detailed statistics help quantify the turbulent transport mechanism driving the scalar mixing, which was visualized through the instantaneous contours of velocity and temperature.

Future Work

- Although great effort has been taken to provide detailed measurements, the near-wall resolution in the PIV measurements could be improved by considering a smaller field of view to attempt resolving the viscous sublayer. The leakage through the top window should also be resolved in subsequent experimental campaigns, as the associated flow disturbance can lead to undesirable measurement uncertainties.
- In order to be able to fully compare experimental measurements and simulation results the present flow solver should be adapted to variable mass density.

- The present LES results are valuable to understand passive scalar transport. Validation against DNS data and examination of the budgets of turbulent kinetic energy would greatly contribute to improving the current understanding of the flow.

Appendix A. Experimental and Numerical Details

A1. Micro-Thermocouple Signal Compensation

Here we recall the heat balance on the thermocouple bead

$$m_b C_{p,b} \frac{dT_b}{dt} = h_{conv} A_b (T_g - T_b) \quad (\text{A.1})$$

where T_b , m_b , A_b , and C_{pb} , are the temperature, mass, surface area and specific heat of the bead, h_{conv} is the convective heat transfer coefficient and T_g is the gas temperature. The time constant of the transient heat balance on the bead is noted, τ_b , and defined by

$$\tau_b = \frac{m_b C_{p,b}}{h_{conv} A_b} \quad (\text{A.2})$$

Then solving for the actual gas temperature in the heat balance equation leads to

$$T_g = T_b + \tau_b \frac{dT_b}{dt}. \quad (\text{A.3})$$

The time constant was used to correct for the thermal inertia of the probe, and recover the power of the fluctuations at high frequencies with a digital compensation technique. The measurement of the time constant was performed in the test section during actual test conditions. Thus the gas temperature is simply related to the measured bead temperature. However, the derivative term dT_b/dt becomes contaminated if electronic noise if central differencing is applied to measured signal T_b . To avoid this phenomenon the derivative is applied in Fourier space and filtering operation is applied.

To avoid Gibbs phenomenon when applying the fast Fourier transform (FFT) to a non-periodic discrete signal, we define the periodic signal P

$$P(t) = T_b(t) - R(t) \quad (\text{A.4})$$

where $R(t)$ is the line joining the first ($t = 0$) and last data point in the measurement sample. Using this decomposition of the raw signal, and substituting into Eq. (A.3), one obtains the following expression for the gas temperature.

$$T_g = P + t \frac{dP}{dt} + R + t \frac{dR}{dt}. \quad (\text{A.5})$$

The two last terms on the right hand side of this equation are known analytic functions: R is a line and its time derivative is a constant. The first and second terms are determined from measurements and consequently have embedded electronic noise. To minimize electronic noise these two terms are treated in Fourier space resulting in

$$\mathcal{F}(P + t \frac{dP}{dt}) = (1 + jtw) \mathcal{F}(P), \quad (\text{A.6})$$

where \mathcal{F} is the Fourier transform operator, $w = 2\pi f$ is the angular frequency, and j is the complex number defined by $j^2 = -1$. After the transform the derivative of the signal is easily determined from the complex product in frequency space. A low-pass filter \mathcal{L}_{fc} with frequency cut-off f_c (defined by a signal-to-noise ratio of 5:1 across the entire frequency range) is then applied along with the inverse Fourier transform yielding the actual filtered gas temperature signal,

$$T_g = \mathcal{F}^{-1} [\mathcal{L}_{fc}((1 + jtw) \mathcal{F}(P))] + R + t \frac{dR}{dt} \quad (\text{A.7})$$

A2. Experimental Uncertainty Analysis

Given a physical quantity, Q , as function of directly measured variables w_i ,

$$Q = Q(w_1, w_2, \dots, w_n) \quad (\text{A.8})$$

the uncertainty on a quantity Q , ΔQ , is calculated based on the uncertainties for each measured variables

$$\Delta Q = \sqrt{\left(\frac{\partial Q}{\partial w_1} \Delta w_1\right)^2 + \left(\frac{\partial Q}{\partial w_2} \Delta w_2\right)^2 + \dots + \left(\frac{\partial Q}{\partial w_n} \Delta w_n\right)^2} \quad (\text{A.9})$$

In this section, we derive the expression for the uncertainty of each quantity.

Blowing ratio, m

The blowing ratio is ratio of mass flux per unit area between the coolant and the mainstream. It is defined by $m = (r_c U_c) / (r_\infty U_\infty)$. For incompressible flow, using the ideal gas law and neglecting the small gas composition differences due to vitiation the blowing ratio can be rewritten as:

$$m = (T_\infty U_c) / (T_c U_\infty) \quad (\text{A.10})$$

The absolute uncertainty on the blowing ratio is then given by:

$$\Delta m = \left[\left(\frac{U_c}{U_\infty T_c} \Delta T_\infty \right)^2 + \left(\frac{T_\infty U_c}{U_\infty T_c^2} \Delta T_c \right)^2 + \left(\frac{T_\infty}{T_c U_\infty} \Delta U_c \right)^2 + \left(\frac{T_\infty U_c}{T_c U_\infty^2} \Delta U_\infty \right)^2 \right]^{1/2} \quad (\text{A.11})$$

The relative uncertainty is obtained by dividing the previous expression by the blowing ratio m ,

$$\frac{\Delta m}{m} = \sqrt{\left(\frac{\Delta T_\infty}{T_\infty} \right)^2 + \left(\frac{\Delta T_c}{T_c} \right)^2 + \left(\frac{\Delta U_c}{U_c} \right)^2 + \left(\frac{\Delta U_\infty}{U_\infty} \right)^2} \quad (\text{A.12})$$

Consequently the relative uncertainty on the blowing ratio is directly related to the relative uncertainty on the measured inflow velocities and temperatures.

Slot Reynolds number, Re_s

The slot Reynolds number is defined by the bulk slot exit velocity, the slot height and the kinematic viscosity at the temperature of the coolant, $Re_s = U_c s / \eta(T_c)$. The relative uncertainty on Re_s is then found to be

$$\frac{\Delta Re_s}{Re_s} = \sqrt{\left(\frac{\Delta s}{s}\right)^2 + \left(\frac{\Delta U_c}{U_c}\right)^2 + \left(\frac{1}{\eta(T_c)} \frac{\partial \eta}{\partial T_c} \Delta T_c\right)^2} \quad (\text{A.13})$$

The kinematic viscosity is calculated based on Sutherland law for the dynamic viscosity and the ideal gas law for the density. Therefore the following relation is obtained:

$$\frac{1}{\eta} \frac{\partial \eta}{\partial T} = \frac{1}{m} \frac{\partial m}{\partial T} + \frac{1}{T} = \frac{3}{2T} - \frac{1}{T+c} + \frac{1}{T} \quad (\text{A.14})$$

where the Sutherland constant c is equal to 110 K. Since the slot temperature is generally about 300 K, c can be approximate by $T_c/3$. Thus one obtains,

$$\frac{1}{\eta} \frac{\partial \eta}{\partial T} \approx \frac{3}{2T} - \frac{3}{4T} + \frac{1}{T} = \frac{7}{4T} \quad (\text{A.15})$$

Finally the relative uncertainty on the slot Reynolds number can be expressed in terms of relative uncertainties of measured quantities by:

$$\frac{\Delta Re_s}{Re_s} = \sqrt{\left(\frac{\Delta s}{s}\right)^2 + \left(\frac{\Delta U_c}{U_c}\right)^2 + \left(\frac{7}{4} \frac{\Delta T_c}{T_c}\right)^2} \quad (\text{A.16})$$

Film effectiveness, h

The film effectiveness coefficient, h , is the dimensionless temperature that describes the gas temperature with respect to the inflow temperature difference,

$$h = \frac{T - T_{\infty}}{T_c - T_{\infty}} \quad (\text{A.17})$$

It takes values between zero and unity, in the mainstream, and near the coolant injection point, respectively. When expressed at an adiabatic wall this coefficient is often called the adiabatic wall film cooling effectiveness. The relative uncertainty on this coefficient, in its general form, is given by

$$\frac{\Delta h}{h} = \sqrt{\left(\frac{\Delta T}{T - T_{\infty}}\right)^2 + \left(\frac{\Delta T_c}{T_c - T_{\infty}}\right)^2 + \left(\frac{T - T_c}{T - T_{\infty}} \frac{\Delta T_{\infty}}{T_c - T_{\infty}}\right)^2} \quad (\text{A.18})$$

Wall conduction heat flux per unit area

The wall conduction heat flux per unit area is calculated based on the thermal conductivity of the UDEL plate, k_w , the wall thickness, t_w , the wall temperature, T_w , and the backside wall temperature, T_{wb} , using the relation

$$q_k = \frac{k_w}{t_w} (T_w - T_{wb}) \quad (\text{A.19})$$

The relative uncertainty for this quantity is then given by

$$\frac{\Delta q_k}{q_k} = \sqrt{\left(\frac{\Delta k_w}{k_w}\right)^2 + \left(\frac{\Delta t_w}{t_w}\right)^2 + \left(\frac{\Delta T_w}{T_w - T_{wb}}\right)^2 + \left(\frac{\Delta T_{wb}}{T_w - T_{wb}}\right)^2} \quad (\text{A.20})$$

Radiation heat flux per unit area

The net radiation heat flux per unit area on the wall is a function of the wall (subscript w) and casing (subscript 0) respective temperature and emissivity, and the view factor from the wall to the casing. The direct radiation approach gives:

$$q_r = \epsilon_0 \epsilon_w F_{w0} S (T_0^4 - T_w^4) \quad (\text{A.21})$$

The relative uncertainty on the radiative heat flux is given by:

$$\frac{\Delta q_r}{q_r} = \sqrt{\left(\frac{\Delta \epsilon_0}{\epsilon_0}\right)^2 + \left(\frac{\Delta \epsilon_w}{\epsilon_w}\right)^2 + \left(\frac{\Delta F_{w0}}{F_{w0}}\right)^2 + \left(\frac{4T_0^3}{T_0^4 - T_w^4} \Delta T_0\right)^2 + \left(\frac{4T_w^3}{T_0^4 - T_w^4} \Delta T_w\right)^2} \quad (\text{A.22})$$

Convective heat flux per unit area

The convective heat flux per unit area into the wall is equal to conductive heat flux across the wall minus the radiative heat flux from the casing, $q_c = q_k - q_r$. The absolute uncertainty on the convective heat flux is then equal to

$$\Delta q_c = \sqrt{(\Delta q_k)^2 + (\Delta q_r)^2} \quad (\text{A.23})$$

And the relative error is simply obtained by dividing this expression by the conductive heat flux,

$$\frac{\Delta q_c}{q_c} = \sqrt{\left(\frac{\Delta q_k}{q_k}\right)^2 \left(\frac{q_k}{q_k - q_r}\right)^2 + \left(\frac{\Delta q_r}{q_r}\right)^2 \left(\frac{q_r}{q_k - q_r}\right)^2} \quad (\text{A.24})$$

Convective heat transfer coefficient

For film cooling flows, the convective heat transfer coefficient is defined the conductive heat flux and the temperature difference between the adiabatic wall and the non-adiabatic wall cases,

$$h = \frac{q_k}{T_{aw}^* - T_w} \quad (\text{A.25})$$

In this expression the adiabatic wall temperature is replaced by an ideal adiabatic wall temperature, noted T_{aw}^* . Because of slight differences of inflow conditions for adiabatic and non-adiabatic experiments, one needs to correct for these differences in the adiabatic wall temperature. Since the film effectiveness is a dimensionless measure of the mixing it is not sensitive to slight changes in inflow temperature or velocity. Thus one can relate the ideal (or corrected) adiabatic wall temperature at the non-adiabatic flow conditions by using:

$$T_{aw}^* = (T_c^{na} - T_\infty^{na})h_{aw} + T_\infty^{na} \quad (\text{A.26})$$

The absolute uncertainty for this correction is

$$\Delta T_{aw}^* = \sqrt{(h_{aw}\Delta T_c^{na})^2 + ((1-h_{aw})\Delta T_\infty^{na})^2 + ((T_c^{na} - T_\infty^{na})\Delta h_{aw})^2} \quad (\text{A.27})$$

Finally, the relative uncertainty on the convective heat transfer coefficient is given by:

$$\frac{\Delta h}{h} = \sqrt{\left(\frac{\Delta q_c}{q_c}\right)^2 + \left(\frac{\Delta T_{aw}^*}{T_{aw}^* - T_w}\right)^2 + \left(\frac{\Delta T_w}{T_{aw}^* - T_w}\right)^2} \quad (\text{A.28})$$

A3. The Spalart-Allmaras RANS Model

The Spalart-Allmaras model is a one-equation turbulence closure model for Reynolds averaged Navier-Stokes (RANS) simulations. The model solves a transport equation for a modified viscosity, $\tilde{\nu}$, that is written as [47]

$$\frac{\partial \tilde{\nu}}{\partial t} + u_i \frac{\partial \tilde{\nu}}{\partial x_i} = Q(\tilde{\nu}) + \frac{c_{b2}}{c_{b3}} \left(\frac{\partial \tilde{\nu}}{\partial x_i} \right)^2 + \frac{1}{c_{b3}} \frac{\partial}{\partial x_i} \left((\nu + \tilde{\nu}) \frac{\partial \tilde{\nu}}{\partial x_i} \right) \quad (\text{A.29})$$

The source term in the transport equation, $Q(\tilde{\nu})$, is defined by:

$$Q(\tilde{\nu}) = c_{b1}(1 - f_{t2}) \tilde{S} \tilde{\nu} + \left(\frac{c_{b1}}{K^2} f_{t2} - c_{w1} f_w \right) \left(\frac{\tilde{\nu}}{d} \right)^2 \quad (\text{A.30})$$

The eddy-viscosity is related to the modified viscosity by the relation $\nu_t = \tilde{\nu} f_{v1}$, where the model damping functions, auxiliary relations and trip term are:

$$\begin{aligned} f_{v1} &= \frac{C^3}{C^3 - c_{v1}^3}, \quad f_{v2} = 1 - \frac{C}{1 - C f_{v1}}, \quad C = \frac{\tilde{\nu}}{\nu}, \\ f_w &= g \left[\frac{1 + c_{w3}^6}{g^6 + c_{w3}^6} \right]^{1/6}, \quad g = r + c_{w2}(r^6 - r), \quad r = \frac{\tilde{\nu}}{\tilde{S} K^2 d^2} \\ \tilde{S} &= S + \frac{\tilde{\nu}}{K^2 d^2} f_{v2}, \quad S = \sqrt{2 S_{ij} S_{ij}}, \quad f_{t2} = c_{t3} \exp(-c_{t4} C^2) \end{aligned}$$

The turbulence length scale in the model is the variable d , which represents the distance from the nearest wall. K is the von Kármán constant and the strain rate tensor is $S_{ij} = \frac{1}{2}(\partial u_i / \partial x_j + \partial u_j / \partial x_i)$. The model closure coefficients are

$$c_{b1} = 0.1355, \quad c_{b2} = 0.622, \quad c_{b3} = 2/3, \quad c_{v1} = 7.1,$$

$$c_{w1} = \frac{c_{b1}}{K^2} + \frac{1 + c_{b2}}{c_{b3}}, \quad c_{w2} = 0.3, \quad c_{w3} = 2, \quad c_{t3} = 1.2, \quad c_{t4} = 0.5$$

The wall boundary condition for the modified viscosity is $\tilde{\eta}|_{wall} = 0$.

Appendix B. Inflow Conditions for RANS and LES

B1. Means Inlet Profiles

The mean velocity profiles prescribed at the inflow plane of the RANS computational domain are obtained by fitting the PIV data at $x/s \approx 0$. A no-slip boundary condition is applied behind the louver lip, i.e. $1 \leq y/s \leq 1.19$. A piecewise expression is obtained for the slot coolant flow and the mainstream;

$$U(y) = U_{cm} (1 - (2y/s - 1)^6), \quad \text{for } 0 \leq y/s \leq 1 \quad (\text{B.1})$$

$$U(y) = 0, \quad \text{for } 1 \leq y/s \leq 1.19 = (1 + t/s) \quad (\text{B.2})$$

$$U(y) = U_\infty \tanh\left(\frac{y/s - (1 + t/s)}{c_1 t/s}\right) \quad \text{for } y/s > 1.19 \quad (\text{B.3})$$

where the values of the constants U_∞ , U_{cm} and c_1 are reported in Table 8. The reader is reminded that the slot height $s = 4$ mm and that the louver thickness $t = 0.76$ mm.

Similarly, the mean temperature profiles at the inlet plane are obtained by fitting the micro-thermocouple measurements using two piecewise hyperbolic tangent profiles;

$$T(y) = \frac{T_\infty + T_c}{2} + \frac{T_\infty - T_c}{2} \tanh\left(\frac{y/s - (1 + c_2 t/s)}{c_3 t/s}\right) \quad \text{for } 0 \leq y/s \leq y_I/s \quad (\text{B.4})$$

$$T(y) = \frac{T_\infty + T_c}{2} + \frac{T_\infty - T_c}{2} \tanh\left(\frac{y/s - (1 + c_2 t/s)}{c_4 t/s}\right) \quad \text{for } y/s > y_I/s \quad (\text{B.5})$$

where the constants c_2 , c_3 , c_4 and the junction point y_I are prescribed in Table 8, along with the coolant and mainstream temperatures, noted T_c and T_∞ respectively.

Table 8. Variables for the profiles of mean velocity and temperature at the inflow plane

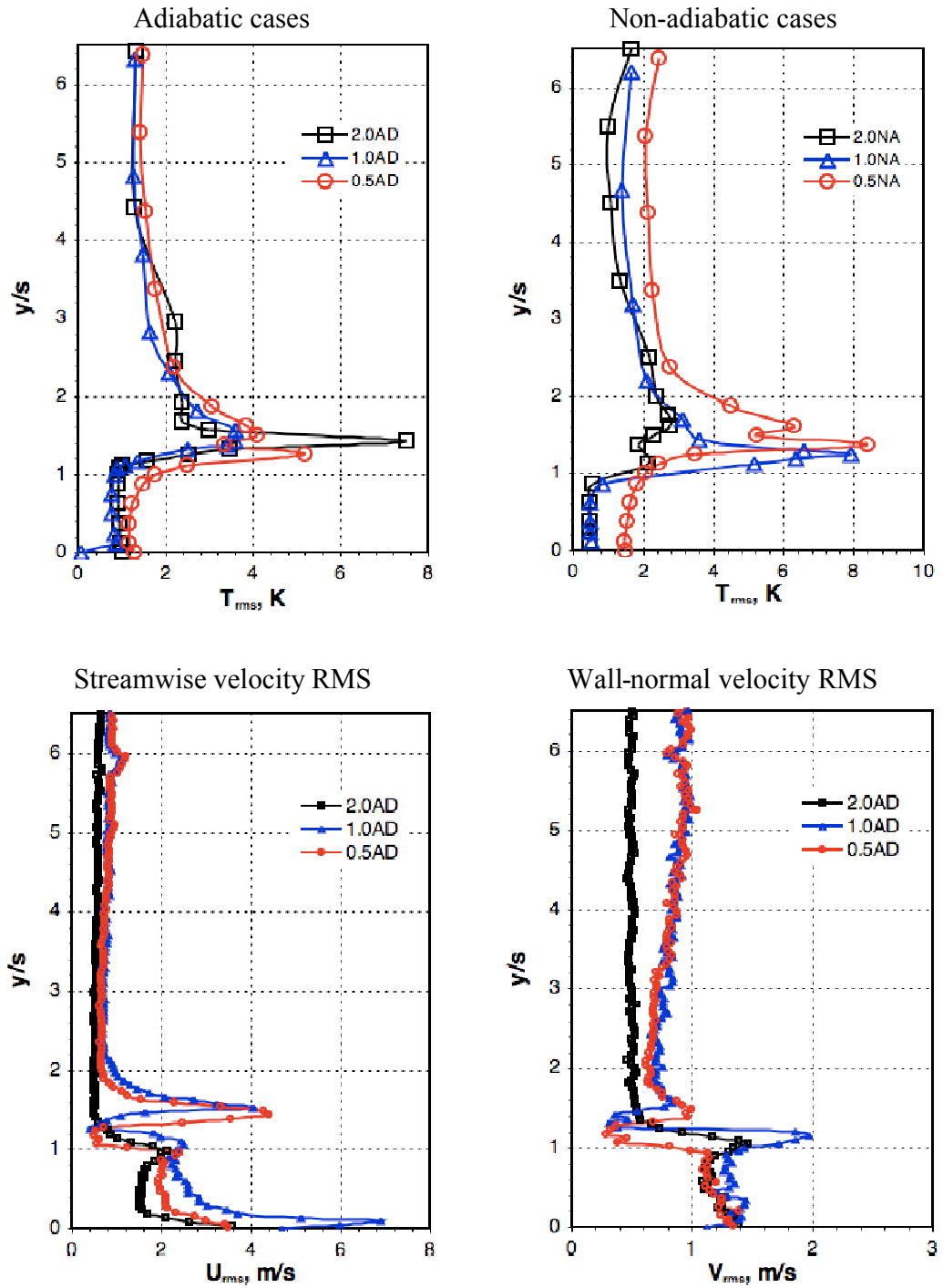
	0.5AD	0.5NA	1.0AD	1.0NA	2.0AD	2.0NA
U_∞ , m/s	24.86		22.1		11.1	
U_{cm} , m/s	12.8		22.6		24.7	
c_1	1.5		1.5		1.5	
T_∞ , K	462.02	454.94	454.33	446.33	462.92	437.89
T_c , K	304.78	306.11	298.88	304.43	296.33	301.54
y_1/s	1.4	1.4	1.4	1.2	1.36	1.37
c_2	2.2	2.4	2.2	1.85	2.0	2.0
c_3	0.75	0.75	0.75	0.75	0.75	0.75
c_4	3.0	3.0	3.0	2.25	3.0	2.7

B2. Inlet Profiles of RMS Temperature and Velocity

The profiles of temperature and velocity RMS at the inflow plane are presented in Figure 48. The temperature RMS is measured with the micro-thermocouple probe with digital compensation for its thermal inertia. The profiles of T_{rms} show very similar behaviors for the adiabatic and the non-adiabatic cases with large RMS values in the wake of the louver and small nearly uniform values in the mainstream and the coolant flows. Furthermore, the profiles of T_{rms} display little dependence with the blowing ratio.

The RMS of the streamwise and wall-normal velocity components is measured with the PIV data at the inflow plane using 1000 samples for the statistics. The velocity RMS depends on the operating conditions, and consequently on the velocity ratio. The case VR1.0 displays the most RMS for U and V in the mainstream and near the wall. In the mainstream the turbulence is nearly isotropic since U_{rms} and V_{rms} take comparable values.

Figure 48. Measurements of inlet temperature RMS and velocity RMS profiles



B3. Inlet Profiles of Modified Eddy Viscosity

For each RANS simulation of the film cooling flow, inlet profiles of modified eddy viscosity, $\tilde{\eta}_t$, are prescribed as a boundary condition for the Spalart-Allmaras transport equation at the inflow plane. This inlet profile is obtained by performing a precursor simulation in the slot and in the mainstream. The corresponding profiles normalized by the kinematic viscosity, η , are presented in Figure 49. At the exit of the slot, the eddy viscosity is higher for the wall jet case, because of the presence of a highly turbulent, high-speed flow in the region. Because of a low mainstream velocity for this case, the eddy viscosity is also smaller compared to the other cases. Note also that the boundary layer case (VR1.0) has the highest turbulence in the freestream and the largest boundary layer thickness. Finally one can notice significantly smaller slot turbulence for the wall wake case (VR0.5).

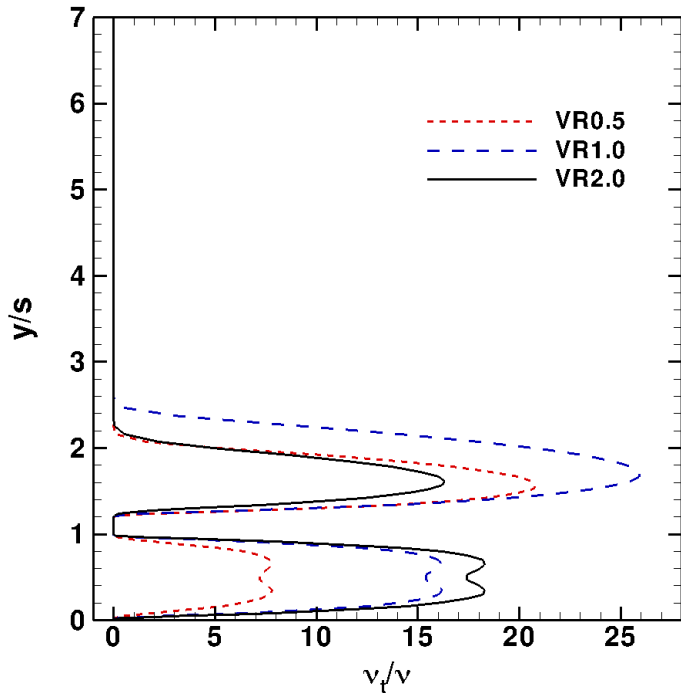


Figure 49. Inlet profiles of modified eddy-viscosity for the RANS simulations

Bibliography

- [1] A. H. Lefebvre, *Gas Turbine Combustion*, Taylor & Francis, 1983, pp. 257-320.
- [2] Sutton, G. P., and Biblarz, O., *Rocket Propulsion Elements*, 7th Edition, John Wiley and Sons, 2001.
- [3] K. Wieghardt, "Hot Air Discharge for De-Icing", *Air Material Command*, AAF Trans. No. F-TS-919-RE, Dec. 1946.
- [4] J. P. Hartnett, R. C. Birkebak, and E. R. G. Eckert, "Velocity distributions, Temperature Distributions, Effectiveness and Heat Transfer for Air Injected Through a Tangential Slot Into a Turbulent Boundary layer", *Journal of Heat Transfer*, August 1961, Vol. 83, pp. 293-306.
- [5] M. Tribus and J. Klein "Forced Convection From Non-Isothermal Surfaces", *Heat Transfer, a Symposium*, University of Michigan Press, Ann Arbor, MI, 1953, pp. 211-235.
- [6] J. L. Stollery, and A. A. M. El-Ehwany, "A Note on the Use of Boundary-Layer Model for Correlating Film Cooling Data", *International Journal of Heat and Mass Transfer*, 1965, Vol. 8, No. 1, pp. 55-65.
- [7] C. J. Marek and R. R. Tacina, "Effect of Free-Stream Turbulence on Film Cooling", NASA TN D-7958, 1975.
- [8] F. F. Simon, "Jet Model for Slot Film Cooling With Effect of Free-Stream and Coolant Turbulence", NASA TP 2655, October 1986.
- [9] D. R. Ballal and A. H. Lefebvre, "Film Cooling Effectiveness in the Near Slot Region", *Journal of Heat Transfer*, May 1973, Vol. 93, pp. 165-166.
- [10] W. K. Burns and J. L. Stollery, "The Influence Foreign Gas Injection and Slot Geometry on Film Cooling Effectiveness", *International Journal of Heat and Mass Transfer*, 1969, Vol. 12, No. 9, pp. 935-951.
- [11] R. J. Goldstein, "Film Cooling", in *Advances in Heat Transfer*, Vol. 7, Academic Press, New York, 1971, pp. 321-378.
- [12] Cruz, C. A. and Marshall, A. W., "Surface and Gas Phase Temperature Measurements Along a Film Cooled Wall", *Journal of Thermophysics and Heat Transfer*, Vol. 21, No. 1, January–March 2007, pp. 181-189.
- [13] Wilcox, D. C., "Turbulence Modeling: An Overview", *39th Aerospace Sciences Meeting and Exhibit*, Reno, NV, January 8-11, 2001, paper AIAA 2001-0724.
- [14] Pajayakrit, P., and Kind, R. J., "Assessment and Modification of Two-Equation Turbulence Models", *AIAA Journal*, Vol. 38, No. 6, June 2000, pp. 955-963.

- [15] Zhou, J. M., Salcudean, M. and Gartshore, I. S., “A Numerical Computation of Film Cooling Effectiveness”, *Near-Wall Turbulent Flows*, Elsevier Science Publishers, 1993, pp. 377-386.
- [16] Jansson, L. S., Davidson, L., and Olsson, E., “Calculation of Steady and Unsteady Flows in a Film-Cooling Arrangement Using a Two-Layer Algebraic Stress Model”, *Numerical Heat Transfer, Part A*, Vol. 25, 1994, pp. 237-258.
- [17] Jia, R., Sundén, B., Miron, P., Léger, B., “A Numerical and Experimental Investigation of Slot Film-Cooling Jet with Various Angles”, *Journal of Turbomachinery*, Vol. 127, July 2005, pp. 635-645.
- [18] Spalart, P. R., Jou, W. -H., Trelets, M., and Allmaras, S., R., “Comments on the Feasibility of LES for Wings, and on a Hybrid RANS/LES Approach”, 1st AFOSR Int. Conf. on DNS/LES, 4-8 August, 1997, Ruston, LA, *Advances in DNS/LES*, C. Liu and Z. Liu eds., Greyden Press, Columbus, OH.
- [19] Roy, S., Kapadia, S. and Heidmann J. D., “Film Cooling Analysis Using DES Turbulence Model”, *ASME Turbo Expo*, paper GT 2003-38140, June 2003.
- [20] Kapadia, S., Roy, S., and Heidmann J. D., “First Hybrid Turbulence Modeling for Turbine Blade Cooling”, *Journal of Thermophysics and Heat Transfer*, Vol. 18, No. 4, 2004, pp. 154-156
- [21] Muldoon, F. and Acharya, S., “Analysis of k-e Budgets for Film Cooling Using Direct Numerical Simulation”, *AIAA Journal*, Vol. 44, No. 12, December 2006, pp. 3010-21.
- [22] Martini, P., Schulz, A., Bauer, H. -J, and Whitney, C. F., “Detached Eddy Simulation of Film Cooling Performance on the Trailing Edge Cutback of Gas Turbine Airfoils”, *Journal of Turbomachinery*, Vol. 128, April 2006, pp. 292-299.
- [23] Dejoan, A., and Leschziner, M. A., “Large Eddy Simulation of a Plane Turbulent Wall Jet”, *Physics of Fluids*, 17, 025102-16, 2005.
- [24] Ahlman, D., Brethouwer, G. and Johansson, A. V., “Direct numerical simulation of a plane turbulent jet including scalar mixing”, *Physics of Fluids*, Vol. 19, Issue 6, 065102, 2007.
- [25] Keating, A., “Large-eddy simulation of heat transfer in the turbulent channel flow and in the turbulent flow downstream of a backward-facing step”, PhD Thesis, Department of Mechanical Engineering, The University of Queensland, Brisbane, Australia, 2004.
- [26] Keating, A., Piomelli, U., Bremhorst, K., and Nesic, S., “Large-eddy simulation of heat transfer downstream of a backward-facing step”, *Journal of Turbulence*, 5. 020, 2004.

- [27] Mehta, R. D. and Bradshaw, P., "Design Rules for Small Low Speed Wind Tunnels", *The Aeronautical Journal*, Nov. 1979, 73: pp. 443-449.
- [28] Adrian, R. J., "Scattering particle characteristics and their effects on pulsed laser measurements of fluid flows: speckle velocimetry vs. particle image velocimetry", *Applied Optics*, 1984. 23, pp. 1690-1691.
- [29] Pickering, C. J. D., and Halliwell, N., "LSP and PIV: photographic film noise", *Applied Optics*, 1984. 23, pp. 2961-2969.
- [30] Durst, F., Melling, A., and Whitelaw, J. H., *Principles and Practice of Laser-Doppler Anemometry*, Academic Press, 2nd Edition, 1981, pp. 270-279.
- [31] Samimy, M., and Lele, S. K., "Motion of particles with inertia in a compressible free-shear layer", *Physics of Fluids A*, Vol. 3, August 1991, pp. 1915-1923.
- [32] Bernard, P. S., and Wallace, J. M., *Turbulent Flow: Analysis Measurement and Prediction*, John Wiley & Sons, Hoboken, New Jersey, 2002.
- [33] Schlichting, H., and Gersten, K., *Boundary Layer Theory*, Springer, 8th Revised and Enlarged Edition, 2003.
- [34] Melling, A., "Tracer particles and seeding for particle image velocimetry", *Measurement Science and Technology*, Vol. 8, 1997. pp. 1406-1416.
- [35] FlowMaster Software Product Manual for Davis 7.2, LaVision GmbH, printed in Göttingen, Germany, December 7 2006.
- [36] Westerweel, J., "Theoretical analysis of the measurement precision in particle image velocimetry", *Experiments in Fluids*, 2000, Vol. 29. Issue S1, pp. 3-12.
- [37] Adrian, R. J., "Particle-imaging techniques for experimental fluid mechanics", *Annual Review of Fluid Mechanics*, 1991. 23, pp. 261-304.
- [38] Nogueira, J., Lecuona, A. and Rodríguez, P. A., "Data validation, false vectors correction and derived magnitudes calculation on PIV data", *Measurement Science and Technology*, 1997, Vol. 8, No. 12, pp. 1493-1501.
- [39] Modest, M. F., *Radiative Heat Transfer*, McGraw-Hill, New York, 1993, pp. 200-217.
- [40] Siegel, R. and Howell, J. R., *Thermal Radiation Heat Transfer*, Hemisphere Publishing Corporation, 2nd Edition, 1972, p. 823.
- [41] Shaddix, C. R. "Practical Aspects of Correcting Thermocouple Measurements for Radiation Loss", *Western State Section/The Combustion Institute*, WSS/CI 98F-14, 1998.

- [42] Marshall, A. W., "Effects of Jet Momentum Distribution on Combustion Characteristics in Co-Swirling Flames", Ph.D. thesis, University of Maryland, 1996.
- [43] Taylor, J. R., Introduction to Error Analysis: The Study of Uncertainty in Physical Measurements, Edition 1982, Mill Valley, Oxford University Press.
- [44] Smagorinsky, J., "General circulation experiment with the primitive equations. I. The basic experiment", *Monthly Weather Review*, Vol. 91, N. 3, pp. 94-164, 1963.
- [45] Volker, J., Large Eddy Simulation of Turbulent Incompressible Flows, Analytical and Numerical Results for a Class of LES Models, Lecture Notes in Computational Science and Engineering, Springer, 2004, Chap. 4, pp. 47-62.
- [46] Sagaut, P., Large Eddy Simulation for Incompressible Flows: An Introduction, 2nd edition, Springer-Verlag, 2002, pp. 59-68.
- [47] Spalart, P. R. and Allmaras, S. R., "A One-Equation Turbulence Model for Aerodynamic Flows", *La Recherche Aerospaciale*, No. 1, pp. 5-21, 1994.
- [48] Cabot, W. and Moin, P., Large Eddy Simulations of Scalar Transport with the Dynamic Subgrid-Scalar Model, in Large Eddy Simulations of Complex Engineering and Geophysical Flows, Cambridge University Press, 1993, Chap. 7, pp. 141-158.
- [49] Kays and Crawford, *Convective Heat and Mass Transfer*, 3rd Edition, 1993, McGraw-Hill.
- [50] Germano, M., Piomelli, U., Moin, P., and Cabot, W. H., "A dynamic subgrid-scale eddy-viscosity model", *Physics of Fluids*, A 3, 1760-1765, 1991.
- [51] Piomelli, U., *Applications of Large Eddy Simulations in Engineering: An Overview*, in Large Eddy Simulations of Complex Engineering and Geophysical Flows, Cambridge University Press, 1993, Chap. 6, pp. 119-137.
- [52] Lilly, D. K., "A proposed modification of the Germano subgrid-scale closure method", *Physics of Fluids*, A 4, pp. 635-635, 1992.
- [53] Meneveau, C., Lund, T. S., and Cabot, W. H., "A Lagrangian dynamic subgrid-scale model of turbulence", *Journal of Fluid Mechanics*, Vol. 319, pp. 353-385, 1996.
- [54] Morinishi, Y., Lund, T. S., Vasilyev, O. V., & Moin, P. "Fully conservative higher order finite difference schemes for incompressible flows", *Journal of Computational Physics*, 1998, No. 143, pp. 90-124.

- [55] F.E. Ham, F.S. Lien, and A.B. Strong, “A fully conservative second-order finite difference scheme for incompressible flow on non-uniform grids”, *Journal of Computational Physics*, 2002, No. 177, pp. 117-133.
- [56] B.P. Leonard, “A stable and accurate convection modeling procedure based on quadratic upstream interpolation”, *Comput. Meth. Appl. Mech. Engrg.*, 1979, Vol. 19, pp. 59-98.
- [57] Spalart, P.R., Moser, R.D., and Rogers, M.M., “Spectral methods for the Navier-Stokes equations with one infinite and two periodic directions”, *Journal of Computational Physics*, 1991, Vol. 96, pp. 297-324.
- [58] Chapman, D. R., “Computational aerodynamics development and outlook”, *AIAA Journal*, 1979, Vol. 17, pp. 1293- 1313.
- [59] Piomelli, U. and Balaras, E., “Wall-Layer Models for Large-Eddy Simulations”, *Annual Review of Fluid Mechanics*, 2002, Vol. 34, pp. 349–374.
- [60] Keating, A., Piomelli, U., Balaras, E., and Kaltenbach, H. J., “A priori and a posteriori tests of the inflow conditions for large-eddy simulations”, *Physics of Fluids*, Vol. 16, N. 22, pp. 4696-4712, 2004.
- [61] Spalart, P. R. and Wattmuff, J. H., “Experimental and numerical study of a turbulent boundary layer with pressure gradients”, *Journal of Fluid Mechanics*, Vol. 249, pp. 337-371, 1993.
- [62] Lund, T. S., Wu, X., and Squires, K. D., “Generation of inflow data for the spatially-developing boundary layer simulations”, *Journal of Computational Physics*, Vol. 140, Issue 2, pp. 233-258, 1998.
- [63] Kasagi, N., Tomita, Y., and Kuroda, A., “Direct Numerical Simulation of Passive Scalar Field in a Turbulent Flow”, *Journal of Heat Transfer*, Vol. 144, August 1992, pp. 598-606.
- [64] Kim, J., Moin, P., and Moser, R., “Turbulence statistics in fully developed turbulent channel flow at low Reynolds number”, *Journal of Fluid Mechanics*, Vol. 177, pp. 136-166, 1987.
- [65] Kader, B. A., “Temperature and concentration profiles in fully turbulent boundary layers”, *International Journal of Heat and Mass Transfer*, Vol. 111, pp. 385-392, 1981.
- [66] Abramovich, G. N., *The Theory of Turbulent Jets*, MIT Press, 1963, Chapter 11.
- [67] Mayhew, J. E., Baughn, J. W., and Byerley, A. R., “The effect of freestream turbulence on film cooling adiabatic effectiveness”, *Int. J. of Heat and Fluid Flow*, 24, 2003, pp. 669-679.

- [68] Saumweber, C., Schulz, A., and Wittig, S., “Free-stream turbulence effects on film cooling with shaped holes”, *J. of Turbomachinery*, Vol. 125, January 2003, pp. 65-73.
- [69] Juhasz, A. J. and Marek, C. J. *Combustor liner film cooling in the presence of high free-stream turbulence*, NASA Technical Note, TN D-6360, July 1973.
- [70] Kruka, V. and Eskinazi, S., “The wall-jet in a moving stream”, *Journal of Fluid Mechanics*, Vol. 20, Part 4, 1964, pp. 555-579.
- [71] Lauder, B. E. and Rodi W., “The Turbulent Wall Jet – Measurement and Modeling”, *Annual Review of Fluid Mechanics*, Vol. 15, 1983, pp. 429-459
- [72] Mathieu, J. and Tailland, A., “Etude d’un jet plan dirigé tangentielle à une paroi”, *C. R. Acad. Sci.*, Vol. 252, 1961, 3736.
- [73] Osterlund, J. M., “Experimental studies of zero-pressure gradient turbulent boundary layer flows”, PhD thesis, Royal Institute of Technology, Stockholm, 1999.
- [74] Eriksson, J. G., Karlsson, R. I., and Persson, J., “AN experimental study of a two-dimensional plane turbulent jet”, *Experiments in Fluids*, Vol. 25, No. 50, 1998.